Master thesis and internship[BR]- Master's thesis : Development of a performance modeling tool for nulling interferometry[BR]- Internship

Auteur : Viseur, Lucas
Promoteur(s) : Clermont, Lionel
Faculté : Faculté des Sciences appliquées
Diplôme : Master en ingénieur civil en aérospatiale, à finalité spécialisée en "aerospace engineering"
Année académique : 2023-2024
URI/URL : http://hdl.handle.net/2268.2/20392

Development of a performance modeling tool for nulling interferometry

Master's thesis completed in order to obtain the degree of Master of Science in Aerospace Engineering - Université de Liège - Faculté des Sciences Appliquées

VISEUR Lucas

Supervisor:
Dr. CLERMONT Lionel

Co-supervisor:
DANDUMONT Colin

Research Centre:
Centre Spatial de Liège - CSL

Academic year 2023-2024

Abstract

This master's thesis delves into the field of space nulling interferometry, a promising technique for direct exoplanet detection and characterization. The work begins with an introduction to nulling interferometry, followed by a comprehensive theoretical background that lays the foundation for understanding the principles and limitations of this method. A review of previous space mission concepts, such as the Darwin mission, as well as currently existing ground-based facilities, highlight the advancements and lessons learned in the field throughout the years.

This thesis aims in enhancing the understanding and application of nulling interferometry by the development in chapter 4 of an advanced analysis tool to assess interference quality. Coupling the results of the ray-tracing software CodeV and postprocess capabilities of MATLAB, this tool performs detailed tolerancing and sensitivity analysis, essential for optimizing the design and performance of future interferometric instruments. The tool was validated through a series of MonteCarlo simulations in chapter 5 and sensitivity analysis in chapter 6, demonstrating its effectiveness in identifying and mitigating potential sources of error.

The results underscore the importance of precise optical design, calibration, and correction mechanisms in achieving high-quality interference. This thesis provides a robust framework for future research and development in nulling interferometry such as precise tolerancing and optimisation of a nulling interferometer optical design, contributing to the ongoing quest for discovering and studying exoplanets.

Acknowledgements

To begin with, I would like to thank my supervisor, Dr. Lionel Clermont, for his invaluable guidance, advice, wisdom, and deep understanding in the optical field. This master's thesis would not have been the same without his contributions and his ability to push me further and further. Meeting him has been a turning point in my academic career, profoundly shaping my future path for the better.

I am also grateful for the comments and advice of my co-supervisor, Colin Dandumont, whose incredible knowledge of nulling interferometry has been of great help. His dedication and good humor accompanied me throughout the completion of this work.

I extend my gratitude to the staff of the Centre Spatial de Liège, with whom I interacted during the five months of my internship.

I would like to thank my friends for their psychological support, especially R., J., S., and my CSL teammates E., N., and L. Special thanks to L. for our chess game breaks and mutual support to exercise.

Last but not least, I would like to thank the dearest people in my life, without whom I would not be here. My best friend V., for his enduring friendship and for putting up with me for so long. My sister Z., the one who understands me the most and for whom I would do anything. My father, who will always be a role model for me and the most knowledgeable person in my eyes. My mother, who has always believed in me and supported me against all odds. "One round at a time," she often repeated to me. Here we are, Mom; this is my master's final round.

Contents

Abstract i

Acknowledgements ii

Introduction 1

1 Theory of nulling interferometry 4

1.1 Light wave properties 4

1.2 Fringe contrast 6

1.3 Going to space 8

1.4 IR domain 9

1.5 Bracewell first concept 11

1.6 Kernel improved interferometer . 13

1.7 Phase chopping 15

1.8 Practical design of an interferometer 16

1.8.1 Beam collection and transport 16

1.8.2 Beam correction 17

1.8.3 Fringe and angle trackers . 19

1.8.4 Beam combination and detection 20

1.9 Response function 22

1.10 Conclusions 25

2 Instrumentations for nulling interferometry 26

2.1 Ground-based instruments 26

2.1.1 LBTI 26

2.1.2 VLTI 28

2.2 Space-based ideas and concepts . 29

2.2.1 Brief history 29

2.2.2 Darwin/TPF-I project . . 29

2.2.3 Darwin/TPF-I demonstrators 30

2.3 Space-based rebirth: LIFE mission 35

2.4 Conclusions 36

3 Optical design of a nulling interferometer 37

3.1 Architecture 38

3.2 Dimensioning 40

3.3 CodeV designs 44

3.3.1 Siderostat-Confocal Hybrid Optic (SCoHo) 44

3.3.2 Direct Confocal Setup (DiCoS) 46

3.4 Conclusions 48

4 Performance modeling tool 49

4.1 The need for tolerancing 49

4.2 Extraction of output parameters from CodeV 51

4.2.1 Optical Path Distribution 52

4.2.2 Relative Phase Distribution 53

4.2.3 Interference Intensity . . . 54

4.3 Derivation of the response function 56

4.3.1 Choice of the figure of merit 56

4.3.2 On-axis analytical development 57

4.3.3 Off-axis analytical development 59

4.4 Tolerance analysis interpretations 65

4.5 Conclusions 68

5 Tolerance modeling results **69**
5.1 Tolerancing hypothesis 69
5.2 Nominal performance 70
5.3 Results 71
5.3.1 Case study 1 71
5.3.2 Case study 2 75
5.3.3 Case study 3 77
5.4 Conclusions 78

6 Parameters sensitivity analysis **79**
6.1 Tip/tilt angles 79
6.1.1 Applied case 79
6.1.2 Sensitivity analysis 81
6.1.3 Tip/tilt correlation 82
6.2 Mirror curve imperfections 87
6.2.1 Applied case 87
6.2.2 Sensitivity analysis 88
6.3 Conclusions 90

Conclusions and perspectives **91**

Appendices **92**

Bibliography **96**

Introduction

Exploration is in our nature. We began as wanderers, and we are wanderers still. We have lingered long enough on the shores of the cosmic ocean. We are ready at last to set sail for the stars.

Carl Sagan.

Throughout history, mankind has always pondered whether we were alone in the universe. In this aspect, the search for planets orbiting other stars than our sun, known as exoplanets, has emerged as an increasingly interesting topic for the science domain. Since the breakthrough of the first exoplanet discovery by Wolszczan and Frail in 1992 [1] and the subsequent first exoplanet detection around a main sequence star, 51 Peg, by Mayor and Queloz (1995) [2], significant advances in this field have occurred.

Two primary methods of exoplanet detection have emerged: indirect and direct techniques [3]. The former encompasses radial velocity, transit photometry, gravitational microlensing and astrometry.

Radial velocity takes advantage of the Doppler effect, observing the star's wobbles induced by the orbiting object. This pioneered method of detection is still employed notably with the Keck telescope and many others. However, it provides imprecise estimates of a planet's mass, due to the uncertainty in the inclination of the orbit [4].

Transit photometry, on the other hand, aims to search for shadows: the star's luminosity decreases when the planet crosses the line of sight of the observer. This method, utilized extensively by telescopes such as TRAPPIST [5], allows for the determination of a planet's radius, as well as the assessment of its atmospheric composition. Yet, it requires an alignment of the line of sight of the observer and the planet's orbital plane. The frequency of transit may be scarce, limited by the exoplanet's orbital period. For an Earth-like planet, this probability would be approximately 0.5% [6].

Gravitational microlensing, applicable to further stars even beyond the galaxy, capitalizes on the gravitational lensing effect predicted by general relativity. Few exoplanets have nevertheless been detected using this method due to its low occurence probability and stringent geometric requirements as well as the singularity and non-repeatability nature of those events.

Lastly, astrometry seeks minuscule celestial movements: it observes the star's apparent position in the sky relative to other stars to infer exoplanets presence. However, detecting such movements poses significant challenges.

Figure 0.1 summarizes the indirect methods of detection.

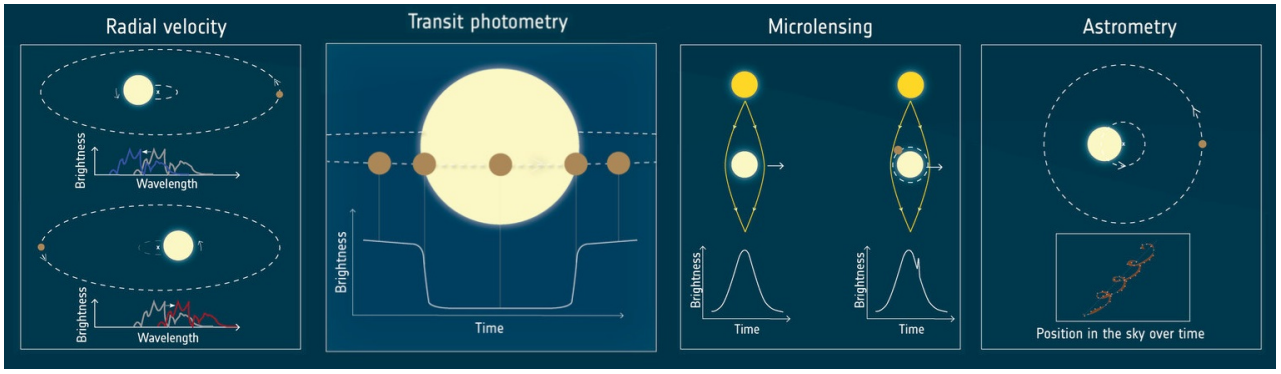

Figure 0.1: Illustrations of indirect methods for exoplanet detection [7].

On the other hand, direct techniques are carried by coronography and interferometry. Direct imaging detects planets in close proximity to their host star, requiring sufficient photon flux variation, yet enabling spectroscopic or photometric characterisation of the atmosphere.

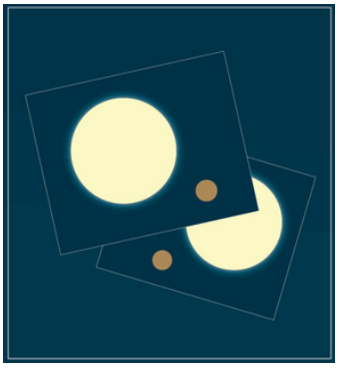

Figure 0.2: Direct imaging method illustration [7].

Coronography involves physically occulting the parent star to observe its surroundings and detect planets. However, light from the star's corona may still interfere, subsequently reducing the contrast.

Conversely, nulling interferometry takes advantage of the wave property of light to suppress the star's luminosity through destructive interferences to observe the exoplanets. This method is described by a high angular resolution.

Figure 0.3 illustrates the efficacy of each method relative to the number of exoplanets detected.

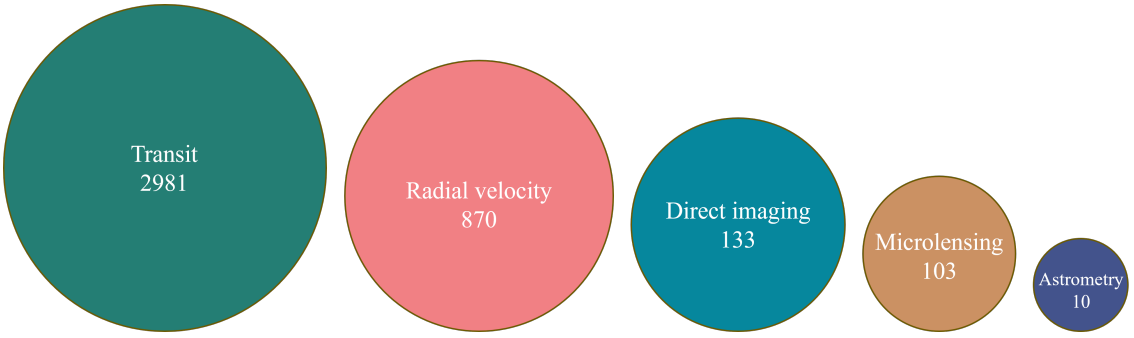

Figure 0.3: Classification of exoplanet detection methods and associated detected number. 4143 exoplanets detected (47 from other methods) at the date of the 6th December 2019 [7].

The focus of this master thesis is on direct imaging using nulling interferometry, aiming to design a nulling interferometer for an exoplanet detection space mission.

The methodology outlined in this master thesis begins with a comprehensive introduction to nulling interferometry, followed by a thorough review of previous and future space missions and the current state-of-the-art in this field. Thereafter, two enhanced optical design, building upon previous missions, are proposed with an emphasis on the optical layout preceding the beam combiner. The main goal of this master's thesis is then to build and propose a complete modeling analyzing tool to assess nulling interferometer performance. Subsequent chapters discuss the results derived from the previously defined tool in MonteCarlo tolerancing and fixed parameters sensitivity analysis on the optical systems previously designed. Finally, the significant findings of this work are summarized and conclusions are drawn. The development of this tool calls for continuation in a future work in order to apply it to a concrete case and deduce a precise and meticulous analysis of an optical design in order to further demonstrate its full potential.

The European Space Agency (ESA) is keen to study the feasibility of projects in the field of nulling interferometry. One notable initiative involves the development of an L-space nulling interferometry mission for Voyage 2050, ESA's scientific space program for the period 2035-2050, in collaboration with TU Delft, KU Leuven, AMOS, and the Centre Spatial de Liège (CSL). This master's thesis aligns with the same perspective, though it remains an independent endeavor.

Chapter 1

Theory of nulling interferometry

Contents

1.1 Light wave properties . . . 4
1.2 Fringe contrast . . . 6
1.3 Going to space . . . 8
1.4 IR domain . . . 9
1.5 Bracewell first concept . . . 11
1.6 Kernel improved interferometer . . . 13
1.7 Phase chopping . . . 15
1.8 Practical design of an interferometer . . . 16
1.8.1 Beam collection and transport . . . 16
1.8.2 Beam correction . . . 17
1.8.3 Fringe and angle trackers . . . 19
1.8.4 Beam combination and detection . . . 20
1.9 Response function . . . 22
1.10 Conclusions . . . 25

In this first chapter, the **concept of interferometry** is explored from the **theoretical background** to foundational concepts. The various components end use and alternatives are also explained thoroughly. Finally, instrumental constraints of nulling interferometry are investigated.

1.1 Light wave properties

Starting from the duality of light, it exhibits wave-like behavior under certain conditions. The diffraction phenomenon exemplifies this wave property. This relates to the bending or interferences of waves passing through an aperture or in the immediate vicinity of an obstacle, into the geometric shadow region. The aperture or obstacle then acts as a secondary source for the propagating wave.

Hence, the angular resolution of telescopes and consequently their spatial resolution is inherently limited by diffraction due to their finite aperture size. Conversely to the idealized point image in geometric optics, or stigmatism, the image of a point source at infinity produced by a telescope

results in an Airy pattern on the image plane. This is a consequence of the diffraction limit for a circular aperture [8]:

$$\theta = 1.22 \cdot \frac{\lambda}{D} \ , \tag{1.1}$$

with θ the angular resolution, 1.22 the coefficient corresponding to the first zero of the order-one Bessel function of the first kind J_1 divided by π, λ the wavelength and D the aperture diameter.

Rayleigh's criterion then states that an optical design is diffraction-limited when the first maximum of the diffraction pattern from one source coincides with the first minimum of the diffraction pattern from another source. Figure 1.1 describes the aforementioned limit and criterion.

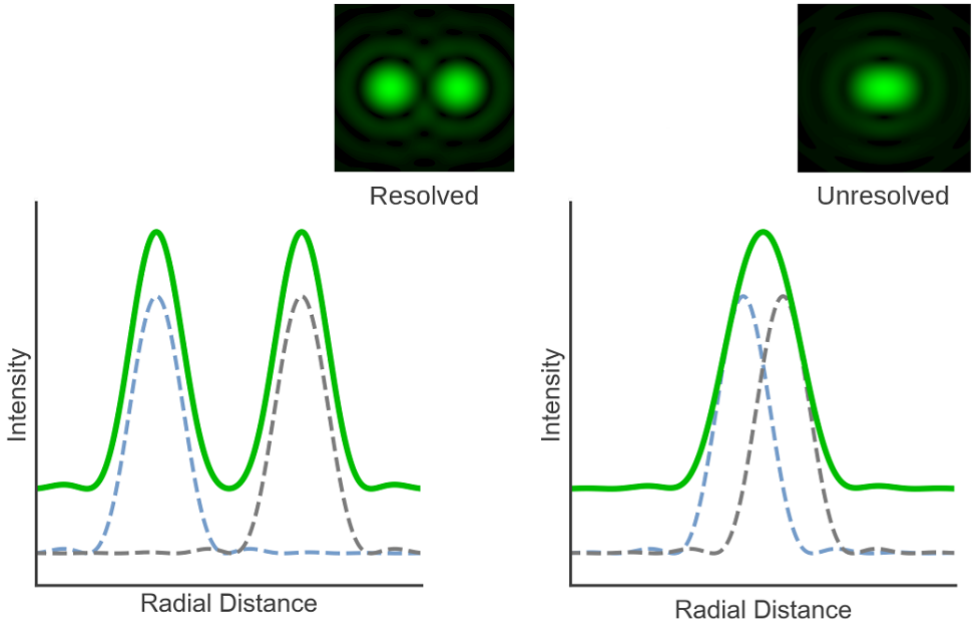

Figure 1.1: Representation of the Airy functions of two separated sources and the associated Rayleigh's criterion.

Given that the optical design is limited by the diameter, the relentless need to increase telescope size over the past decades is justifiable. From the Very Large Telescope (VLT) to the upcoming Extremely Large Telescope (ELT), mirror sizes are poised to increase nearly fivefold, from 8 to 39 meters. While adaptive optics have enabled the utilization of these larger mirrors, there are practical limitations to the size expansion of telescopes due to technical challenges. The production of large glass components becomes progressively tedious, as does the support of these expansive mirrors. Gravity affects significantly the mirrors, inducing deformations under their own weight, resulting in optical aberrations and a degradation in image quality. Managing thermal properties poses another challenge, with gravity-induced temperature gradients leading to thermal deformations that impact the mirror's optical integrity [9].

However, by using an interferometer consisting of two telescopes, this limitation can be overcome through the principle of aperture synthesis. The two telescopes act as an equivalent single one whose diameter is equal to the baseline b separating them [8].

This concept and the resulting interference pattern are illustrated in Figure 1.2.

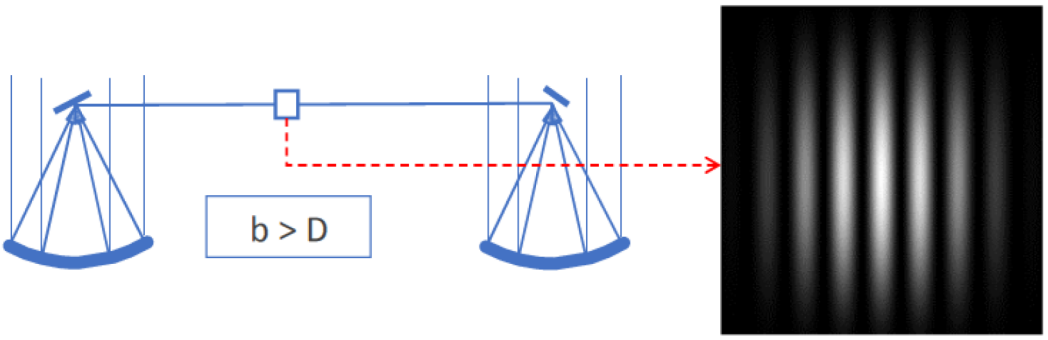

Figure 1.2: Interferometer concept using two circular aperture telescopes and associated fringe diffraction pattern [8].

The Airy pattern is seen to be modulated by the periodic bright/dark fringes spaced by $\frac{\lambda}{b}$.

The minimum achievable angular resolution by this design is given by

$$\theta = \frac{\lambda}{2b} \tag{1.2}$$

which has to be compared with Equation 1.1. This design is thus equivalent in terms of angular resolution to a single telescope of diameter equal to the baseline b of the two-element interferometer, thereby improving it, but gathering the exact same flux than the two telescopes taken separately.

1.2 Fringe contrast

Referring to Equation 1.2, the contrast of the fringe pattern depends on the angular size of the object and the baseline between the two telescopes. Thus, a larger baseline results in closer fringes and reduced ability to resolve fine details. This relationship is illustrated in Figure 1.3.

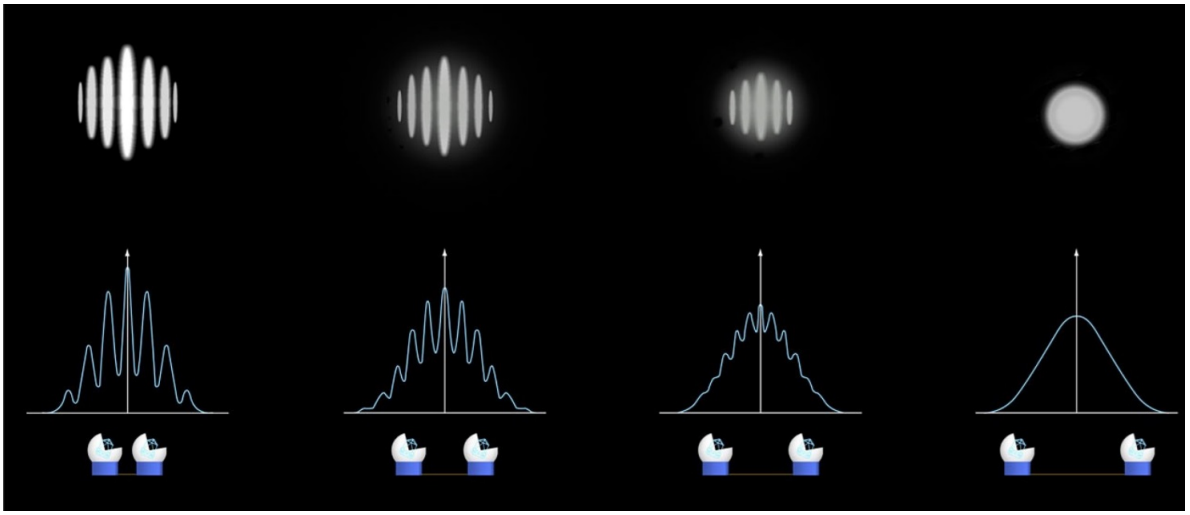

Figure 1.3: Coherence evolution and fringe contrast with respect to the baseline of a two-element interferometer [8].

The fringe contrast, or visibility V, is the primary observable of an interferometer and is defined as [10]:

$$V = \frac{I_{\max} - I_{\min}}{I_{\max} + I_{\min}} \ , \tag{1.3}$$

where $I_{\max}$ and $I_{\min}$ denote the maximum and minimum fringe intensity, respectively.

As can be derived from the Rayleigh's criterion in this context, coherence is lost when $\theta = \frac{\lambda}{2b}$ and the contrast steadily decreases before reaching this limit. If this equation holds true, the angular size of the observed object is directly related to the Airy disk diameter.

Due to potential noise effects, it is often preferable to work with the visibility squared, given for a uniform disk of angular diameter θ_{UD} by:

$$V^2 = \left(\frac{2J_1(\pi\theta_{UD} b_\perp/\lambda)}{\pi\theta_{UD} b_\perp/\lambda} \right) \ , \tag{1.4}$$

with J_1 the first Bessel function and $b_\perp$ the projected baseline onto the sky plane.

The Van Cittert-Zernike theorem establishes a fundamental connection between fringe contrast, or complex visibility, and the intensity distribution of the light source [10][11]. Mathematically, this relationship is expressed through the Fourier transform pairs hereafter:

$$\begin{aligned} V(u,v) &= \iint I(l,m) \mathrm{e}^{2\pi i(ul+vm)} \mathrm{d}l \mathrm{d}m \\ I(l,m) &= \iint V(u,v) \mathrm{e}^{-2\pi i(ul+vm)} \mathrm{d}u \mathrm{d}v \end{aligned} \tag{1.5}$$

where the variables u,v represent the spatial frequencies in the east-west and north-south directions, respectively, while l,m denote direction cosines relative to a reference position [8].

In essence, this theorem enables to infer the spatial coherence of a light source from the visibility of its interference fringes. High fringe visibility indicates strong spatial coherence, while low visibility suggests lower coherence.

By studying the visibility of the interference fringes across different baselines (*i.e.*, separations between telescopes), astronomers can infer properties of the observed object, such as its size, shape, and spatial distribution of emitting regions. However, this constitutes an inverse problem: the image must be retrieved from measurements in the frequency domain. Due to the under-constrained nature of this problem, several methods are used to fill the u,v plane. Multiple baselines as well as large apertures relative to baseline can be employed or even using the Earth rotation to scan the sky (for all ground-based nulling interferometers).

1.3 Going to space

Space interferometry offers two main advantages over ground-based facilities: freedom from atmospheric disturbances and the ability to configure larger baselines. Molecules in the atmosphere indeed selectively absorb specific parts of the electromagnetic spectrum, as depicted in Figure 1.4.

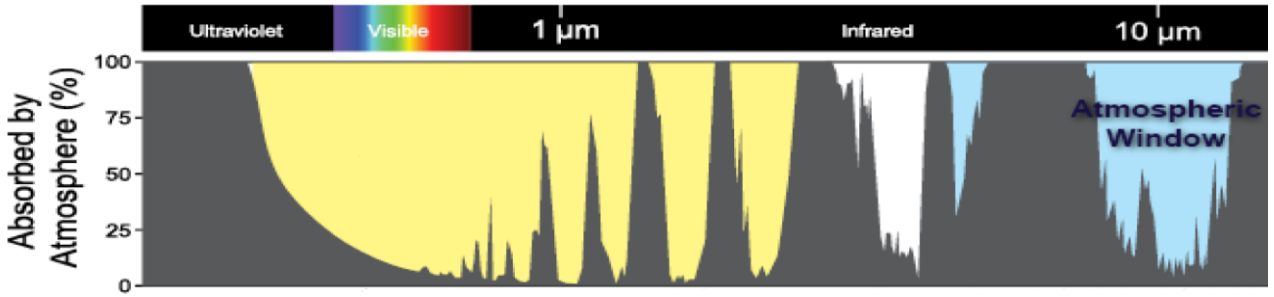

Figure 1.4: Atmospheric absorption of the electromagnetic spectrum [12].

While there exist atmospheric windows in the optical and radio wave ranges, the infrared domain at the heart of exoplanet detection is affected. Moreover, space-based interferometry eliminates atmospheric turbulence, allowing for longer integration times [8].

The quality of atmospheric optical transmission, particularly with respect to turbulence, can be assessed by the Fried parameter r_0 [13]. This parameter depends on random inhomogeneities in the atmosphere's refractive index so that telescope resolution might be limited due to atmospheric turbulence rather than diffraction. According to a Kolmogorov turbulent model, it behaves as $r_0 \sim \lambda^{6/5}$ [14], translating to approximately 10 cm in the visible domain and 50 cm in the infrared. This reinforces the advantage of space-based observations.

Space-based interferometry also allows for very long baselines and easy reconfiguration of arrays. The more stable environment in space, for example at Lagrangian points, facilitates alignment and calibration, and passive cooling of infrared instruments enables continuous observation.

1.4 IR domain

The optical design under consideration in this work operates within the mid-infrared (MIR) domain, spanning wavelengths from [3-20] µm, a range well-suited for exoplanet detection missions. This spectral region holds particular importance due to its ability to capture the absorption signatures of key molecules present in potentially viable planet atmospheres, commonly referred to as planetary bio-signatures. As a matter of fact, molecules such as water vapor (H_2O), carbon dioxide (CO_2), ozone (O_3) and methane (CH_4) give rise to distinctive spectral features [4], as illustrated in Figure 1.5.

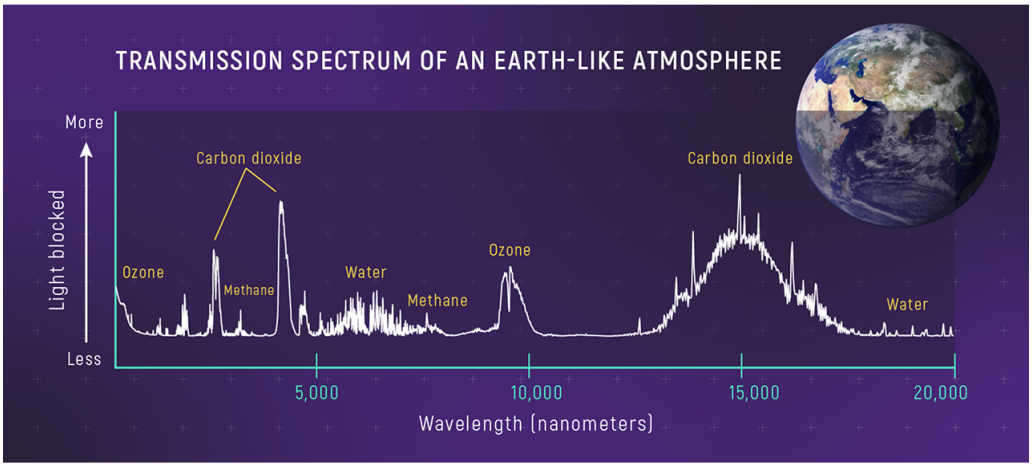

Figure 1.5: Spectral signature of Earth-like planet in the MIR domain [15].

Working within the MIR domain enables comprehensive analysis of exoplanetary atmospheres, including probing their composition and assessing thermal structures. Unlike the visible domain, where observations rely on reflected light, the MIR domain captures thermal emissions from the exoplanets themselves, offering unparalleled insights.

In addition, the MIR domain permits a better contrast, a better flux ratio, between the stellar emissions and those from neighboring planets in the sense of Planck's law of radiations Equation 1.6:

$$B_\lambda(\lambda, T) = \frac{2hc^2}{\lambda^5} \cdot \left(e^{\frac{hc}{\lambda kT}} - 1\right)^{-1} , \tag{1.6}$$

with B_λ [W/(m^2·µm· sr)] the spectral radiance, h [(m^2·kg)/s] the Planck constant, k [(m^2·kg)/(s^2·K^{-1})] the Boltzmann constant, λ [m] the wavelength and T [K] the temperature. This law governs the spectral radiance emitted by a blackbody at a given temperature. Wien's law of displacement further highlights the significance of the MIR domain by providing the peak emission wavelength:

$$\lambda_{\max} = \frac{2897.772}{T} [\mu m]. \tag{1.7}$$

Notably, Earth's thermal emission peaks around 11 µm.

Hence, the substantial difference in temperature between the parent star and the orbiting planet results in general in an amplification of the luminosity contrast. However, this ratio favors planet detection in the infrared domain as depicted in Figure 1.6.

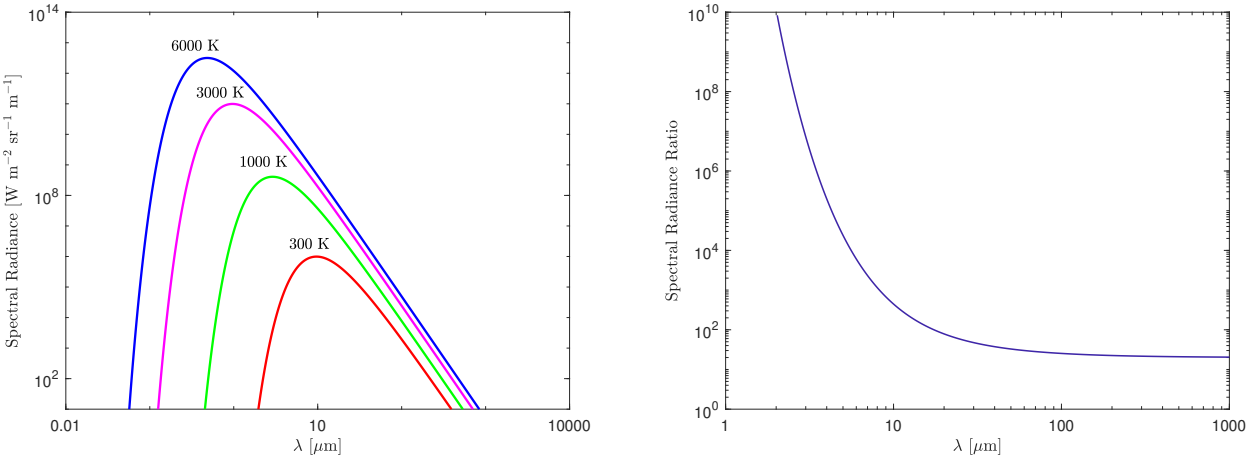

(a) Spectral radiance

(b) Spectral radiance ratio

Figure 1.6: Planck's distribution for different blackbody temperatures (a) and associated ratio of the red, typical of exoplanet emissions, and blue curves related to Sun-like stars (b).

Measuring this planetary thermal signature even constraints the effective temperature and radius of the detected exoplanet, a task challenging to accomplish using reflected light. Furthermore, using shorter wavelength results in a diminished contrast and poses technical challenges to the interferometer design.

1.5 Bracewell first concept

In 1978, Ronald N. Bracewell first introduced the groundbreaking concept of a two-element rotating nulling interferometer [16], as depicted in Figure 1.7.

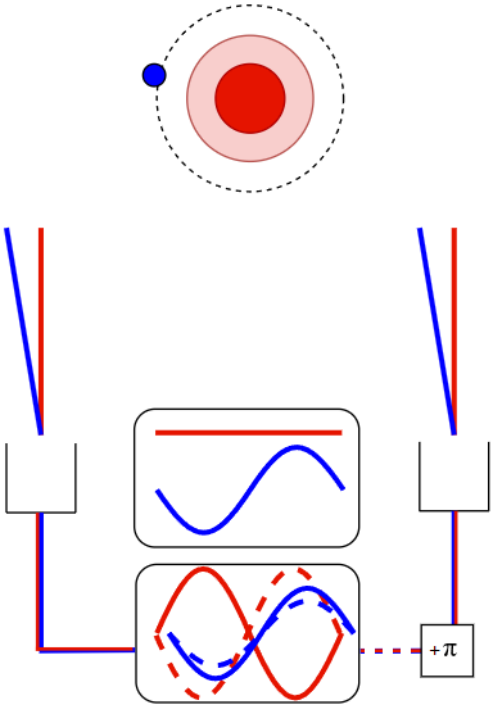

Figure 1.7: Representation of a Bracewell nulling interferometer for exoplanet detection. Collected by the two spacecrafts, the starlight is depicted in red whereas the exoplanet signal is represented in blue. The upper signals result from the interferences.

The nulling interferometer builds upon the principles of the two-element interferometer, where light is collected and interfered in a plane while ensuring coherence. However, it introduces an achromatic π-phase shift in one of the arms. This results in a fringe pattern that destructively interferes with on-axis light source, effectively cancelling the glare of the observed star. Consequently, it enables the detection of faint planetary systems free from their parent star's brightness. This produces a so called on-sky transmission map, akin to observing the sky through a sinusoidally varying transmission mask along the axis separating the telescopes.

Despite sufficient starlight reduction, detecting Earth-like planets with such a static array configuration is typically not possible due to the exozodiacal emission dominance. To address this, Bracewell proposed rotating the interferometer so that the planet's signal would be temporally modulated by alternately crossing high and low transmission regions. Meanwhile, the stellar signal and background emission would remain constant. The planetary signal could then be retrieved through synchronous demodulation.

This rotation eliminating on-axis symmetrical sources like exozodiacal disks or the star's corona is illustrated in Figure 1.8.

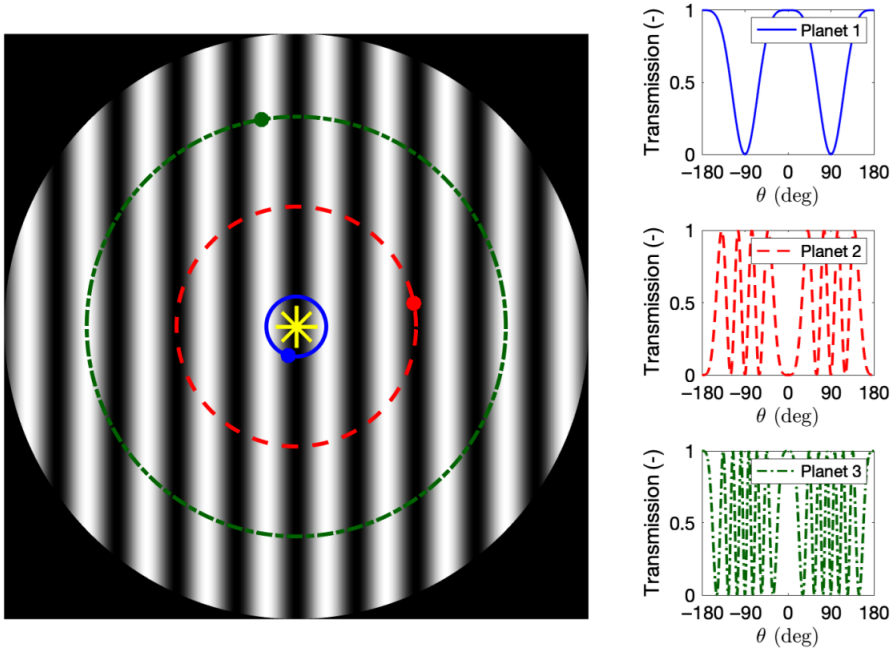

Figure 1.8: Modulation of the signal of three planets of increasing distance with respect to the parent star with nulling interferometry [17].

As can be seen, the number of extrema and modulation strength directly correlate with the planet's distance from the parent star. This first design is nonetheless sensitive to phase differences and lacks robustness in this aspect. In addition, stray sources within the field of view can reduce signal-to-noise ratio (SNR). Furthermore, the requirement for precise baseline rotation is a technical challenge for space-based observatories, potentially limiting the instrument's efficiency.

Despite these issues, Bracewell's pioneering concept laid the foundation for further developments in nulling interferometry, shaping the future of exoplanet detection.

1.6 Kernel improved interferometer

A more sophisticated nulling interferometer design was proposed and denoted Kernel, leveraging multiple baselines to enhance performance and robustness to phase perturbations [18]. This enhanced concept is depicted in Figure 1.9.

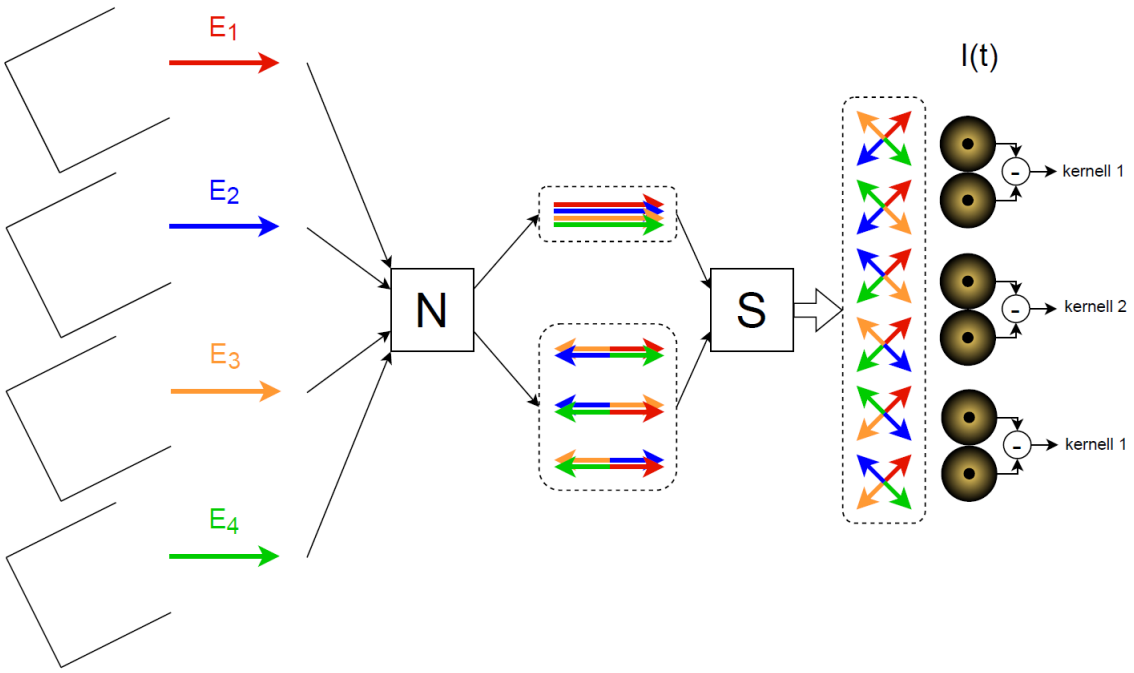

Figure 1.9: Kernel robust interferometer concept.

In this design, a π-phase shift is applied at the nuller N to the three possible combinations of signals, represented by the electric fields E_i. Subsequently, more complex pair switching S is implemented with a $\frac{\pi}{2}$-phase shift. Finally, the difference of these newly acquired signals defines the kernel outputs. Kernels are high-contrast observables that are insensitive to small perturbations. This approach exhibits superior performance compared to a simple Bracewell interferometer while also relaxing tolerances on the design [18].

The resulting transmission maps, however, are more complex, as depicted in Figure 1.10.

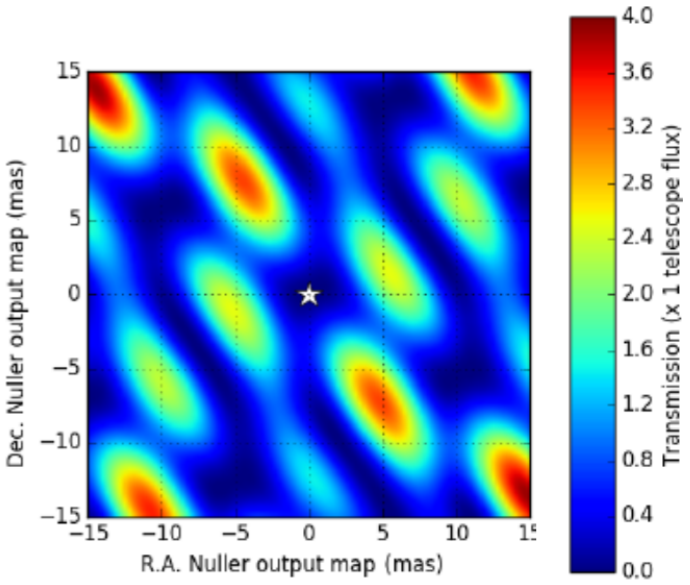

Figure 1.10: Kernel interferometer transmission maps [19]. The star is at the center and coordinates are given in terms of declination and right ascension [mas].

These maps display intricate patterns relative to the simple sinusoidal mask of the previous concept.

1.7 Phase chopping

The first implementations of the concept of baseline rotation to discriminate the planetary signal from the exozodiacal emissions were successively proposed by Angel and Woolf [20] and by Mennesson and Mariotti [21] in 1997. Angel and Woolf relied on the pronounced modulation of the exozodiacal emissions induced by the design symmetry occurring at twice the frequency of the baseline rotation. Conversely, Mennesson and Mariotti broke this symmetry using, for instance, five telescopes regularly located on a circle or ellipse. However, both configurations faced challenges due to the array's inability to rotate sufficiently fast, leaving them prone to low-frequency drifts originating from stray light, thermal emission, and detector gain.

To address this issue, the technique of phase chopping was suggested in 1997 by J.M. Mariotti [22]. Phase chopping is a calibration technique performed at the combination stage in nulling interferometry, where multiple ways of beam combination from various apertures exist. The principle involves synthesizing two different transmission maps with the same telescope array by applying different phase shifts during the beam combination process [23].

Essentially, phase chopping rapidly alternates the phase shift introduced, for example, between the two arms of a Double-Bracewell interferometer on timescales of seconds to minutes, much shorter than the typical integration times needed for detecting small exoplanets. This modulation helps calibrate out long-term drifts (*i.e.*, low-frequency noise) within the instrument [24]. By performing quick switches between the two transmission maps, phase chopping modulates the planet signal while leaving contributions from sources such as stellar emissions, local zodiacal cloud, exozodiacal cloud, stray light, thermal effects, and detector gain unaffected.

Phase chopping can be implemented in various ways, such as inherent and internal modulation [10], and is considered an essential component of future space-based life-searching missions.

The implementation of phase chopping can be achieved in a number of ways, such as inherent and internal modulation [10], and is seen as a key element of future space life-seeking missions.

1.8 Practical design of an interferometer

The structure of a single arm of a nulling interferometer typically consists of several components, each serving a specific purpose in the instrument's operation. Said components are organized as follows:

- Collecting optics;
- Transfer optics;
- Tip/tilt mirror and corresponding tip/tilt sensor;
- Optical delay line and optical path difference sensor;
- Deformable mirror and corresponding wavefront sensor;
- Phase shifter;
- Beam combiner;
- Modal filter;
- Science detection assembly.

The different components are investigated hereafter. As previously mentioned, a particular attention is given to the optics located upstream of the beam combiner.
These optics play indeed a critical role in collecting and correcting the incoming light from the celestial sources (star, exoplanets) before it reaches the beam combiner for further interference analysis and subsequent scientific observations.

1.8.1 Beam collection and transport

Celestial light can be collected using either telescopes or siderostats. A siderostat is a steerable and flat mirror that directs light directly to the interferometer or to a fixed horizontal telescope acting as a beam compressor. Both solutions are illustrated in Figure 1.11.

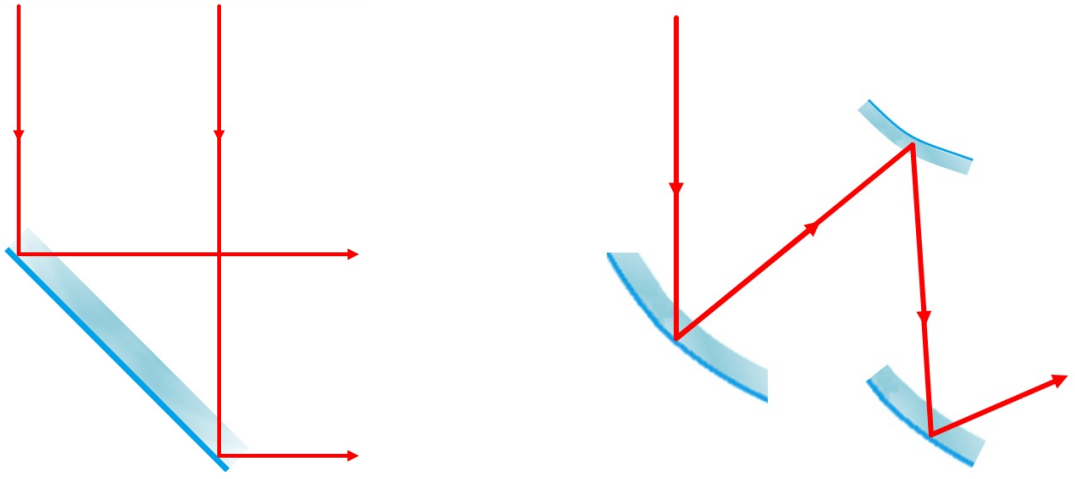

(a) Siderostat (b) Telescope

Figure 1.11: Illustrations of the two types of collecting optics.

The siderostat offers a simple design but has a limited field of view and may introduce optical aberrations for large angles. Additionally, due to the large beam it gathers, a siderostat requires a large secondary mirror, resulting in a less compact design.

On the other hand, a telescope provides a larger collecting area. An off-axis design also prevents blockage which is particulary important given the low throughput of nulling interferometers. Telescopes can be equipped with single or multiple apertures for greater design flexibility and degrees of freedom.

Subsequently, the collected light is transported through an optical train and directed to the beam combiner after correction. For instance, an afocal system comprising two confocal off-axis parabolic mirrors can be used to increase the magnification while maintaining the parallel nature of the beams.

A particular attention must be taken with respect to the mirror geometry and coatings to preserve the relative polarisation of the beams [10].

1.8.2 Beam correction

Beam correction plays a crucial role in nulling interferometry by ensuring coherence and maintaining high quality interference patterns. Said correction is achieved through the implementation of a tip/tilt mirror, adjusting the incoming light rays, and a deformable mirror, which addresses wavefront errors.

Both the tip/tilt mirror and the deformable mirror are essential for compensating for wavefront errors introduced by imperfections in optical elements, misalignment, or atmospheric turbulence (especially in ground-based facilities). These errors can significantly degrade the interferometric signal and reduce the nulling depth. The tip/tilt mirror primarily adjusts the tilt of the incoming wavefront, while the deformable mirror dynamically corrects more complex aberrations by altering its shape. It exists a direct link with the precision of the ADCS of the formation of satellites and the required corrections.

Moreover, these mirrors ensure precise alignment between the beams from the different collecting spacecrafts. The tip/tilt mirror permits fine adjustments in beam direction to achieve proper alignment before interference occurs.

In addition, nulling interferometers rely on precise phase control to achieve destructive interference of the starlight while allowing the planet's signal to pass through. The deformable mirror can thus introduce controlled phase shifts across the aperture to achieve the desired interference pattern. However, this is performed in many cases using an optical delay line, as discussed later in this section.

Alternatively, a deformable mirror can be directly used for adaptive optics, addressing both tip/tilt and wavefront errors simultaneously. With its ability to modify its shape precisely, multiple degrees of freedom, compact design, and rapid response time, it offers an attractive option [25].

These beam corrections significantly enhance therefore coherence of the light for proper interferometry quality. Figure 1.12 illustrates the two types of correcting mirror discussed.

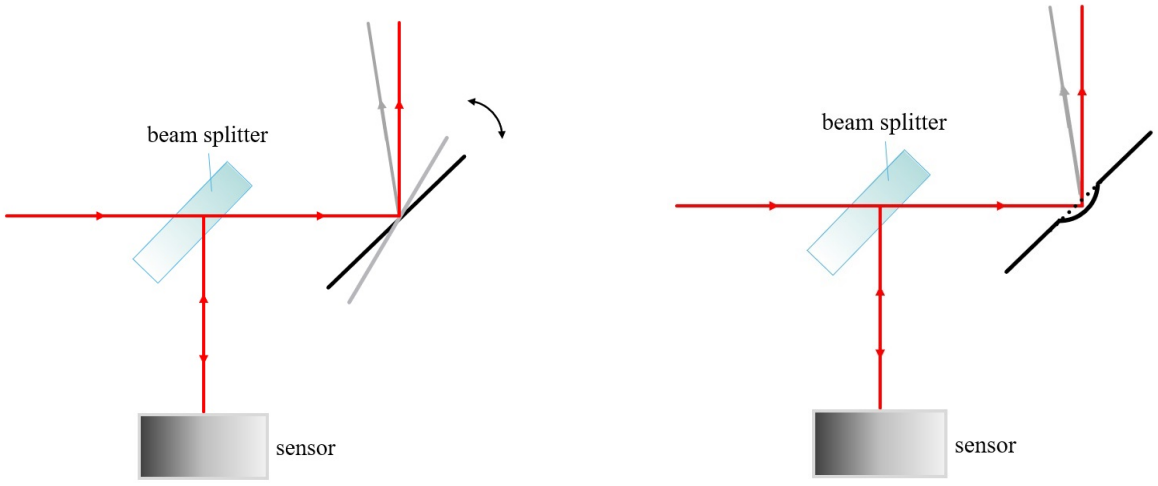

(a) Tip/tilt mirror (b) Deformable mirror

Figure 1.12: Illustrations of beam correction mirrors.

Both types of mirrors operate within a closed-loop system with feedback. Sensor measurements of the light are processed by a control system, which subsequently adjusts the shape or orientation of the mirror surface therefore ensuring continuous correction and monitoring to maintain interferometry quality.

As previously mentioned, an optical delay line is also present for equalizing optical path differences and ensuring coherence. It introduces a delay to the optical signal, which can be achieved through various methods such as increasing physical length (*e.g.*, coiling optical fiber or movable mirrors), changing the refractive index of the propagation medium, or utilizing phase arrays (*e.g.*, phase shifters or electronically controlled tunable delays). Regardless of the method used, automated control and monitoring of the optical path difference are required to maintain coherence throughout the optical layout. Another method involves retroreflection , as seen in 'cat's eyes' optical delay lines. A corner-cube structure induces multiple reflections of the light thus introducing a small delay. By adjusting the size and geometry, a desired delay can be achieved. Multiple retroreflectors can also be used in series. Figure 1.13 depicts for instance an optical delay line consisting of movable mirrors to achieve the required path difference and subsequent phase difference.

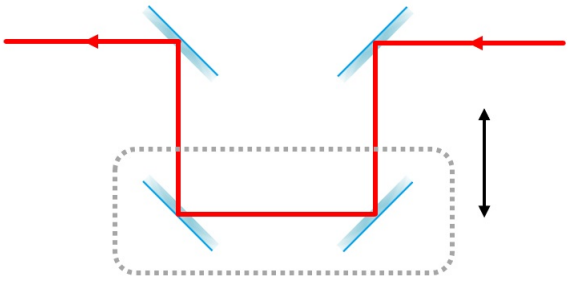

Figure 1.13: Illustration of a movable mirrors optical delay line.

In nulling interferometry, a π-phase shift must also be applied in one of the arms (for a two-element interferometer) or in multiple arms for more complex designs. This phase shift must be as exact

as possible to ensure sufficient quality and performance. While easily achieved for monochromatic light by modifying the optical path difference (OPD) between the two beams accordingly, this becomes a significant challenge for polychromatic starlight. To ensure this shift is achromatic, complex recombination systems are needed. For instance, the Achromatic Interferential Coronograph (AIC) [26] designed for the Darwin mission or the Mach-Zender beam combiner [27] used in the FKSI mission, two modified versions of traditional Michelson interferometers, can be cited. This achromatic shift is one of the major challenges of nulling interferometry but is out of scope of this work.

1.8.3 Fringe and angle trackers

Fringe and angle trackers operate alongside the main optical layout and play a pivotal role in achieving high-quality results.

The primary objective of a fringe tracker is to continuously monitor the interference pattern, detecting any deviations in position or intensity [28][29]. Such deviations may arise from vibrations, atmospheric disturbances (in ground-based interferometry), or other potential perturbations.

The general layout of a fringe or angle tracker is illustrated in Figure 1.14. The beam is split by a beam splitter and directed onto a detector to monitor any changes.

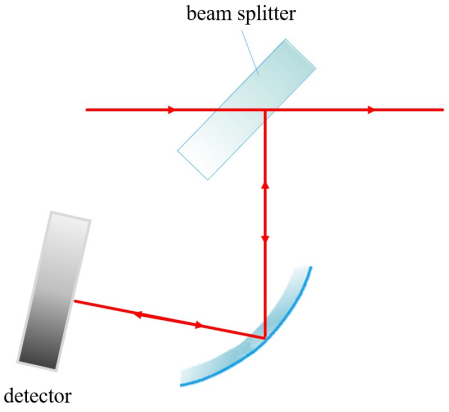

Figure 1.14: Illustration of a fringe/angle tracker.

Upon detecting any changes, the fringe tracker's control system performs corrective measures to realign the fringes to their original position and intensity by adjusting the optical interfaces of the design. This process, known as active retroaction, ensures continuous stabilization. Monitoring occurs constantly to maintain maximal stability of the pattern throughout the observation phase for high-quality results.

Similarly, an angle tracker is essential for maintaining the alignment between interfering beams. It continuously monitors the interference pattern and adjusts the angles of mirrors within the optical system, often utilizing piezoelectric actuators or motorized mounts. This mechanism relies on feedback as for beam correction mirrors.

In summary, both trackers are integral to interferometer design in the sense of the precision and stability of measurements they provide.

1.8.4 Beam combination and detection

Coaxial/Multiaxial combinations

The starlight, covering a wide range of wavelength as described by Planck's law defined previously, results in a wavelength-dependent interference pattern leading thus to reduced contrast and visibility. To avoid this phenomenon, measurements are therefore conducted at isolated wavelengths (narrow bands) to ensure sufficient contrast.

Two approaches of beam combination are commonly applied to maintain coherence between the different telescopes, namely coaxial and multiaxial combinations [30] [31], as schematized in Figure 1.15.

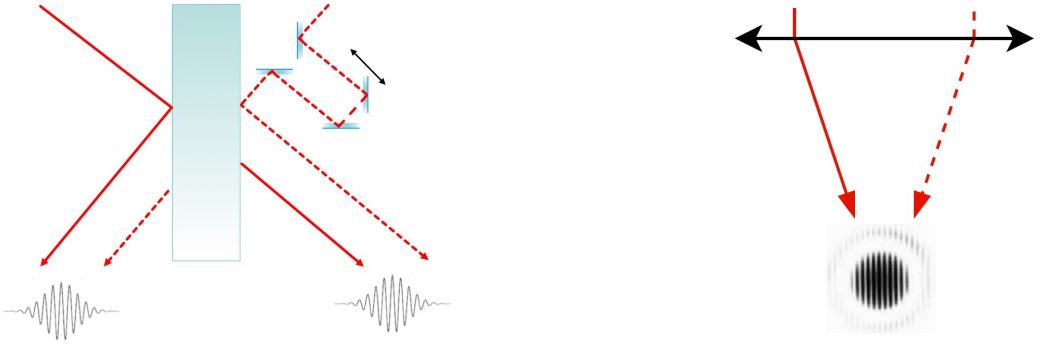

(a) Coaxial (b) Multiaxial

Figure 1.15: Two strategies of beam combination [8].

As depicted in Figure 1.15a, the coaxial strategy involves superposing the light from two telescopes by means of a 50/50 beam splitter. The process, taking place in the pupil plane, relies on encoding fringes temporally on two single-pixel detectors at each output of the beam splitter. A temporal modulation is subsequently performed by systematically modifying the optical path difference (OPD) with the introduction of additional delay of known amplitude. This can technically be achieved by using piezoelectric scanners. The coaxial strategy is thus similar to a Michelson-Morley interferometer. This technique is the most widely used today [23].

As depicted in Figure 1.15b, on the other hand, the multiaxial strategy exploits a common focus similar to Young's fringe experiment, with the combination occuring in the image plane. Fringes are spatially encoded on a focal plane array, resulting in modulation of the Airy pattern intensity due to varying delays between beams across this plane. In this method, the signal is recorded at one time but extends over several pixels on the detector plane, leading to spatial instead of temporal modulation. The coding of the spatial fringe is performed by placing the exit pupils at certain distances from each other and subsequently introducing geometric path differences to superimpose the beams. This can be achieved by using a simple lens [23].

Modal filtering

Modal filtering of the signal is also performed to reduce the aberrations and noise, thus achieving the desired nulling effect [10]. The use of single-mode fiber (SMF) [32] is especially effective to ensure that only a single spatial mode of light propagates through the system. By supporting only the fundamental spatial mode, SMF minimizes dispersion, ensuring that the output beam

maintains spatial coherence and enhance light purity. Modal filtering is nonetheless out of the scope of this work, focusing mainly on the pre-combination phase.

Detection

Finally, the planet's signal, free from starlight glare, is detected after passing through dispersive elements such as a spectrometer. This marks the attainment of tangible scientific results: the ultimate goal of a nulling interferometer. This thesis focuses on the optical design preceding the beam combiner stage to ensure the quality of these results, hence no further details are provided regarding the beam combination stage and subsequent detector assembly.

1.9 Response function

The schematic of the geometrical configuration of the interferometer in space is provided in Figure 1.16.

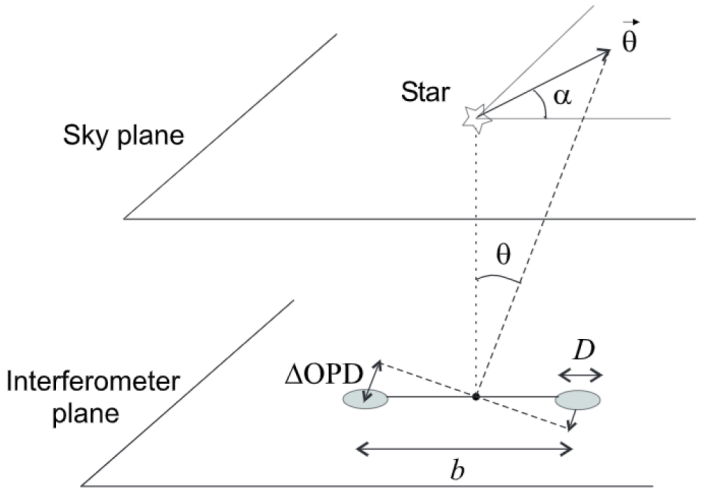

Figure 1.16: Geometrical configuration of a Bracewell interferometer with respect to the planes of interest: the interferometer and sky planes.

Following the formulation provided by Absil et al. [10], the instrument response or the wavelength-dependent intensity, denoted by R_λ, for a simple Bracewell interferometer is expressed as

$$R_\lambda(\theta,\alpha) = 2\sin^2\left(\pi\frac{b\theta}{\lambda}\cos\alpha\right) \approx 2\cdot\left(\pi\frac{b\theta}{\lambda}\cos\alpha\right)^2 , \tag{1.8}$$

where the parameters correspond to Figure 1.16 and the simplification stands for the small angle approximation.

The light is seen to be cancelled only on the optical axis, following a θ^2 relation slightly off-axis. This phenomenon, known as stellar leakage, occurs because a portion of the stellar light reaches the detector, *leaks*, without being fully nulled due to the finite size of the star's photosphere.

Figure 1.17 further illustrates the extinction profile of the response function of a simple Bracewell interferometer. In addition, a higher reduction profile is also depicted.

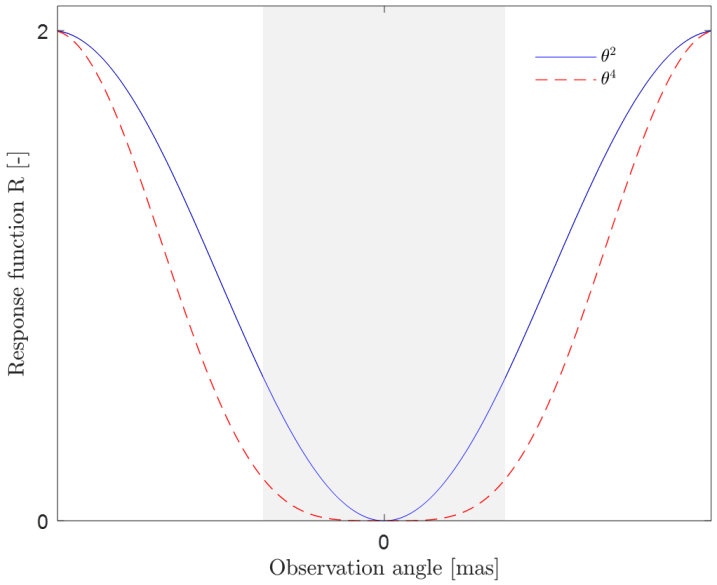

Figure 1.17: Different types of extinction profiles of the response function and associated stellar leakage.

To achieve an higher reduction, such as θ^4 in Figure 1.17, a minimum of three apertures is required, or specific beam combination strategies. These types of response function provide a better starlight reduction than a classical θ^2 curve. There is a steeper transition between bright and dark fringes, or in other words between constructive and destructive interferences, thereby improving the contrast. This results in a reduction of the stellar leakage [26], one of the major challenges in nulling interferometry. The hypothetical star chosen is Proxima Centauri, as explained in Section 6.3.

Another important figure of merit is the nulling ratio N, defined as the ratio of the transmitted stellar flux to the initial flux:

$$N = \frac{1}{\rho} = \frac{F_{leak}(\lambda)}{F_{init}(\lambda)} = \frac{\pi^2}{4} \cdot \left(\frac{b\theta_\star}{\lambda}\right)^2 , \tag{1.9}$$

where its inverse ρ denotes the rejection ratio.

Although a perfect interferometer will always exhibit stellar leakage, imperfections in the optical design can lead to instrumental stellar leakage including phase, wavefront, intensity or polarization errors resulting in a non-null on axis transmission [33][34].

These errors are further explained hereunder.

Phase:

Phase errors give rise to a shift in the position of the fringes of the transmission map. Hence, the main dark fringe is no longer centered resulting in non-null on axis transmission as expressed by

$$R_\lambda(0,0) = \frac{\Delta\phi^2(\lambda)}{4} \ , \tag{1.10}$$

with $\Delta\phi(\lambda)$ the small phase difference.

Wavefront:

Wavefront corrugation leads to a mismatch between the shapes of the two beams. By defining the phase variance over each pupil $\sigma^2_{\phi_{1/2}}$, the on-axis transmission becomes [32]

$$R_\lambda(0,0) = \frac{\left(\sigma^2_{\phi_1}(\lambda) + \sigma^2_{\phi_2}(\lambda)\right)}{4} \ . \tag{1.11}$$

Intensity:

Unequal intensities in the two arms induce also non-null transmission on the optical axis. Any additional amount of light does not interfere and therefore acts as background emissions. With ΔI the relative intensity error, it yields [33]

$$R_\lambda(0,0) = \frac{\Delta I^2(\lambda)}{16} \ . \tag{1.12}$$

Polarisation:

Multiple types of polarisation exists but can usually be decomposed into intensity and phase errors. For instance, a shift in the two components s and p of light is seen as a phase error while differential rotation signifies an intensity error [27]. It can then be shown that

$$R_\lambda(0,0) = \frac{\left(\Delta\phi^2_{s-p}(\lambda) + \alpha^2_{rot}(\lambda)\right)}{4} \ , \tag{1.13}$$

with $\Delta\phi_{s-p}$ the phase delay and α_{rot} the relative polarisation rotation angle.

1.10 Conclusions

Starting with an exploration of light wave properties, the foundation of nulling interferometry rests upon the principle of **interference**. At its core, this technique leverages destructive interference **to suppress starlight** glare to detect faint planetary signal. The pioneering introduction of the rotating nuller by Bracewell marked a significant breakthrough setting the stage for subsequent innovations such as the Kernel interferometer.

Going to space offers to suppress the atmospheric disturbances relative to ground-based interferometry facilities. In addition, operating within the mid-infrared (MIR) domain presents advantages by enhancing the contrast between stellar and planetary signals while facilitating atmospheric molecules' signatures detection.

The success of any interferometric system lies in the well-designed optical components to preserve coherence and maintain fringe contrast such as deformable mirrors, optical delay line or fringe tracker.

Optical elements to **ensure coherence** between the beams and maintain the fringe contrast such as deformable mirrors, optical delay line or fringe tracker are essential for a well-designed interferometer. However, instrumental limitations are inherent to interferometer design. Vigilant monitoring of beam quality becomes imperative to mitigate these constraints and uphold the performance of the interferometer.

Chapter 2

Instrumentations for nulling interferometry

Contents

2.1 Ground-based instruments 26
2.1.1 LBTI 26
2.1.2 VLTI 28
2.2 Space-based ideas and concepts 29
2.2.1 Brief history 29
2.2.2 Darwin/TPF-I project 29
2.2.3 Darwin/TPF-I demonstrators 30
2.3 Space-based rebirth: LIFE mission 35
2.4 Conclusions 36

This chapter delves into the nulling interferometry instrumentations, with a particular focus on the optical layout preceding the combination stage. It first describes **ground-based instruments**. Since limits exist for ground-based nulling interferometry, an overview of the ideas and concepts for **space-based missions** is investigated. In particular, the history of space-based instruments is overlined with a particular focus on the Darwin/TPF-I project and its precursors. Finally, the future of space interferometry will be explored with the LIFE initiative, the living legacy of the past concepts.

Through this missions examinations, insights are extracted for the possibilities and capabilities of different optical designs. By evaluating the performance and identifying bottlenecks of these concepts, critical parameters can be discerned with the ultimate aim of enhancing the optical design aspect.

2.1 Ground-based instruments

Only ground-based instruments for nulling interferometry are actually in use. As these interferometers are ground-based, adaptive optics are essential to mitigate atmospheric effects and background emissions.

2.1.1 LBTI

The Large Binocular Telescope Interferometer (LBTI), located on 3,300 m Mount Graham in the Pinaleno Mountains of southeastern Arizona, United States, comprises two 8.4 m diameter mirrors

mounted on a common altazimuth mount [35]. It is part of the Mount Graham International Observatory. Collectively, they provide a collecting area equivalent to a single 11.8 m mirror. On the other hand, the coherent combination of the two apertures signals provides images with spatial resolution equivalent to a 22.8-meter telescope.

A depiction of the LBT is presented in Figure 2.1.

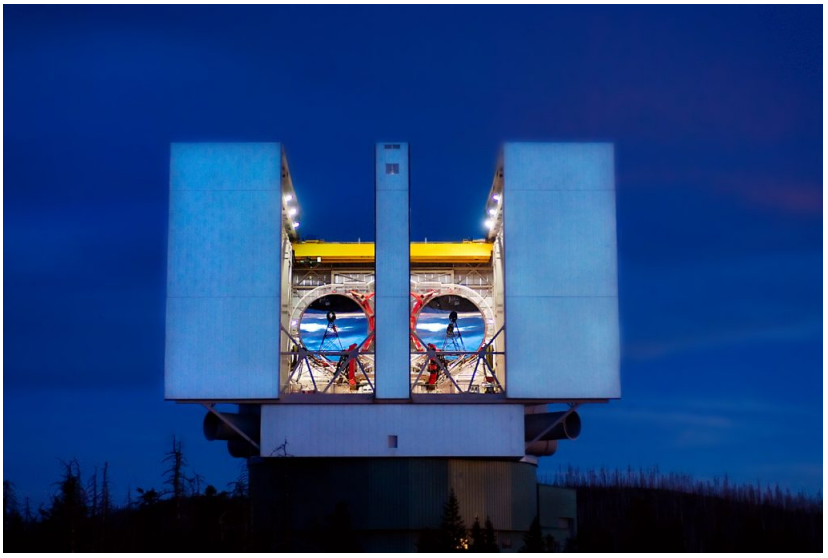

Figure 2.1: Image of the LBT [35].

The nulling interferometry mode of the LBT features a baseline of 14.4 m and enables observations in the spectral range [2.9-13] µm, sometimes called MIR N-band. It uses the natural Earth rotation to perform baseline rotation and scan the sky.

It was designed and funded by NASA to detect exozodiacal dust for the TFI/Darwin mission (see next section) [36].

A recent use of the LBTI was to capitalize on a Junovan eclipse to image thermal radiation from volcanic activity on the surface of Io, a Galilean moon over a range of parallactic angles [37].

2.1.2 VLTI

The Very Large Telescope Interferometer (VLTI), located on Cerro Paranal in the Atacama Desert of northern Chile, is an astronomical facility operated by the European Southern Observatory since 1998. It comprises four telescopes with diameters of 8.2 m and four mobile telescopes with diameters of 1.8 m. The achievable baselines range from 8 to 160 m.

A depiction of the VLTI is provided in Figure 2.2.

Figure 2.2: Image of the VLTI [8].

As all nulling interferometers, it will synthetize a large telescope whose angular resolution is equivalent to that of a telescope with a diameter equal to the largest baseline between the telescopes used. It also uses the natural Earth rotation to rotate the baseline.

The future of the VLTI lies in future visitor instruments such as the NOTT instrument for nulling interferometry (Nulling Observations of exoplaneTs and dusT), formerly Hi-5 (High-contrast Interferometry to $5\,\mu m$) [38]. Large ground-based interferometer such as the LBTI allows to achieve contrast up to 10^{-4}, whereas NOTT would be able to leverage sharp angular resolution of the VLTI with high-contrast capabilities up to 10^{-5} according to recent studies [38]. With this higher contrast and longer baselines that the future 30m-class extremely large telescopes armada will offer, the VLTI will be a keystone in various scientific areas such as exozodiacal disks observations or planet formation. Moreover, it will serve as a key technology demonstrator for future missions as LIFE, later discussed [39].

Debuted in 2017, this project involving the CSL was really presented and received fundings in 2019 [39].

2.2 Space-based ideas and concepts

Since ground-based instruments suffer from numerous limitations as explained in chapter 1, space-based missions is the next step forward.

2.2.1 Brief history

First introduced by Ronald Bracewell in 1978 [16], the concept of nulling interferometer was resurrected in 1990 during the discussion about the future NASA Next Generation Space Telescope, eventully becoming the James Webb Space Telescope [20]. Later in 1993, a european consortium led by the CNRS proposed the idea of an infrared nulling interferometer for Earth-like planets detection and their associated spectra analysis. This project, named DARWIN, was finally proposed to the Horizon 2000 Plus program of the European Space Agency (ESA) [32]. In parallel, a similar concept to the DARWIN one was considered on NASA's side in 1999 and named Terrestrial Planet Finder (TPF) [40]. Even though DARWIN and TPF gathered support and evolved over the years, these concepts were finally abandonned. Recently, new projects nonetheless re-emerged as their legacy, due to a better comprehension of the problematic and major technological breakthroughs.

2.2.2 Darwin/TPF-I project

The Darwin interferometer by ESA and the Terrestrial Path Finder - Interferometer by NASA were thus parallel space projects aimed at exoplanet detection in the MIR during the 2000s [41][42]. These projects proposed several architectures from 4 to 8 telescopes operating within the wavelength band of [6-20] µm with a desired field of view (FOV) of 1 as. The final concept proposed was the Emma X-array design, as illustrated in Figure 2.3 (a tribute to Darwin's wife).

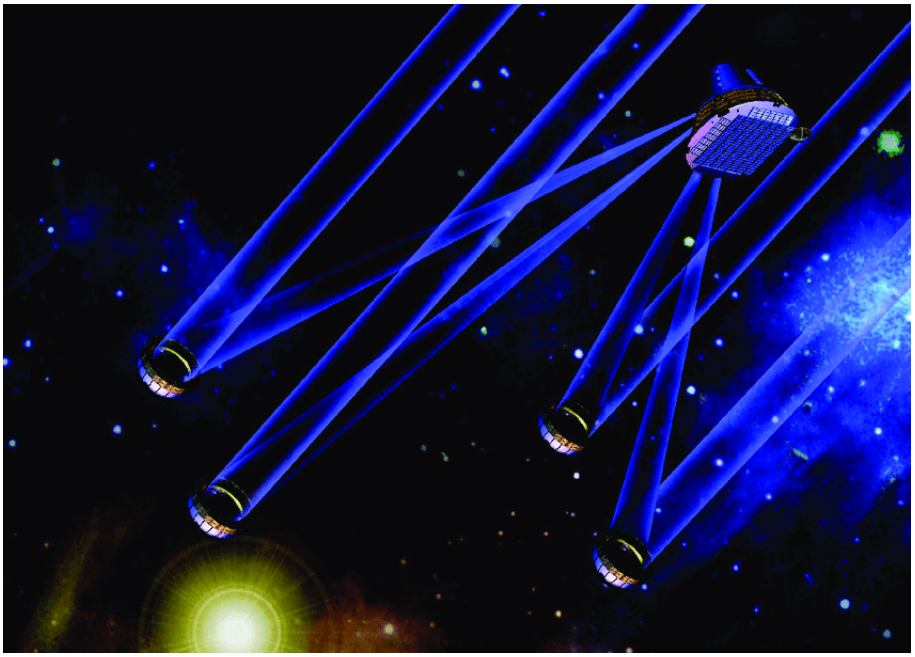

Figure 2.3: Artist illustration of the Emma X-array interferometer design.

The technical parameters of the Emma X-array design are detailed in Table 2.1, retrieved from [43].

Table 2.1: Emma X-array interferometer design specifications.

Collectors	four 2 m diameter spherical mirrors	**FOV**	1 as
Wavelength range	[6-20] µm	**Null depth**	10^{-5}
Inner working angle	[13-43] mas	**Spectral resolution** $\Delta\lambda/\lambda$	25
Angular resolution	[2.4-8.2] mas	**Temperature**	50 K

The wavelength-dependent properties are provided for $\lambda = 10\,\mu m$ and the collectors are diffraction limited at $2\,\mu m$. The baseline between the different collectors can be adjusted while the beam combiner spacecraft is located 1 km away from the collectors' plane.

2.2.3 Darwin/TPF-I demonstrators

Since Darwin and TPF-I evolved and grew over the years, demonstrators for key technologies were necessary to align with their final designs.

FKSI

The Fourier-Kelvin Stellar Interferometer (FKSI) is a concept for a structurally-connected nulling interferometer proposed by NASA in 2003 [44]. It was designed to detect giant planets, nearby superstars and exozodiacal disks [8], serving as a precursor for the TPF-I mission. An artist's impression of the FKSI mission is provided in Figure 2.4.

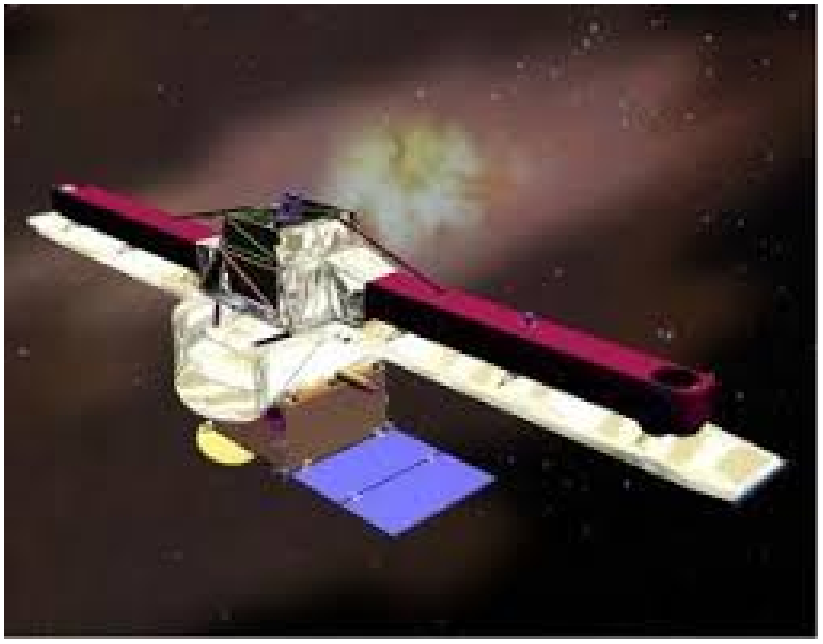

Figure 2.4: Artist illustration of the FKSI interferometer design.

The final optical system design of the FKSI is represented in Figure 2.5.

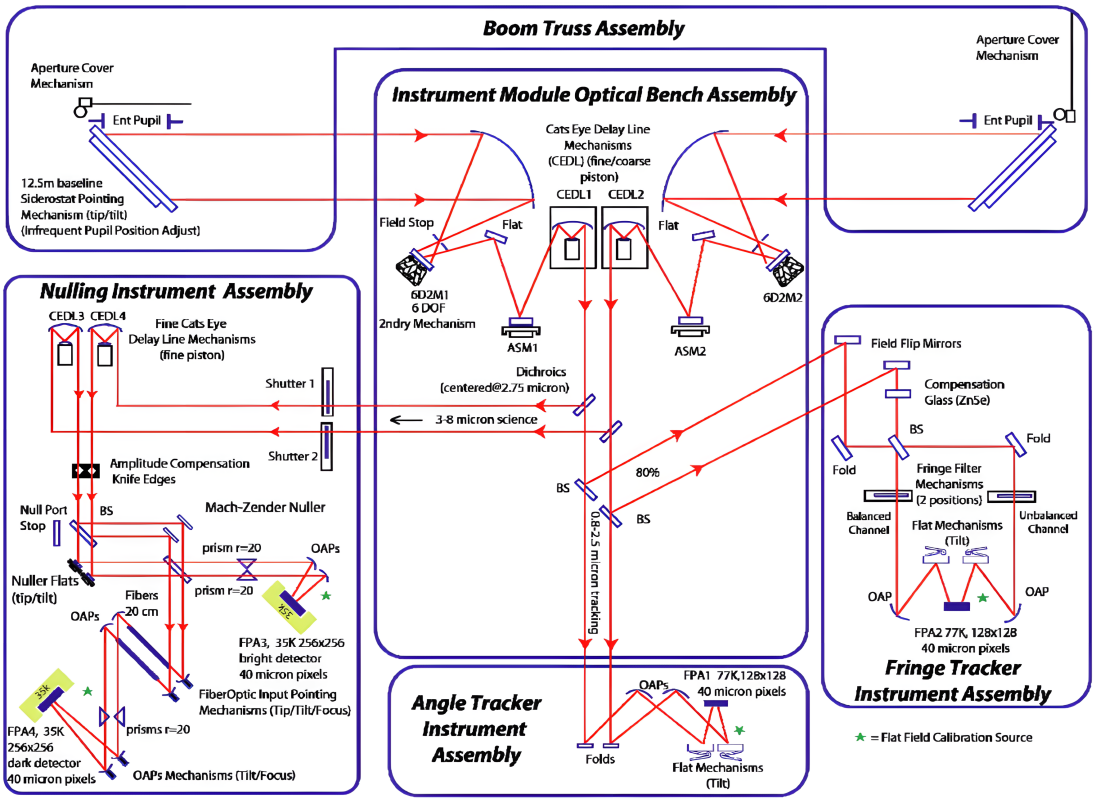

Figure 2.5: Schematic of the optical design of the FKSI.

This nulling interferometer configuration is intended to work in the spectral range [3-8] µm. It comprises two siderostats of 0.5 m diameter separated by a baseline of 12.5 m. The plane mirrors of these siderostats are inclined at 45 degrees for the light to travel towards the center of the satellite. Subsequently, the beam is fed into a symmetric Mach-Zehnder beam combiner through an off-axis parabola. A cat's eyes delay line ensures correct coherence maintenance. In addition, the light passes by a null tracker and a fiber wavefront error reducer to achieve a required null depth of $N = 10^{-4}$. Finally, it is focused on a detector cooled to 35 K. Fringe and angle trackers are also included in parallel with the main optics.

PEGASE

The PEGASE mission was a nulling inteferometer that aimed to conduct spectral analysis in the domain [1.5-6] µm, targeting hot jupiters around nearby stars, brown dwarves and providing high-resolution measurements of protoplanetary disks [45]. It was designed to serve as a precursor for TPF-I. An artist's impression of this concept is depicted in Figure 2.6.

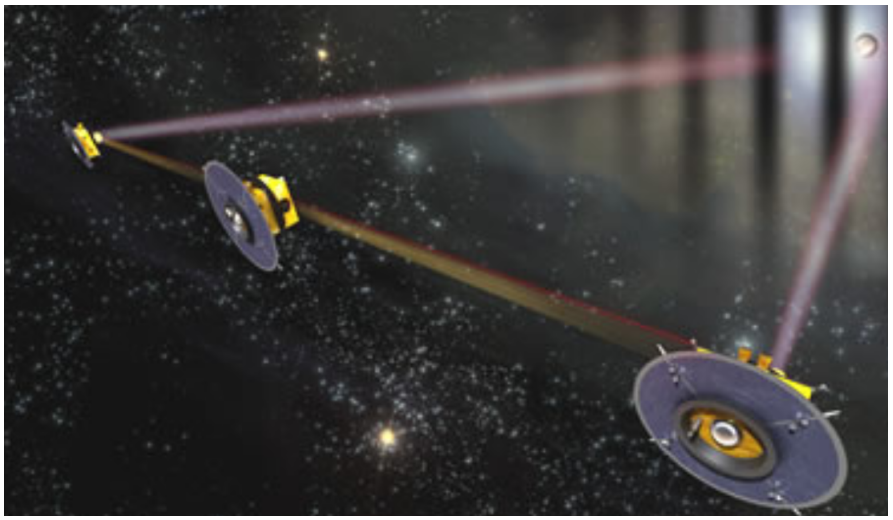

Figure 2.6: Illustration of the PEGASE interferometer.

The optical layout of PEGASE is provided in Figure 2.7.

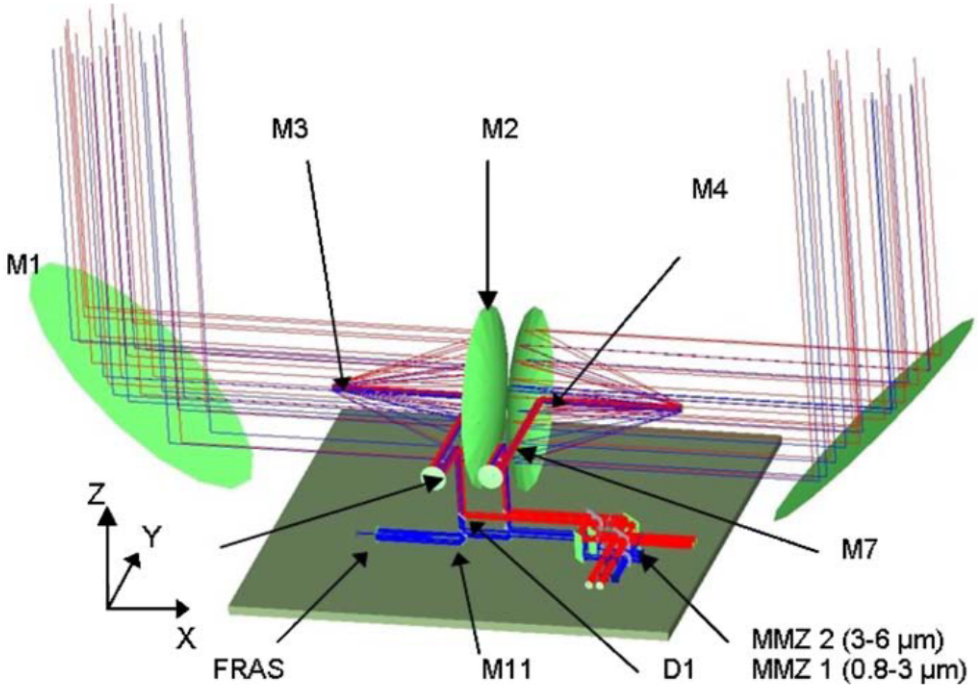

Figure 2.7: Schematic of the optical system of the PEGASE mission.

It consists of a simple Bracewell interferometer with two siderostats arranged in a linear formation with the beam combiner spacecraft. Both mirrors of the collector elements (M1) are inclined at 45

degrees with an aperture diameter of 0.4 m. Subsequent mirrors (M2 and M3) form a simple afocal of magnification 20, ensuring no net divergence or convergence of the light. Taking advantage of the field reversal by reflection, an achromatic phase shift of π is achieved using M1 and M4, the latter being a small flat mirror. A fringe sensor and an optical delay line of the 'cat's eyes' type are also included. The baseline of this concept could vary from 40 to 500 m with spatial resolution ranging between 0.5 and 30 mas.

CINDIS

The Cold Interferometric Nulling Demonstration in Space (CINDIS) aimed to demonstrate key technologies for the TPF mission, prioritizing technical advancements over scientific objectives [46]. With a budget of less than 300M $, its objectives included achieving high-contrast nulling interferometry at a 10 µm wavelength, implementing vibration control strategies, instrument pointing/path control, stray light control, and potentially demonstrating a 4-aperture compound nulling. Its primary objective was nonetheless to demonstrate a stable null. An illustration of the CINDIS mission is provided in Figure 2.8.

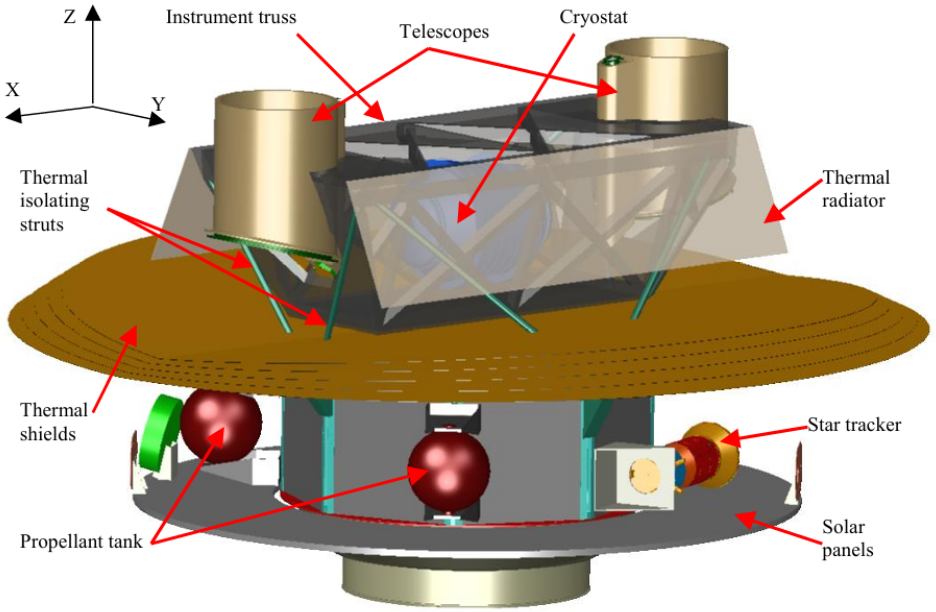

Figure 2.8: Illustration of the CINDIS interferometer [46].

The optical layout of the CINDIS mission is outlined in Figure 2.9.

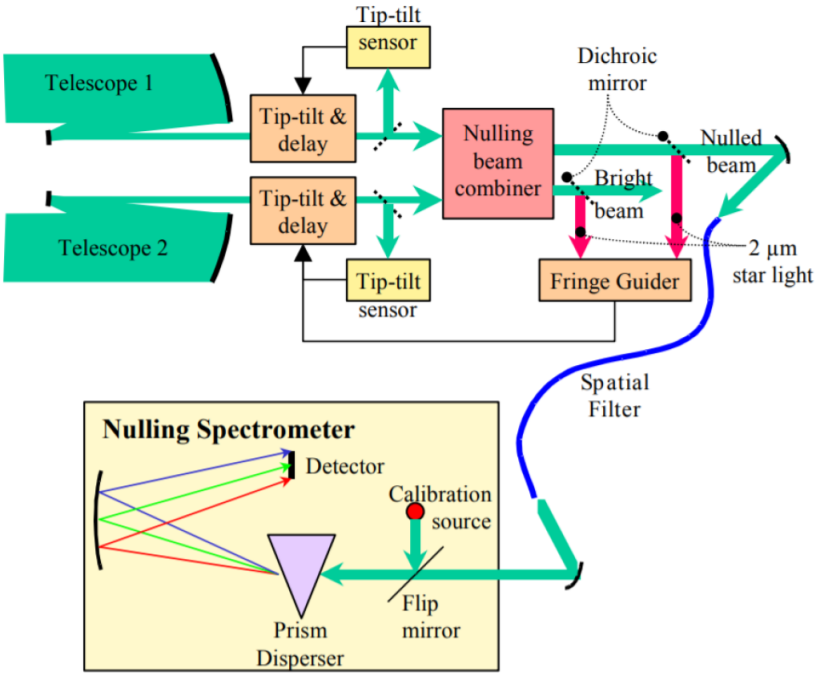

Figure 2.9: Schematic of the optical system of the CINDIS mission [46].

It forms a simple Bracewell nulling interferometer with a null depth of around 10^{-5} with a short 2 m structurally fixed baseline. The spectral band of interest is [6-12] µm. The system employs two off-axis Cassegrain telescopes with a 40 cm aperture diameter to collect and direct the light onto a fast steering mirror (FSM). Both primary and secondary mirrors of the telescopes are confocal coaxial paraboloids, resulting in unobstructed 4 cm diameter output beams when coupled with off-axis pupils. The following FMSs monitor tip-tilt to ensure wavefront quality for the beam combiner. The optical delay line consists of a simple piston actuator with a total stroke of near 30 µm in one of the interferometer arms to adjust the optical path difference of the two beams. Additionally, a fringe tracker is present. Spatial filtering and scientific assembly are not discussed.

2.3 Space-based rebirth: LIFE mission

The Large Interferometer For Exoplanets (LIFE) builds upon previous concepts such as Darwin/TPF-I [24]. It aims to assess the atmospheric composition of a significant numbers of terrestrial exoplanets to address the fundamental question: "Are we alone in the universe?".

Officially initiated in 2018, the LIFE project has been in its initial study phase since 2020, following community building efforts. While many technologies required for space interferometry were immature at the time of Darwin, advancements such as formation flying and deep nulling have now reached a technology readiness level (TRL) of 5. The components have therefore been tested and validated in their relevant environment, making the mission concept feasible. An artist's impression of this mission is depicted in Figure 2.10.

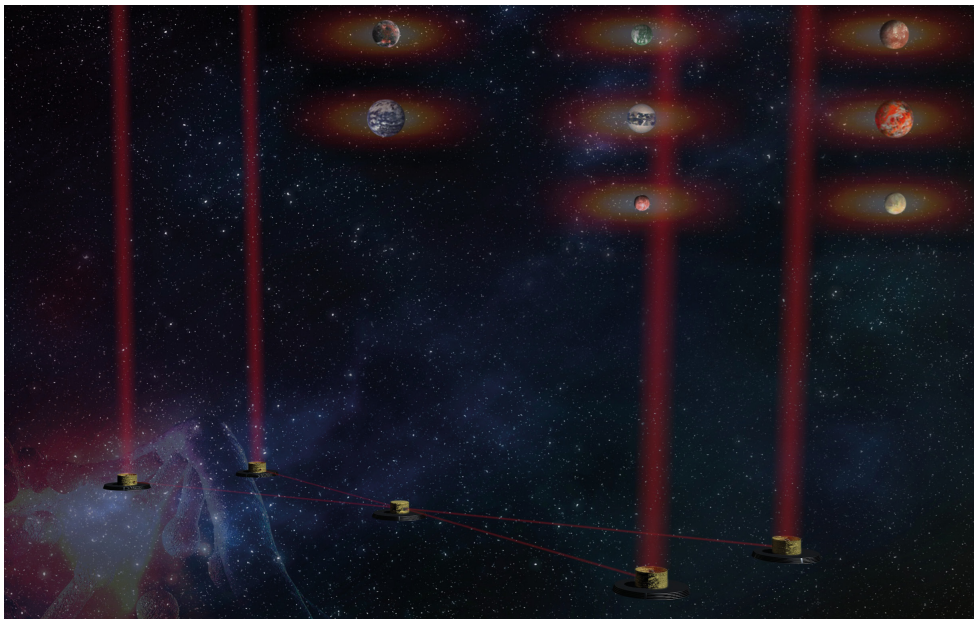

Figure 2.10: Artist illustration of the LIFE space mission design [24].

Since the mission is still in the study phase, parameters have not been finalized [24]. However, it is likely to consist of four collector spacecrafts and a beam combiner one to better discriminate axis-symmetric emissions with respect to a simple two-collector model. Numerous trade-off are being conducted to determine the optimal aperture diameter and associated signal-to-noise ratio (SNR). The aperture diameter is varied from 1 to 3.5 m with a fixed throughput of 5% and a SNR of 7 [47]. The spectral domain of interest is of [4-18.5] µm and the instrument would be cooled to 40 K [24].

2.4 Conclusions

During the 2000s, **various space nulling interferometer concepts** were proposed. However, many of these missions were abandoned due to the immaturity of the required technologies at the time. Consequently, only ground-based interferometer facilities are currently in use, which are subjected to atmospheric disturbances. While adaptive optics enable these ground facilities to reach their maximum potential, the advantages offered by space-based interferometry, such as longer possible baselines and freedom from atmospheric perturbations, are undeniable. Now, with advancements in technologies such as formation flying and deep nulling, initiatives like LIFE are being reconsidered. What seemed impossible yesterday has become conceivable today. Building on these key ideas, the next chapter will focus on designing two optical systems.

Chapter 3

Optical design of a nulling interferometer

Contents

3.1 Architecture **38**
3.2 Dimensioning **40**
3.3 CodeV designs **44**
3.3.1 Siderostat-Confocal Hybrid Optic (SCoHo) 44
3.3.2 Direct Confocal Setup (DiCoS) 46
3.4 Conclusions **48**

This chapter reviews and examines various options for nulling **optic design** and subsequently proposes two different configurations of light-gathering optic system based on previous concepts. Firstly, the influence of the main parameters is investigated regarding the design's capabilities. The **dimensioning** and **choices** made are then discussed and studied through trade-off analysis as an initial approach before future optimization in a subsequent section. Finally, the configurations are implemented using the **CodeV software** for further analysis in the following section. These two optical designs **will serve as the foundation for validating the performance modeling tool** developed in the subsequent chapter.

3.1 Architecture

Following a top-down approach, different numbers and configurations of the collecting spacecraft are possible, as exemplified by the different concepts outlined in chapter 2. Possible geometries are provided in Figure 3.1.

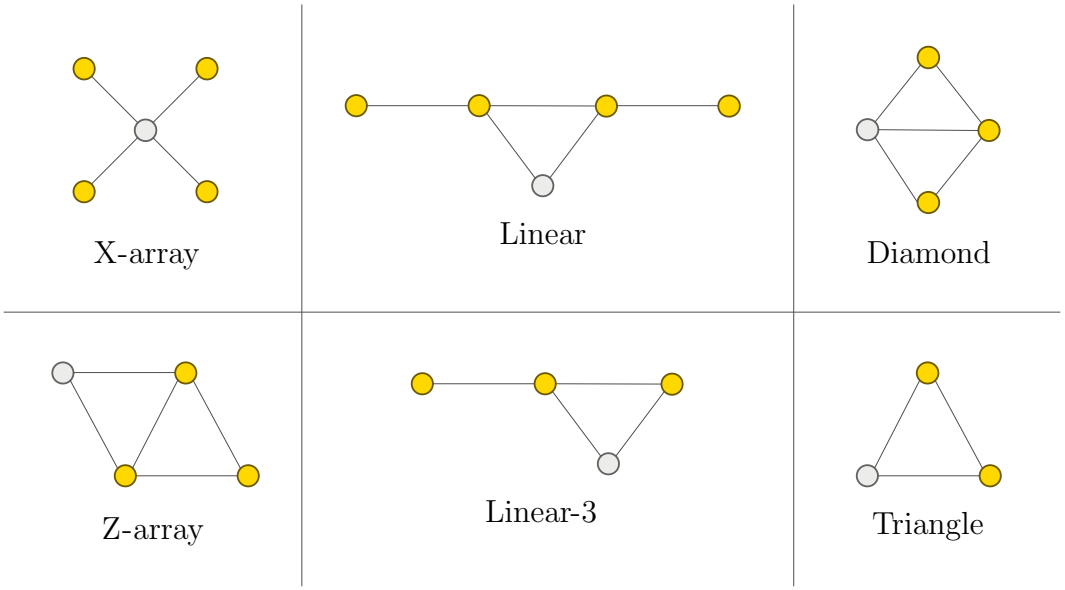

Figure 3.1: Exemple of configurations for space nulling interferometers.

These configurations can be discriminated based on factors such as stellar leakage, feasibility of flying formation, or overall costs. Since this thesis focuses on the optical design before combination, the choice of the telescope, or more generally, the collecting spacecraft, can be made independently of the overall configuration as an initial consideration. To streamline the work, a simple rotating Bracewell interferometer is initially considered.

Whether the combination is performed using a single-mode fiber or classical pupil plane recombination, the telescope acts as a simple beam compressor and aims to produce a collimated beam. Its design can be made independently of the following stages.

Different types of collecting spacecraft exist, as represented in Figure 3.2.

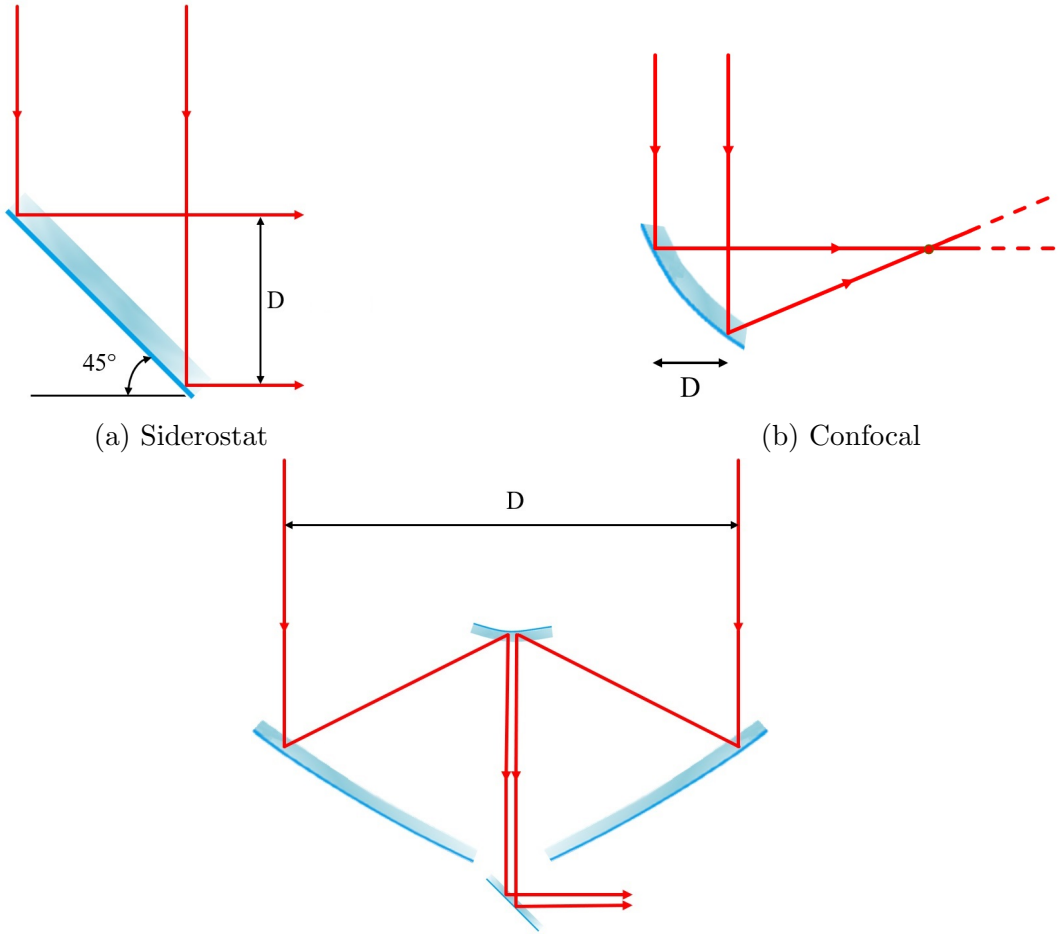

(a) Siderostat

(b) Confocal

(c) Cassegrain type

Figure 3.2: Schematic of main telescope choices for nulling interferometry.

The first type depicted in Figure 3.2a consists of a simple siderostat. It is easy to manufacture but requires a large secondary mirror for the confocal part, increasing the weight and size of the design. On the other hand, it allows for easy correction of the incoming ray's path if there are calibration or tracking errors.

The second type, illustrated in Figure 3.2b, consists directly of a confocal system. Therefore, there is no need for a large secondary mirror, allowing for the useful utilization of the great value of the baseline for the parameter S, which leads to a compact design. Moreover, it requires fewer optical surfaces, but they are more difficult to manufacture and polarisation problems may arise. Problems in tracking are also tedious to mitigate compared to a simple siderostat.

Finally, the Cassegrain-type telescope is represented in Figure 3.2c. On-axis telescopes present fewer aberrations, and these aberrations are also more easily reduced. They can tackle tracking error just like a simple siderostat but require numerous mirrors. The main disadvantage of the on-axis design is the central obstruction, which leads to a reduced collecting area in an instrument with already very low throughput. Off-axis variants correspond in a sense to schematics 1 and 2.

3.2 Dimensioning

Several parameters define and influence the capabilities of a light-gathering device, such as the f-number ($F\#$), aperture diameter (D), magnification (M), or even the size of the optic system (S). For a nulling interferometer, the baseline (b) is obviously of great importance as well, even though it does not directly impact the design of a single arm of the interferometer. The influence of these parameters is investigated below.

The baseline b and the aperture diameter D shape the overall geometry of the interferometer most significantly, as illustrated in Figure 3.3.

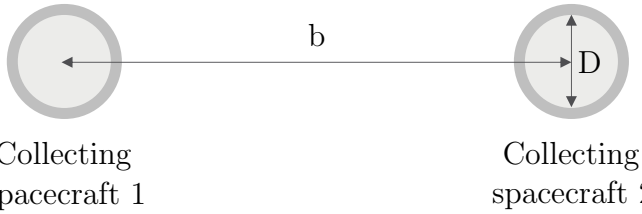

Figure 3.3: Schematic of the baseline and aperture diameter of a nulling interferometer.

These two parameters allow to define the so-called inner and outer working angles (IWA and OWA, respectively), given by

$$IWA = \frac{\lambda}{b} \tag{3.1}$$

and

$$OWA = \frac{\lambda}{D} \ . \tag{3.2}$$

While the baseline with the IWA drives the resolution of the instrument, as discussed in chapter 1 with the fringes, the diameter with the OWA drives the sensitivity and theoretical field of view. The smaller the telescope, the larger the field of view, but the smaller the sensitivity. However, the specific problem of the FOV in nulling interferometry is tackled later on.

The IWA in combination with the OWA also provides an estimation of the number of observable exoplanets with the instrument, as illustrated in Figure 3.4 for $\lambda = 10\,\mu\text{m}$ and a similar design to FKSI.

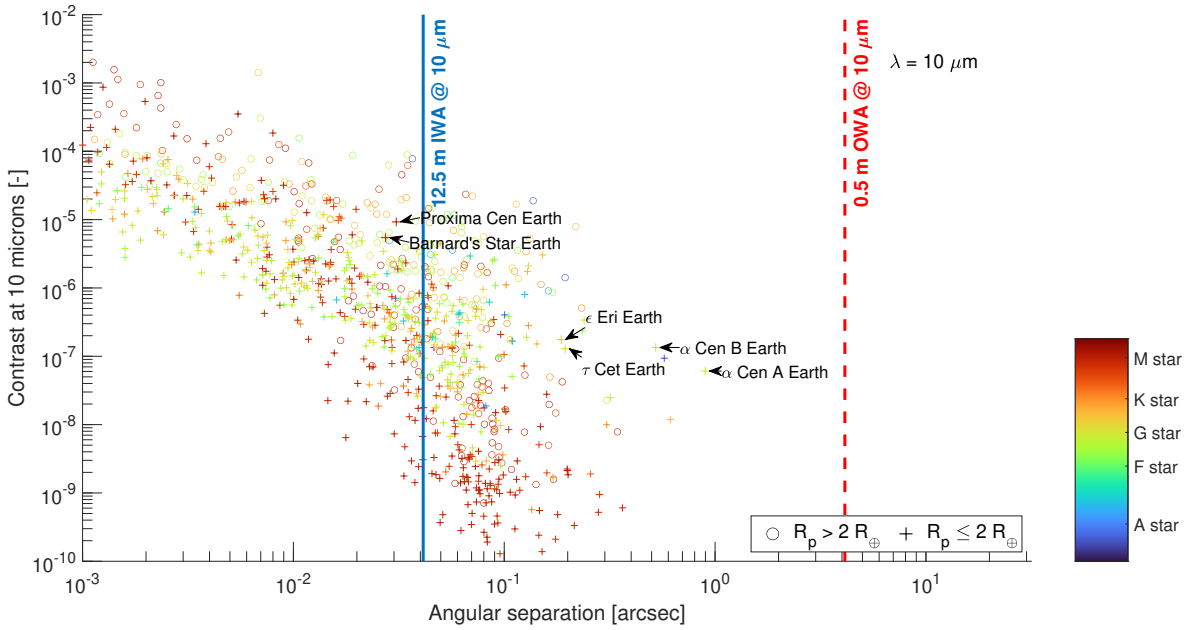

Figure 3.4: Number of observable rocky planets depending on the IWA and OWA (courtesy of C. Dandumont). A distinction is made between exoplanets of more, or of less than twice the Earth radius, respectively denoted by a circle or a cross.

This set of angles indeed constrains the angle between the exoplanet and its parent star that can be detected by the instrument. A trade-off also arises with the photon flux gathered by the instrument. While the OWA can be increased by decreasing D, the collecting area of the instrument is proportional to D^2, and a sufficient amount of photons must be gathered by the instrument to ensure high-quality measurements and not degrade the signal-to-noise ratio. On the other hand, a reduced D can also mitigate background noise. The aperture diameter is also intrinsically related to the technology and materials limits. High values of D require specific materials, since not all materials can be used to manufacture large mirrors, or the use of segmented parts must be considered [48].

For a generic telescope, the f-number is essential to its design. The higher the f-number, the higher the diffraction, as expressed previously by Rayleigh's criterion. However, the aberration tends to approach a near-perfect Dirac representation. The overall quality of the optical system is then expressed by the convolution of the Dirac representation from the aberration part and the extended diffraction pattern. By analogy, this is represented by a low curvature or, equivalently, a high radius of curvature lens. On the other hand, the lower the f-number, the higher the aberrations and the lower the diffraction. This corresponds to a high curvature or, equivalently, a low radius of curvature lens.

However, the field of view is nearly inexistant for nulling interferometry. This is because rocky planets orbiting distant stars are observed. For instance, the angular separation of the nearest star to the Sun, Proxima Centauri, and its first orbiting planet, Proxima Centauri B, lies in the milliarcsecond range.

Furthermore, producing mirror with lower f-numbers is increasingly difficult. Therefore, considering all constraints, a rule of thumb is to use f-numbers in the range [3-10] [49].

The f-number is therefore less relevant for interferometer design. For instance, if the beam is first focused before combination by passing through a single-mode fiber, the f-number can be changed by the focusing element (*e.g.* a simple converging lens). Since the light-gathering optic acts merely as a beam compressor, essentially forming an afocal system, the f-number does not have direct importance in the design.

A more critical factor for the design is the magnification M of the beam compressor. The magnification refers to that of the confocal system consisting of two parabolas. It aims to narrow the beam while maintaining the rays parallel for the beam combination phase. The beam must not be narrowed too much to prevent auto-interference (interference between rays of the same beam) but it should be sufficient.

The choices of D, M and indirectly $F\#$ are not independent, and another important factor also needs to be taken into account: the size (S) of the optical system.

The size of the optical system is mainly due to the confocal system. Denoting the first and second parabolas by 1 and 2, the relationships governing the confocal system are as follows:

$$\begin{aligned} F\#_1 &= \frac{f_1}{D_1}, & f_1 &= \frac{r_1}{2}; \\ F\#_2 &= \frac{f_2}{D_2}, & f_2 &= \frac{r_2}{2}; \\ S &= f_1 + f_2, & M &= \frac{f_2}{f_1} = \frac{D_2}{D_1}. \end{aligned} \tag{3.3}$$

It is inferred that higher f-numbers lead to less compactness, resulting in a higher value of S.

Figure 3.5 illustrates the influence of the previously defined parameters on the compactness of the design.

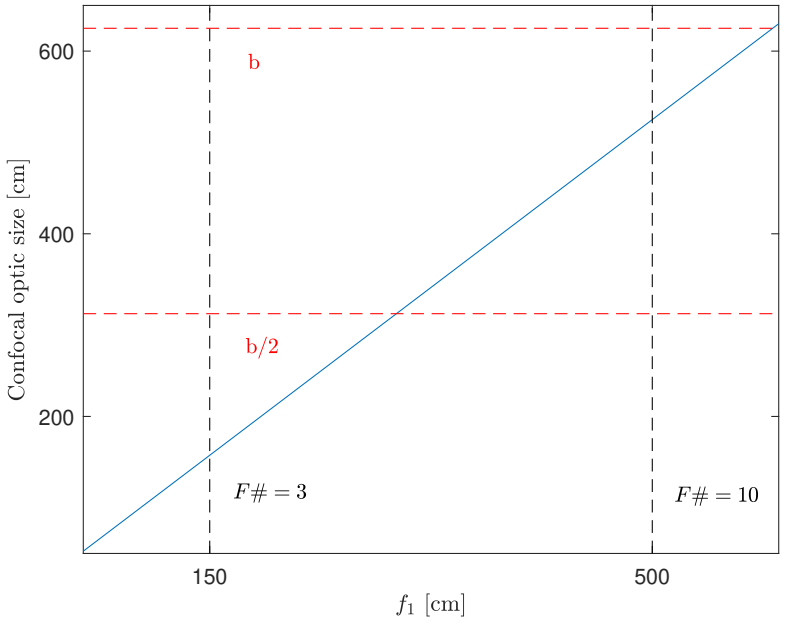

Figure 3.5: Influence of the focal length of the first mirror on the confocal optic size S.

As can be observed in Figure 3.5, the direct use of a confocal system as the first mirrors allows for utilizing the full length of the baseline, resulting in a higher f-number. On the other hand, the use of a siderostat before the confocal system imposes constraints, making the system more compact with a lower f-number, as the baseline cannot be fully utilized. The range of f-number and the size of the design with respect to the baseline are also displayed. Parameters and configurations choices will take into account the relationship between each parameter and the constraints outlined by Figure 3.5.

3.3 CodeV designs

Based on the previous investigations, we have designed two different configurations with an aperture diameter $D = 50$ cm and a magnification $M = 20$, following the FKSI concept as an initial approach, and implemented them in CodeV.

The first configuration implements a siderostat before conveying the light to the confocal system. Hence, an f-number of 3 is chosen to improve the compactness of the design.

The second configuration consists directly of a confocal system, which will also act as the primary optical surface encountered by the light. This system allows the utilization of the baseline as a useful length for the confocal system, and the f-number can be increased to 10.

Each configuration is further explained below.

3.3.1 Siderostat-Confocal Hybrid Optic (SCoHo)

The first configuration, also known as SCoHo (Siderostat-Confocal Hybrid Optic), implements a siderostat as the initial optical surface before using the confocal system for light gathering, as depicted in Figure 3.6.

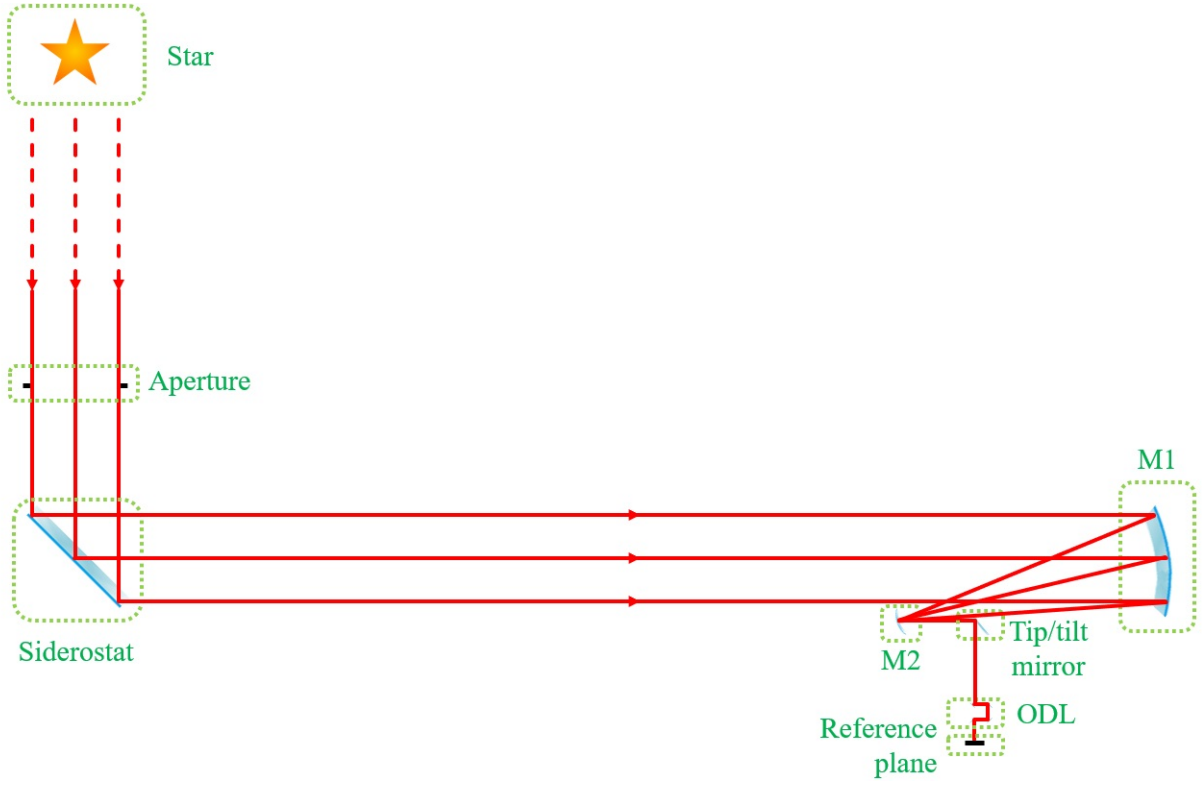

Figure 3.6: SCoHo schematic design and ray tracing, implemented and created in CodeV.

This figure illustrates only the pre-combining stage of the optical design, which is the focus of this master's thesis.

The SCoHo light gathering system is further illustrated in Figure 3.7.

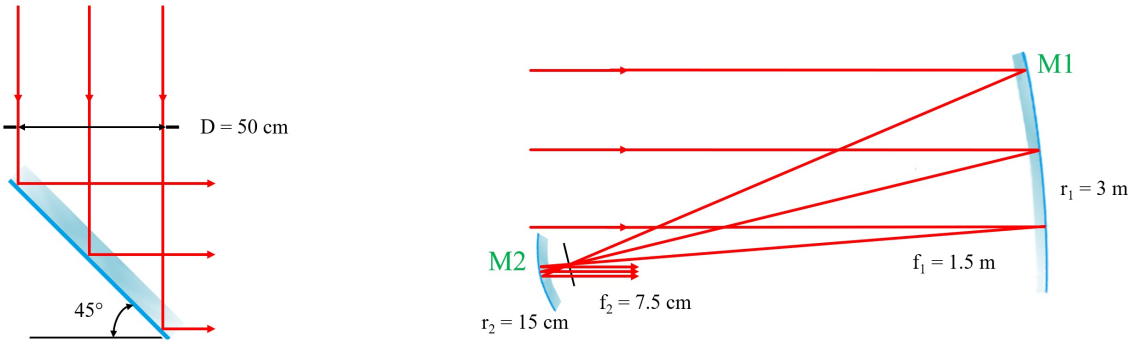

(a) Siderostat (b) Confocal system

Figure 3.7: First configuration: light gathering.

The siderostat is inclined by 45 degrees and covers the entire aperture before conveying the light to a confocal system consisting of a primary mirror with a curvature of 300 cm and a secondary mirror of 15 cm. Both mirrors have a parabolic shape, described by the equation:

$$z = \frac{x^2}{4R}\ , \tag{3.4}$$

where z is the sag of the mirror surface, x is the radial distance from the optical axis, and R is the radius of curvature. This equation represents the surface profile of each mirror.

This design is similar to FKSI in many ways, and the use of the siderostat, even though it requires a large secondary mirror, allows for easy recalibration with respect to a first powered mirror. The siderostat also offers easier manufacturing.

Coherence maintenance and eventual corrections are performed afterwards by an optical delay line and a tip/tilt mirror, as illustrated in Figure 3.8.

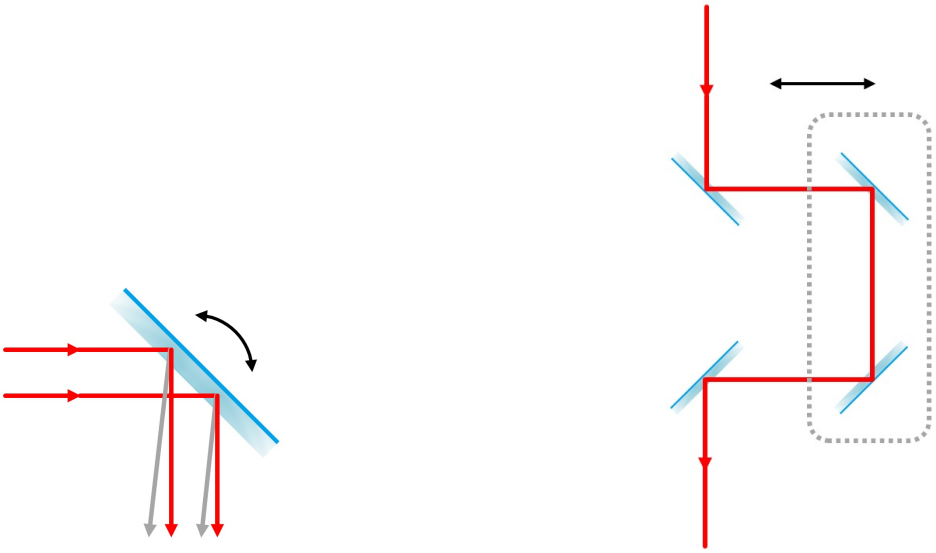

(a) Tip/tilt mirror (b) Optical delay line

Figure 3.8: First configuration: correction and coherence maintenance.

No further details are provided as these are standard elements for ensuring coherence maintenance.

3.3.2 Direct Confocal Setup (DiCoS)

The second configuration, also known as DiCoS (Direct Confocal Setup), directly consists of the confocal system made by the primary and secondary parabolic mirrors, as illustrated in Figure 3.9.

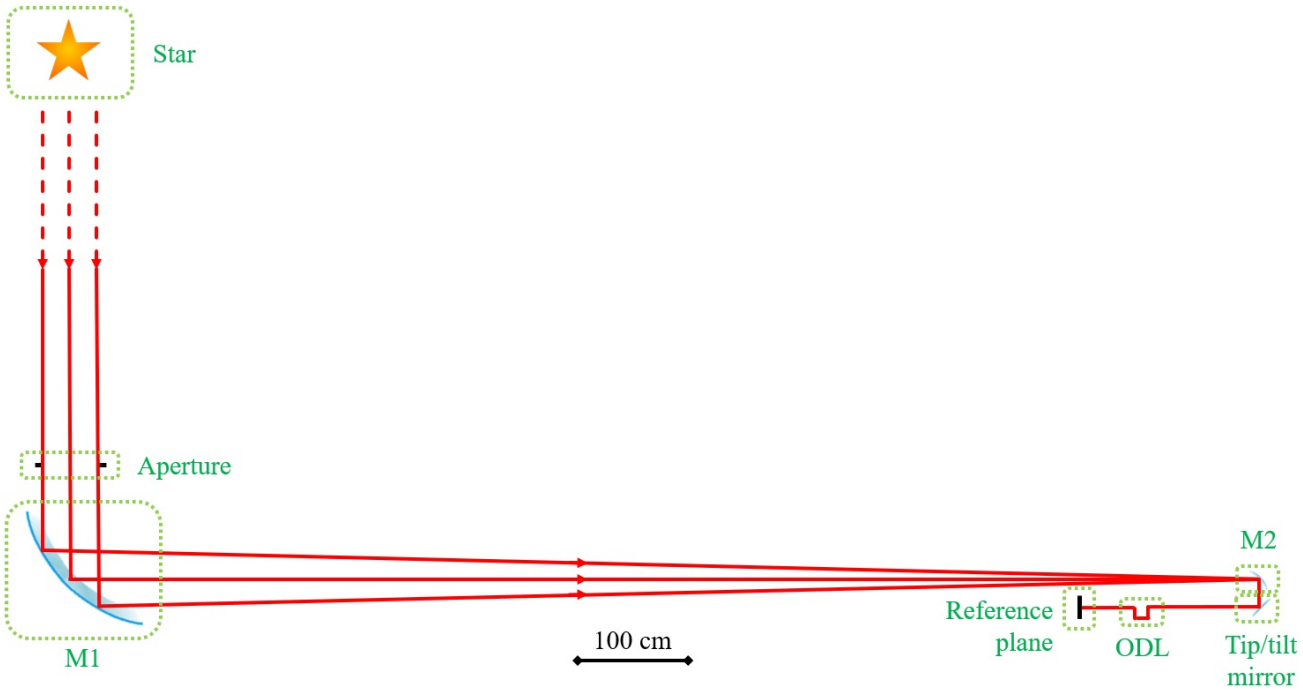

Figure 3.9: DiCoS schematic design and ray tracing, implemented and made in CodeV.

Once again, only the pre-combining stage is represented.

The DiCoS confocal system is further depicted in Figure 3.10.

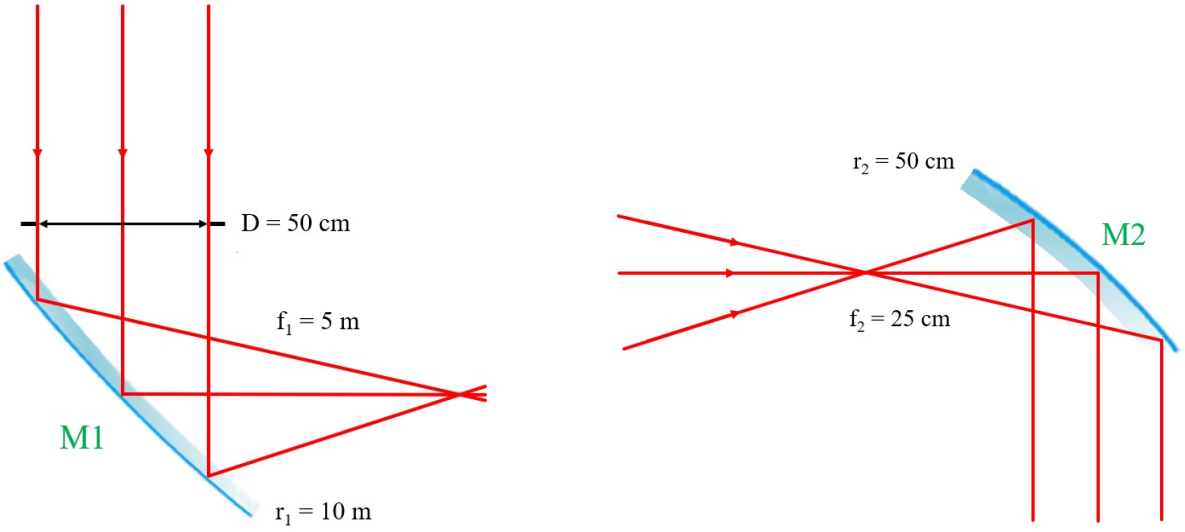

(a) Primary mirror (b) Secondary mirror

Figure 3.10: Second configuration: light gathering.

The primary mirror exhibits a curvature of 1000 cm, resulting in the secondary mirror having a curvature of 50 cm to achieve a 20 magnification. Calibration is more challenging with a curved first mirror, but there is no need for a secondary large mirror. This design can be seen as a modified version of the FKSI.

Coherence maintenance and eventual corrections are also performed afterward by an optical delay line and a tip/tilt mirror, represented in Figure 3.11.

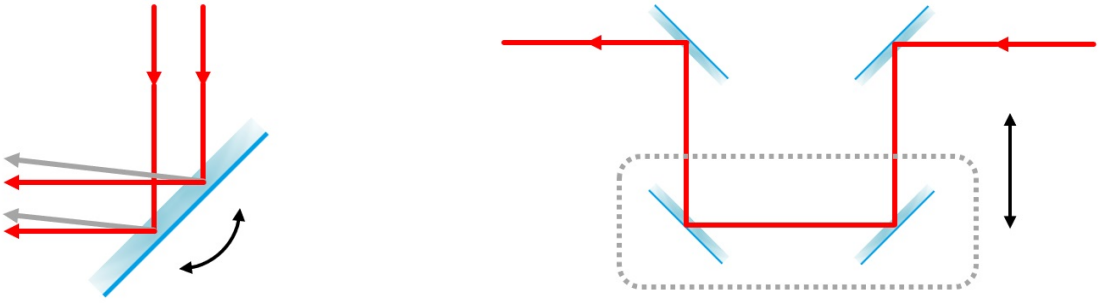

(a) Tip/tilt mirror (b) Optical delay line

Figure 3.11: Second configuration: correction and coherence maintenance.

This last part is similar to the SCoHo configuration.

3.4 Conclusions

In this chapter, two distinct configurations for interferometric systems, namely the **SCoHo (Siderostat-Confocal Hybrid Optic)** and **DiCoS (Direct Confocal Setup)** were proposed and designed in CodeV. These configurations **will be used to test the performance modeling tool** developed in the next chapter.

The SCoHo configuration integrates a siderostat as the initial optical surface, followed by a confocal system, while the DiCoS configuration directly implements the confocal system without the use of a siderostat.

Features comparison reveals several key differences between the two configurations. SCoHo offers advantages in coherence maintenance and ease of calibration due to the inclusion of the simple siderostat. However, it requires a larger secondary mirror, resulting in increased weight, size, and reduced compactness. On the other hand, DiCoS achieves a more compact design by eliminating the siderostat, leading to potential benefits in terms of weight and size reduction, albeit at the expense of some challenges in tracking error mitigation.

Design considerations highlighted the importance of factors such as baseline length, aperture diameter, and optical surface curvature in determining the performance and feasibility of interferometric systems. Overall, this investigation sheds light on the design considerations and trade-offs involved in the development of interferometric systems.

Chapter 4

Performance modeling tool

Contents

4.1 The need for tolerancing 49
4.2 Extraction of output parameters from CodeV 51
4.2.1 Optical Path Distribution 52
4.2.2 Relative Phase Distribution 53
4.2.3 Interference Intensity 54
4.3 Derivation of the response function 56
4.3.1 Choice of the figure of merit 56
4.3.2 On-axis analytical development 57
4.3.3 Off-axis analytical development 59
4.4 Tolerance analysis interpretations 65
4.5 Conclusions 68

This chapter focuses on developing a **performance modeling tool** for a nulling space interferometer and is the **heart of this master's thesis**. This tool aims to assess both on-axis and off-axis observation performance and enables performing tolerancing and sensitivity analysis of interferometer designs such as SCoHo and DiCoS. Through such analysis, insights into the sensitivity of interference quality to perturbations can be gained, and conclusions can eventually be drawn. Firstly describing the importance of tolerancing, the chapter goes on by presenting the methodology, and particularizing it for both types of observations. A rigorous convergence analysis is provided in the appendices. The following chapters will provide an overview of the capabilities of this newly developped tool in tolerancing and sensitivity analysis to demonstrate its robustness and usefullness.

4.1 The need for tolerancing

Tolerancing in space nulling interferometry and optics, in general, is of paramount importance. This method is critical to ensure the expected optical system performance in the harsh and variable conditions of the cosmos and to account for manufacturing and alignment errors. In outer space, optical instruments undergo radiation, mechanical stresses, and extreme temperatures, all of which can affect and degrade their alignment and performance. Tolerancing allows setting acceptable

limits for deviations in the main parameters, ensuring the optical system still operates correctly within these deviations. It is mandatory for achieving the high precision and accuracy required for space optics, ensuring system reliability and robustness, and balancing the need between cost and feasibility [50] [51].

For nulling interferometry, in particular, tolerancing is crucial to maintain the extremely low wavefront errors needed to achieve the desired null depth (typically in the range of 10^{-4} to 10^{-6} [10]). Hence, this requires tight tolerances on the surface quality of the mirrors as well as for the alignment of the different optical components. Precise alignment is essential for controlling the path length difference in the interferometer arms within a fraction of the wavelength of light to achieve effective nulling. The coherence length L_c for both SCoHo and DiCoS is indeed $\lambda/25$. By definition, the coherence length is given by

$$L_c = \frac{\lambda^2}{\Delta\lambda} \ , \tag{4.1}$$

with $\frac{\Delta\lambda}{\lambda}$ the wavelength resolution of the optic system.

By considering an equivalent resolution to the FKSI for both configurations studied, $L_c = 0.4\,\mu\text{m}$ for the wavelength of interest.

Thermal stability must also be enforced, although this is less of a problem for space nulling interferometry missions typically launched to Lagrangian Point 2 (L2), a semi-stable point in the gravitational field created by the Earth and the Sun located approximately 1.5 million kilometers away from Earth. L2 provides a stable thermal environment, reducing thermal fluctuations crucial for the precise measurements required by nulling interferometers. Both ESA's Darwin Mission and NASA's Terrestrial Planet Finder (TPF) proposed mission concepts considered orbits around L2.

Vibrations from external sources or the spacecraft itself can disturb the alignment of optical surfaces. Mechanical tolerances must account for these potential disturbances, and damping mechanisms might be needed. In addition, optical coatings and materials used in the design must remain stable over time and under potential radiation exposure to maintain the nulling interferometer's performance.

The tolerancing process involves several steps: defining requirements, error budgeting, sensitivity analysis, setting tolerances, and verification and testing.

- Defining Requirements: Establish the performance requirements for the nulling interferometer, such as null depth, wavelength range, resolution, and response function.
- Error Budgeting: Allocate allowable errors to different components and factors, such as surface roughness, alignment errors, and thermal effects.
- Sensitivity Analysis: Perform sensitivity analysis to understand how deviations in certain parameters affect overall performance, helping prioritize the most critical tolerances.
- Setting Tolerances: Based on error budgeting and sensitivity analysis, set tolerances for each component and parameter, such as allowable parabolic mirror surface curvature imperfection or the acceptable range of alignment errors.
- Verification and Testing: Validate the tolerances through simulations, testing, or prototypes to ensure the overall system meets its performance requirements despite these deviations.

In summary, tolerancing aims to set acceptable limits for deviations in various parameters to ensure the overall system meets its performance requirements despite these deviations and to predict the performance of the as-built system in operational conditions.

4.2 Extraction of output parameters from CodeV

An operating space nulling interferometer is considered. The wavelength of interest is set to $\lambda = 10\,\mu m$, the central wavelength of the infrared range considered. Numerical convergence has been enforced and is explained in further details in Section 6.3.

In absence of any perturbations, the light wavefronts coming from the collector optics onto the beam combiner are perfectly parallel. The goal of the pre-combination optics is indeed to collimate the beam, regardless of whether the beam is subsequently focused. Figure 4.1 illustrates the wavefront behavior after passing through an unperturbed, perfect optical design, represented by a simple optical surface acting as a blackbox.

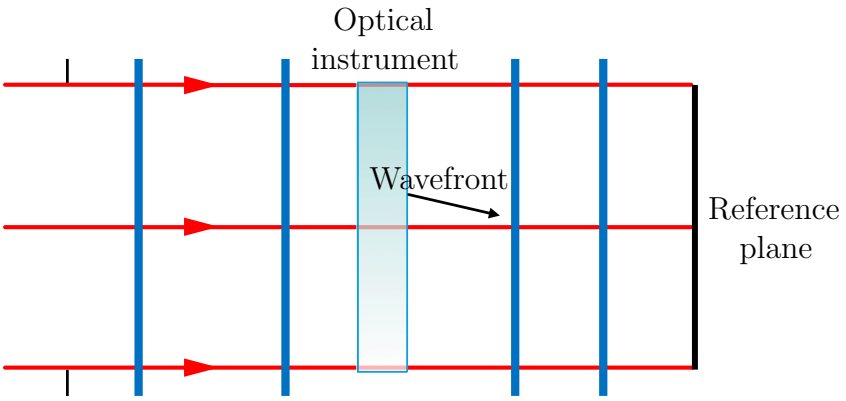

Figure 4.1: Unperturbed optical design wavefronts.

As can be observed, the wavefronts arrive perfectly parallel at the plane of combination. This plane represents the plane at which the state of the light is investigated. Each ray in this beam therefore exhibits the same optical path length. Consequently, when this signal is interfered with an equivalent signal dephased by π, the interference quality is theoretically perfect and the starlight suppression is expected to be total. This scenario describes an ideal nulling interferometer.

However, optical designs are generally subject to imperfections, as depicted in Figure 4.2.

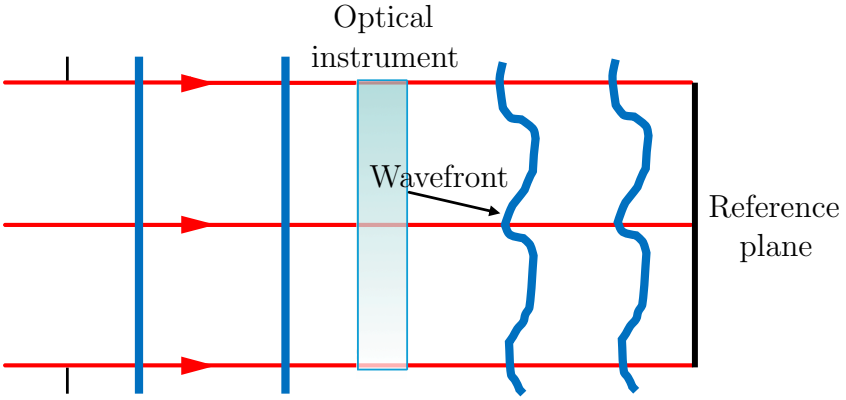

Figure 4.2: Perturbed optical design wavefronts.

Wavefronts are no longer planes at the plane of combination, resulting in a distribution of optical path length and a reduction in interference quality. The nulling interferometer is no longer ideal. These imperfections simulate potential flaws in the optical design, calibration tolerances, or misalignments due to thermal effects.

This chapter aims to develop a tool and establish a methodology for analyzing interference quality under such perturbed conditions. For the sake of example, a simple converging lens is treated as a black box for a nulling interferometer observing on-axis.

4.2.1 Optical Path Distribution

The methodology begins by extracting the optical path of each ray for both perfect and perturbed signals. This is performed using the ray-tracing software CodeV. A macro program has first been developed and implemented in CodeV to retrieve the optical path of selected beams. The results are then visualized using MATLAB, as demonstrated in Figure 4.3.

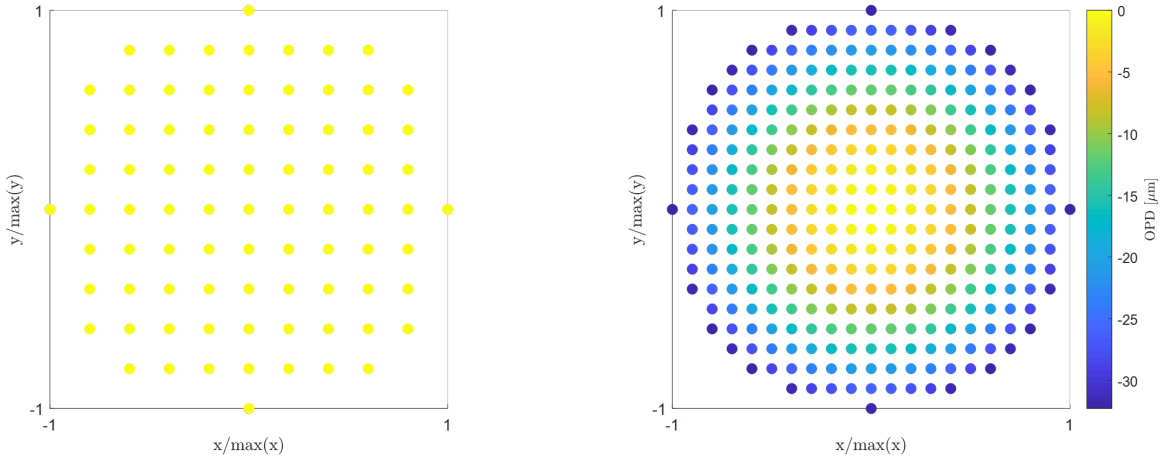

(a) Perfect validation signal

(b) Perturbed validation signal

Figure 4.3: Discrete optical path distribution of the light rays over the detector retrieved from codeV.

The perfect signal exhibits no deviation in optical path, aligning with the expected physics of the case. Conversely, the convergence of the perturbed beam is clearly identified in Figure 4.3b.

An interpolation of these discrete datasets is subsequently conducted to obtain the complete beam wavefront reaching the reference plane for both signals, as depicted in Figure 4.4.

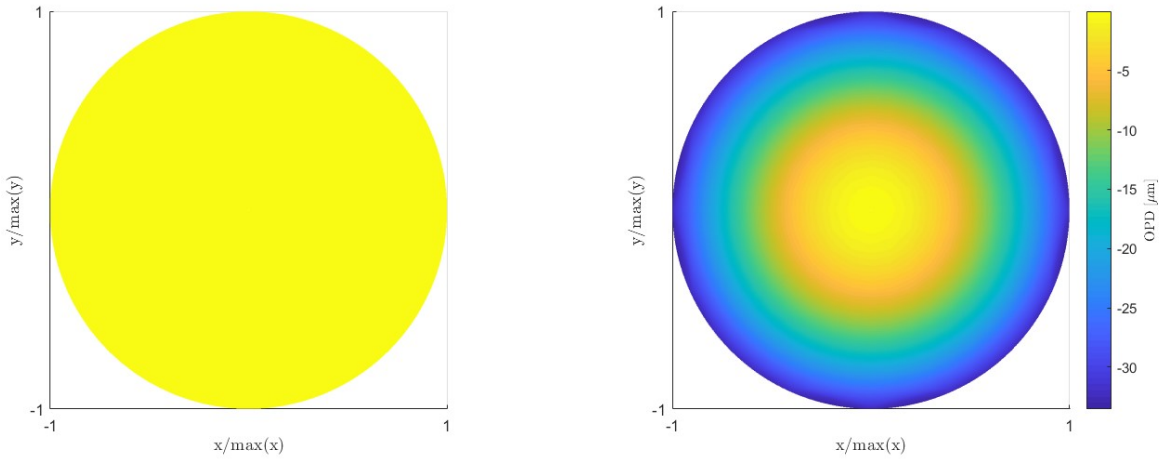

(a) Perfect validation signal

(b) Perturbed validation signal

Figure 4.4: Interpolated optical path distribution of the light rays over the detector.

A 1000×1000 grid is used, see Appendix B, before applying the effect of the circular aperture.

4.2.2 Relative Phase Distribution

Furthermore, the knowledge of the optical path (OP) distribution enables the direct computation of the phase (ϕ) for each rays using the relationship hereafter:

$$\phi = 2\pi \frac{OP}{\lambda} \ , \tag{4.2}$$

where λ represents the working wavelength. The phase is subsequently wrapped within the range $[-\pi\text{-}\pi]$.

The inferred phase distribution corresponding to this computation is depicted in Figure 4.5.

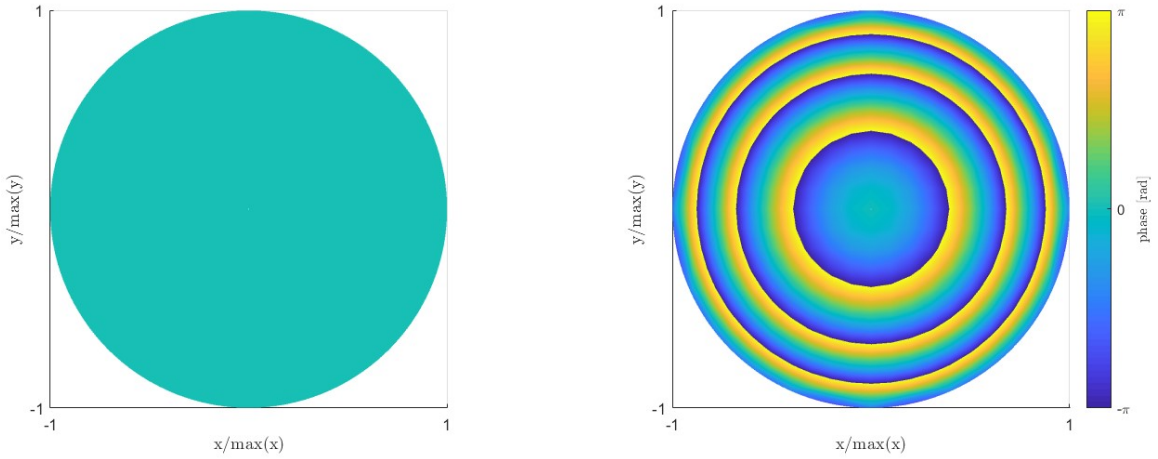

(a) Perfect validation signal

(b) Perturbed validation signal

Figure 4.5: Phase distribution of the light rays over the detector.

The periodic nature of the phase can be observed in Figure 4.5b, aligning consistently with the corresponding purely radial optical path distribution.

4.2.3 Interference Intensity

Assuming a constant amplitude A_0 for both initial signals, and setting it to 1 without loss of generality, the interference of the two signals can be performed. The first signal (*i.e.* the perfect one) is shifted by π before further computations. The coherent sum of both signals can then be applied in the case of nulling interferometry using the following equations:

$$A = \sqrt{2 \cdot (1 + \cos(\phi_1 - \phi_2))} \ , \tag{4.3}$$

and

$$\phi = \tan^{-1}\left(\frac{\sin(\phi_1) + \sin(\phi_2)}{\cos(\phi_1) + \cos(\phi_2)}\right) \ , \tag{4.4}$$

where A and ϕ represent the amplitude and phase of the resulting interference signal, respectively.

To facilitate discussion in terms of intensity $I = A^2/2$, half of the modulus square of the signal is computed, resulting in the intensity distribution of the interfered signal as illustrated in Figure 4.6.

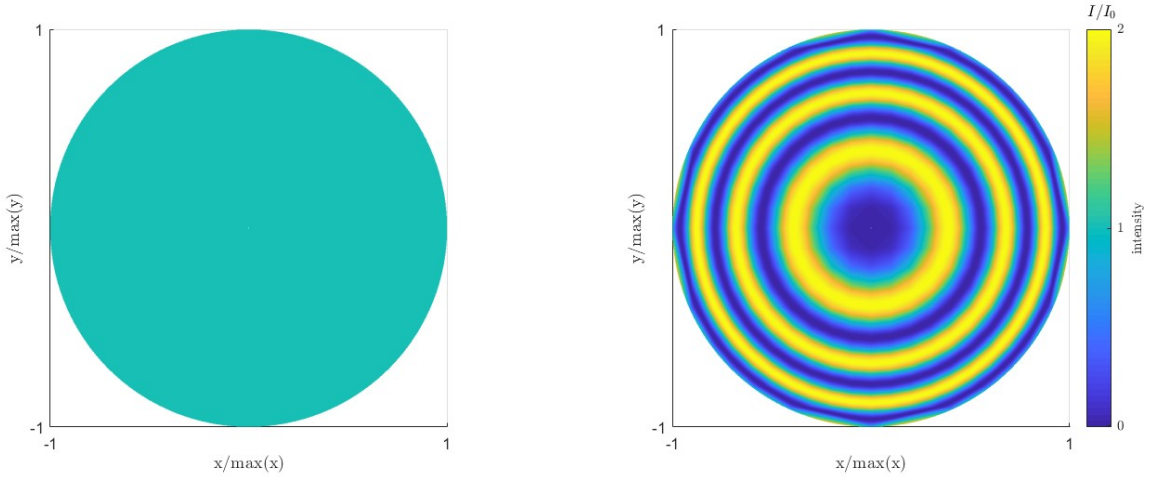

(a) Perfect interfered signal

(b) Perturbed interfered signal

Figure 4.6: Intensity distribution of the interfered signal over the detector.

In Figure 4.6b, values of 2 correspond to constructive interference whereas values of 0 indicate destructive interference. For instance, if this optical design were to be implemented in an actual nulling interferometer, the quality of the interference would be suboptimal. To provide a benchmark for comparison, the intensity distribution of a perfectly nulling instrument is depicted in Figure 4.6a.

It is important to note that this methodology describes the behavior of a light beam before any focusing. Imperfections in this pre-focus stage would propagate to further imperfections after focusing and subsequent beam combination. To construct the interferogram, as discussed in chapter 1, both signals would generally need to be focused, and successive fields should be covered. The analysis presented until here is valid either for on- or off-axis observations.

4.3 Derivation of the response function

4.3.1 Choice of the figure of merit

To evaluate the interference quality, a spatial average of each ray of light is computed to obtain a unique value of average amplitude $\overline{A}$, or similarly for the intensity. In this case, the normalized average amplitude is given by

$$\frac{\overline{A}}{A_0} = 1.238 >> 0 \ . \tag{4.5}$$

A perfect interfered signal completely cancels out the starlight at a zero angle, $A = 0$, as explained in chapter 1. Therefore, the normalized amplitude value does not directly correspond to the nulling depth, which accounts for stellar leakage and total intensity retrieved from the star, as discussed again in chapter 1. Hence, while the normalized amplitude $\frac{\overline{A}}{A_0}$ does not directly represent the null depth N, it serves as a proxy for interference quality. In this case, since $\dfrac{\overline{A}}{A_0} = 1.238 >> 0$, the nulling capability of this hypothetical design is severely compromised.

A better figure of merit was already introduced in chapter 1 in the sense of the response function R, relating the factor by which the starlight is reduced. As derived in [10], the response function R of the nulling interferometer is computed from the juxtaposition S of the two light signals, one being π-shifted to achieve destructive interferences:

$$S = \frac{1}{\sqrt{2}} \left(e^{iC} + e^{-iC} \cdot e^{i\pi} \right) \ , \tag{4.6}$$

where an equal intensity of the signals is assumed and the quantity C expresses the following:

$$C = \frac{\pi b \theta}{\lambda} \ . \tag{4.7}$$

Subsequently taking the modulus square of S yields the classical response function R of a perfect nulling interferometer (complete demonstration provided in Appendix C),

$$\boxed{R = 2\sin^2(C)} \ . \tag{4.8}$$

This expression is nonetheless only valid for a perfect combination of the signals.

This figure of merit will now be investigated for on-axis observations and later generalized for off-axis observations.

4.3.2 On-axis analytical development

On-axis observation, $\theta = 0°$, is illustrated in Figure 4.7.

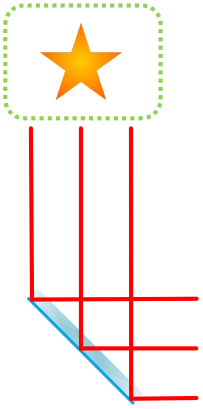

Figure 4.7: On-axis observation of a nulling interferometer.

In order to use R as a figure of merit for on-axis observations, $R(0)$, one must generalize its expression for a random phase perturbation $\Delta\phi$ with respect to the perfect π-shift at an angle $\theta = 0$, or equivalently $C = 0$.

A perturbation term is thus added in the demonstration in [10], resulting in a new expression for S:

$$S = \frac{1}{\sqrt{2}}\left(e^{iC} + e^{-iC} \cdot e^{i(\pi+\Delta\phi)}\right) , \tag{4.9}$$

simplifying for on-axis as

$$S(0) = \frac{1}{\sqrt{2}}\left(1 - (\cos(\Delta\phi) + i \cdot \sin(\Delta\phi))\right) . \tag{4.10}$$

Subsequently taking the modulus square provides the perturbed response function expression for on-axis,

$$R(0) = \frac{1}{2}\left(1 - 2\cos(\Delta\phi) + \cos^2(\Delta\phi) + \sin^2(\Delta\phi)\right) . \tag{4.11}$$

Using the Pythagorean trigonometric identity,

$$R(0) = 1 - \cos(\Delta\phi) , \tag{4.12}$$

and Carnot's formula finally yields the final expression

$$\boxed{R(0) = 2\sin^2\left(\frac{\Delta\phi}{2}\right)} . \tag{4.13}$$

Assuming $\Delta\phi <<$, the small angles approximation, a similar expression than chapter 1 is retrieved:

$$\boxed{R(0) = \frac{\Delta\phi^2}{2}}\,, \tag{4.14}$$

the difference lying in the multiple effects taken into account [34]. This expression describes the so-called non-null floor perturbations, as depicted in Figure 4.8.

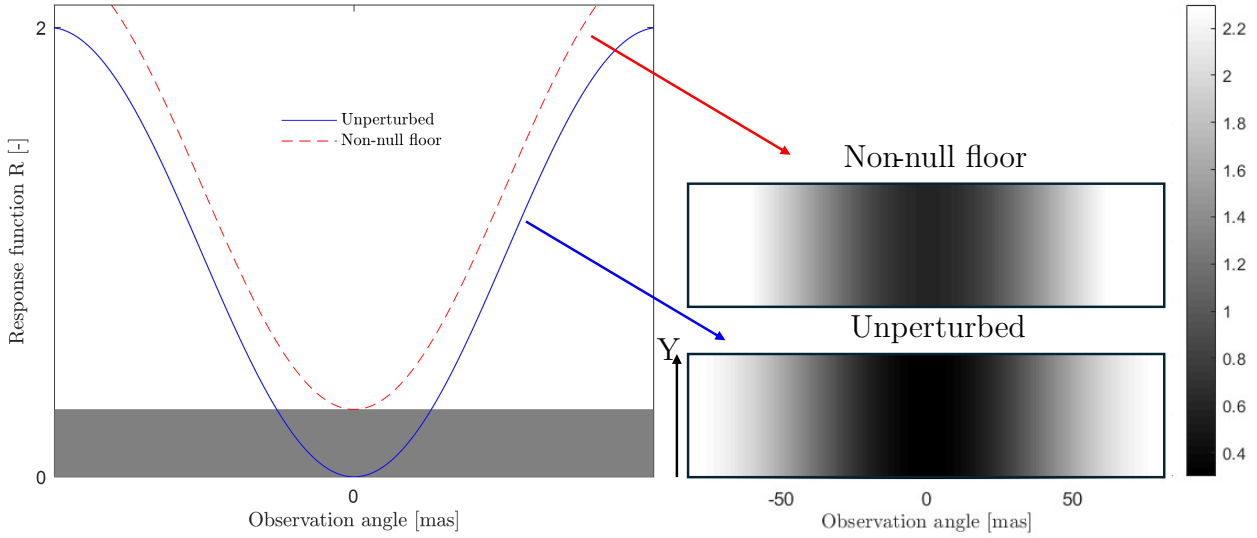

Figure 4.8: Non-null floor perturbations of the response function.

The red curve, however, is only physically valid at a zero angle of observation, as values higher than 2 might be reached. The actual solution for any angles will be derived in the next section.

There are two approaches to compute the response function: deriving it from the phase, as demonstrated above, or directly using the intensity, which is equivalent. This equivalence will be demonstrated for off-axis observations but can also be applied to on-axis observations.

4.3.3 Off-axis analytical development

The methodology is now generalized for off-axis observations, as illustrated in Figure 4.9.

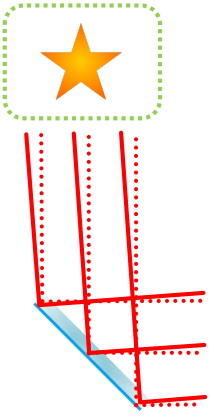

Figure 4.9: Off-axis observation of a nulling interferometer.

However, the figure of merit must be adapted since only $R(0)$ perturbations have been derived so far. The demonstration of the perturbed response function expression from the phase is provided hereunder.

The expressions derived previously are either only valid for a perfect combination of the signals or for on-axis perturbations. In order to use R as a figure of merit for tolerancing means at any angle, one must generalize its expression for a random phase perturbation $\Delta\phi$ with respect to the perfect π-shift for $C \neq 0$.

A perturbation term is thus added once again in the demonstration in [10], resulting in a new expression for S:

$$S = \frac{1}{\sqrt{2}}\left(e^{iC} + e^{-iC} \cdot e^{i(\pi+\Delta\phi)}\right) . \tag{4.15}$$

It is then first assumed that $\Delta\phi <<$, the small angles approximation can thus be applied with

$$e^{i(\pi+\Delta\phi)} = -\left(\cos(\Delta\phi) + i \cdot \sin(\Delta\phi)\right) \approx -1 - i\Delta\phi . \tag{4.16}$$

Replacing in S,

$$S = \frac{1}{\sqrt{2}}\left(e^{iC} + e^{-iC} \cdot (-1 - i\Delta\phi)\right) \tag{4.17}$$

successively gives

$$S = \frac{1}{\sqrt{2}}\left(e^{iC} - e^{-iC} - i\Delta\phi \cdot e^{-iC}\right) , \tag{4.18}$$

$$S = \frac{1}{\sqrt{2}}\left(2i \cdot \sin(C) - i\Delta\phi \cdot \cos(C) - \Delta\phi \cdot \sin(C)\right) , \tag{4.19}$$

by taking advantage of the Euler formulas.

Highlighting the real and imaginary parts,

$$S = \frac{1}{\sqrt{2}} \left(i \cdot (2\sin(C)\Delta\phi - \cos(C)) - \Delta\phi \cdot \sin(C) \right) \tag{4.20}$$

and taking the modulus square yields

$$R = \frac{1}{2} \left((2\sin(C) - \Delta\phi \cdot \cos(C))^2 + (\Delta\phi \cdot \sin(C))^2 \right) \ . \tag{4.21}$$

By decomposing, it gives

$$\frac{1}{2} \left(4\sin^2(C) - 4\sin(C)\cos(C)\Delta\phi + \Delta\phi^2\cos^2(C) + \Delta\phi^2\sin^2(C) \right) \ . \tag{4.22}$$

Using the Pythagorean trigonometric identity $\cos^2(C) + \sin^2(C) = 1$ and the addition formula $2\sin(C)\cos(C) = \sin(2C)$, it becomes

$$R = \frac{1}{2} \left(4\sin^2(C) - 2\sin(2C)\Delta\phi + \Delta\phi^2 \right) \ , \tag{4.23}$$

finally yielding the perturbed expression of the response function

$$\boxed{R = 2\sin^2(C) - \sin(2C)\Delta\phi + \frac{\Delta\phi^2}{2}} \ . \tag{4.24}$$

This equation nonetheless assumes small perturbations and is not valid in all cases.

The generalization for all perturbations of this expression is only possible without assuming the small angles hypothesis. The exact solution for S is thus given by

$$S = \frac{1}{\sqrt{2}} \left(\mathrm{e}^{iC} - \mathrm{e}^{-iC} \cdot \cos(\Delta\phi) - i \cdot \sin(\Delta\phi)\mathrm{e}^{-iC} \right) \ . \tag{4.25}$$

Applying the Euler formulas and developing gives

$$\frac{1}{\sqrt{2}} \left(\cos(C) + i \cdot \sin(C) - \cos(\Delta\phi)\cos(C) + i \cdot \sin(C)\cos(\Delta\phi) - i \cdot \sin(\Delta\phi)\cos(C) - \sin(\Delta\phi)\sin(C) \right) \ . \tag{4.26}$$

The exact expression of the response function is retrieved by taking once again the modulus square of the previous expression:

$$R = \frac{1}{2} \left([\sin(C) + \sin(C)\cos(\Delta\phi) - \sin(\Delta\phi)\cos(C)]^2 + [\cos(C) - \cos(\Delta\phi)\cos(C) - \sin(\Delta\phi)\sin(C)]^2 \right) \ , \tag{4.27}$$

where the imaginary and real parts have first been highlighted.

Developing each bracket square by using the formula $(a+b+c)^2 = (a^2+b^2+c^2+2ab+2bc+2ac)$ yields

$$\begin{aligned} R = \frac{1}{2}\Big(& [2\sin^2(C)\cos(\Delta\phi) - 2\sin(\Delta\phi)\sin(C)\cos(C) - 2\sin(C)\cos(C)\sin(\Delta\phi)\cos(\Delta\phi) \\ & + \sin^2(C) + \sin^2(C)\cos^2(\Delta\phi) + \sin^2(\Delta\phi)\cos^2(C)] \\ & + [\cos^2(C) - 2\cos^2(C)\cos(\Delta\phi) - \sin(\Delta\phi)\sin(2C) + \cos^2(\Delta\phi)\cos^2(C) \\ & + \sin(2C)\sin(\Delta\phi)\cos(\Delta\phi) + \sin^2(\Delta\phi)\sin^2(C)]\Big) \ . \end{aligned} \tag{4.28}$$

After removal of the cancelling terms and application of the trigonometric identity and addition formula, the expression is simplified as

$$\frac{1}{2}\left(2\sin^2(C)\cos(\Delta\phi) - 2\sin(2C)\sin(\Delta\phi) + 2 - 2\cos^2(C)\cos(\Delta\phi)\right) \ . \tag{4.29}$$

Highlighting now the terms in $\cos(\Delta\phi)$,

$$R = \frac{1}{2}\left(2\cos(\Delta\phi)\cdot(\sin^2(C) - \cos^2(C)) - 2\sin(2C)\sin(\Delta\phi) + 2\right) \tag{4.30}$$

and applying once more the trigonometric identity gives

$$R = \frac{1}{2}\left(2\cos(\Delta\phi)\cdot(2\sin^2(C) - 1) - 2\sin(2C)\sin(\Delta\phi) + 2\right) \ . \tag{4.31}$$

By simply developing, it provides

$$R = \frac{1}{2}\left(4\cos(\Delta\phi)\sin^2(C) - 2\cos(\Delta\phi) - 2\sin(2C)\sin(\Delta\phi) + 2\right) \ . \tag{4.32}$$

By taking advantage of Carnot's formula $1-\cos(2a) = 2\sin^2(a)$, it yields

$$R = \frac{1}{2}\left(4\cos(\Delta\phi)\sin^2(C) + 4\sin^2(\frac{\Delta\phi}{2}) - 2\sin(2C)\sin(\Delta\phi)\right) \ , \tag{4.33}$$

finally giving the general expression of the response function for any phase perturbation

$$\boxed{R = 2\sin^2(C)\cos(\Delta\phi) + 2\sin^2(\frac{\Delta\phi}{2}) - \sin(2C)\sin(\Delta\phi)} \ . \tag{4.34}$$

Specific cases of this expression come back to the other previously defined identities.

In the particular case of $\Delta\phi = 0$, the expression of the perfect response function is retrieved [10] whereas applying the small angles approximations yields the approximated formula.

This mathematical expression of the response function is bounded between 0 and 2, complying with its physical interpretations of constructive and destructive interferences limits.

Trivially, the maximum perturbation possible $\Delta\phi = \pi$ simply comes back to strict interferometry without π-phase shift. Hence, constructive interference occurs at a zero angle of observation and the fringe pattern becomes inverted.

The representation of the perturbed response function is illustrated in Figure 4.10 for any angles.

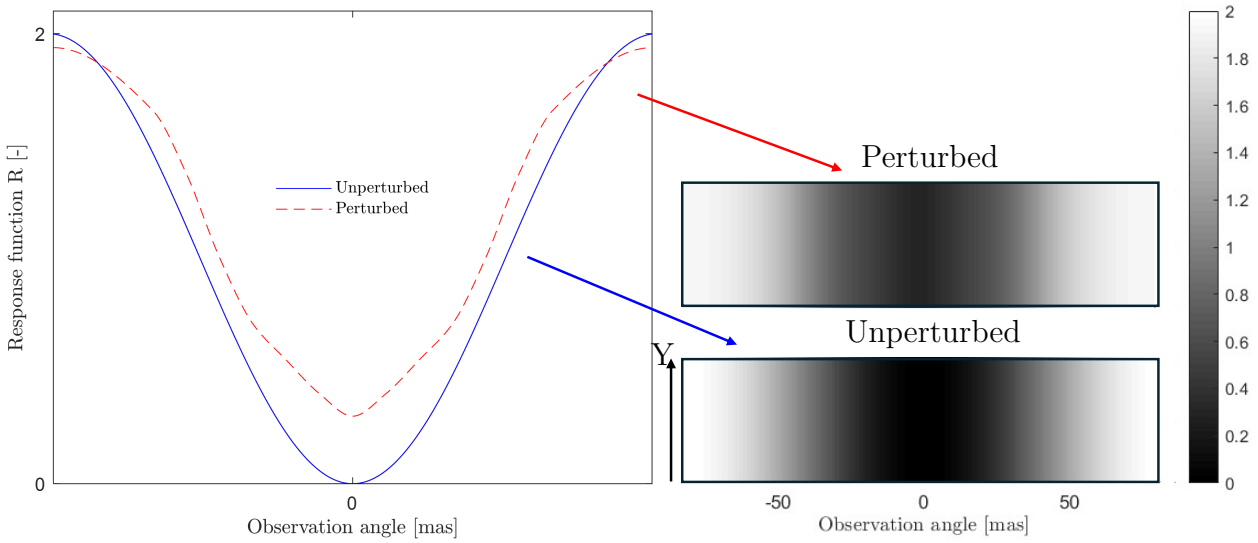

Figure 4.10: Perturbed response function.

Such a curve can be obtained by conducting MonteCarlo simulations on a toleranced system, extracting the $\Delta\phi$ in each case and computing the statistical value at 1 sigma. Applications of these simulations are provided in chapter 5.

Alternative approach

The knowledge of the phase, easily obtainable, to compute the response function is pleasant and straightforward. However, it is not always applicable. For instance, with designs undergoing straylight, the phase becomes incoherent so that this approach is proscribed. Another strategy as briefly mentioned for on-axis is to directly use the interferogram or intensity of the interference. The equivalence between the general perturbed response function and the intensity is demonstrated hereunder. One approach will be preferred to the other depending on conditions and physical context.

First of all, the geometry of the problem is recalled in Figure 4.11.

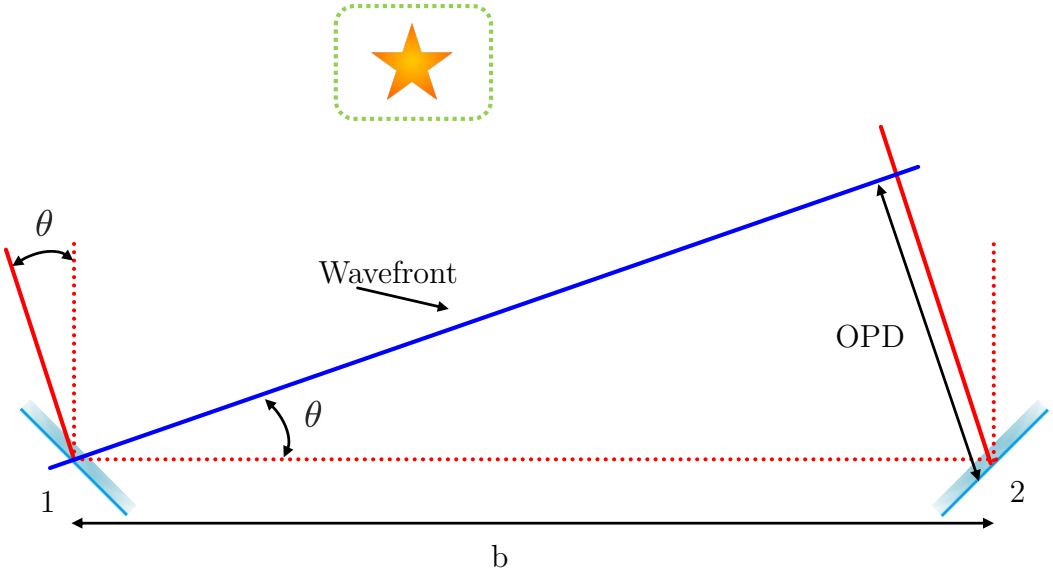

Figure 4.11: Off-axis observations geometric schematic.

The optical path difference *OPD* between the two collectors is easily computed from Figure 4.11 as

$$OPD = OP_2 - OP_1 = b\theta \ , \tag{4.35}$$

with OP_i the optical path of the beam of collector i.

By definitions of the variables used previously, the following relationships are inferred:

$$C = \frac{\pi b\theta}{\lambda} = \frac{(OP_2 - OP_1)\pi}{\lambda} \ , \tag{4.36}$$

$$\phi_i = \frac{2\pi OP_i}{\lambda} \ , \tag{4.37}$$

so that eventually

$$C = \frac{\phi_2 - \phi_1}{2} \ . \tag{4.38}$$

Starting out from the definition of the interference intensity and replacing yields

$$I = 1 + \cos(\phi_1 + \pi - \phi_2) = 1 + \cos(-2C + \pi) \ . \tag{4.39}$$

Using the trigonometric relationships $\cos(-a) = \cos(a)$ and $\cos(a+\pi) = -\cos(a)$ gives

$$I = 1 - \cos(2C) \ . \tag{4.40}$$

Finally, Carnot's formula directly proves that the response function equals the intensity, at least without any perturbations:

$$\boxed{I = R = 2\sin^2(C)} \ . \tag{4.41}$$

Adding a perturbation term $\Delta\phi$ as previously in the definition of the intensity will now prove that this equality stands for any angles and with or without perturbations.

Starting again from the definition, it gives

$$I = 1 + \cos(-2C + \pi + \Delta\phi) = 1 - \cos(-2C + \Delta\phi) \ . \tag{4.42}$$

Using now the trigonometric addition formula $\cos(a-b) = \cos(a)\cos(b) + \sin(a)\sin(b)$ yields

$$I = 1 - (\cos(2C)\cos(\Delta\phi) + \sin(2C)\sin(\Delta\phi)) \ , \tag{4.43}$$

and, after further simplifications and rearrangement,

$$I = 1 - (1 - 2\sin^2(C))\cos(\Delta\phi) - \sin(2C)\sin(\Delta\phi)) \ . \tag{4.44}$$

After decomposition,

$$I = 1 - \cos(\Delta\phi) + 2\sin^2(C)\cos(\Delta\phi) - \sin(2C)\sin(\Delta\phi) \ , \tag{4.45}$$

it finally gives the expression of the perturbed response function, concluding this demonstration:

$$\boxed{I = R = 2\sin^2(C)\cos(\Delta\phi) - \sin(2C)\sin(\Delta\phi) + \sin^2(\frac{\Delta\phi}{2})} \ . \tag{4.46}$$

Two approaches can therefore be envisaged: deriving the response function from the easily obtainable phase distribution or using the intensity when not applicable.

4.4 Tolerance analysis interpretations

Two common strategies exist for conducting a tolerance analysis, namely using statistics with Monte Carlo simulations or fixing parameters and performing sensitivity analysis. The two approaches are detailed and interpreted hereafter.

MonteCarlo simulations

A perturbation is first applied to the optical system. The associated figure of merit, the response function, is then evaluated for each angle of observations from the dark to the bright fringe. This results in a perturbed response function curve for the considered perturbed configuration. This stage is repeated a great number of times for different random perturbations to later perform statistics. This is by definition MonteCarlo simulations. At the end, the values of $\boldsymbol{R}$ is known for a great number of perturbed systems at each angle considered. Statistics can therefore be conducted, and two important scenarios are considered:

- The starlight extinction for the worst-case scenario. For the sake of the example, this will be evaluated for a 1 sigma percentile. However, a more restrictive approach can be followed with, for instance, a 2 sigma percentile but this requires to perform an even larger of simulation to ensure appropriate "statistics". The starlight extinction is thus taken at the extent of the star, where the stellar leakage is at its maximum. This value is desired to be as low as possible for a nulling interferometer.
- The planet transmission for the worst-case scenario (considering again a 1 sigma percentile). This value is computed at the location of the bright fringe. Conversely, this value is desired to be as high as possible for a nulling interferometer.

Before further discussion, the probability density function (PDF) and associated cumulative distribution function (CDF) of a distribution (in this example a Gaussian) are illustrated in Figure 4.12 for the sake of comprehension.

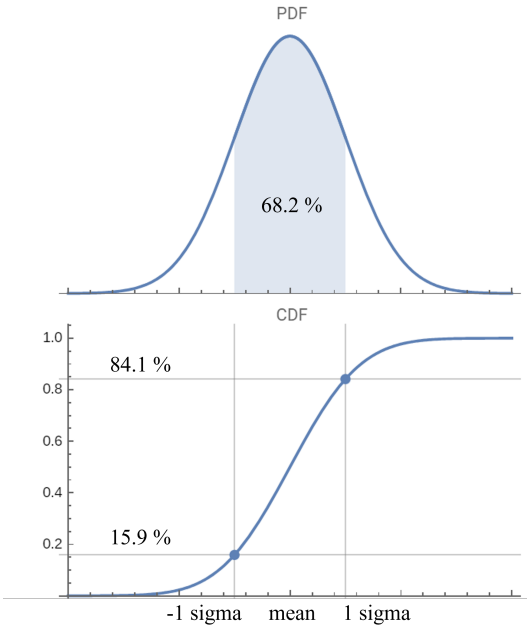

Figure 4.12: PDF and associated CDF of a normal distribution.

The PDF of a distribution describes the likelihood of a random variable (X) taking on a specific value. On the other hand, the CDF of a distribution represents the probability that a random variable (X) is less than or equal to a specific value (x). It is therefore the integral of the PDF from $-\infty$ to the specific value (x). The 1 sigma and -1 sigma percentiles correspond respectively to the 84.13th and 15.87th percentiles. Thus, approximately 68.24% of the values lie within those limits. Moreover, for the specific case of a normal distribution, the 1 sigma value corresponds to the standard deviation of the distribution.

Returning to the star and planet signals, a subtlety nevertheless arises in the sense that a 1 sigma percentile approach for the star corresponds to a -1 sigma percentile for the planet, due to the switch between dark and bright fringes.

The reference curve for the star extinction will be located below, so that the 1 sigma percentile curve corresponds to the worst case scenario under which 84.1 % of the perturbed configurations have a lower stellar leakage (or lower response function). On the other hand, the reference curve for the planetary transmission will be located above, so that the 1 sigma percentile curve corresponds this time to the worst-case scenario above which 15.9 % of the perturbed configurations have a better transmission (or higher response function). In other words, the equivalent curve would be the -1 sigma percentile curve. This is due to the change of reference and would not happen if the mean curve was considered.

A value of contrast v can be computed between the maximum response function of the planet R_p and the value of the response of the star at the angle of extent of the stellar leakage R_* as

$$v = \frac{R_p - R_*}{R_p + R_*} \ . \tag{4.47}$$

This definition of the contrast v is similar to that of visibility V except that the response at the extent of the star is investigated instead of the minimum at a zero angle. Figure 4.13 further illustrates this contrast in the case of a perturbed design with respect to the unperturbed one for the star of reference.

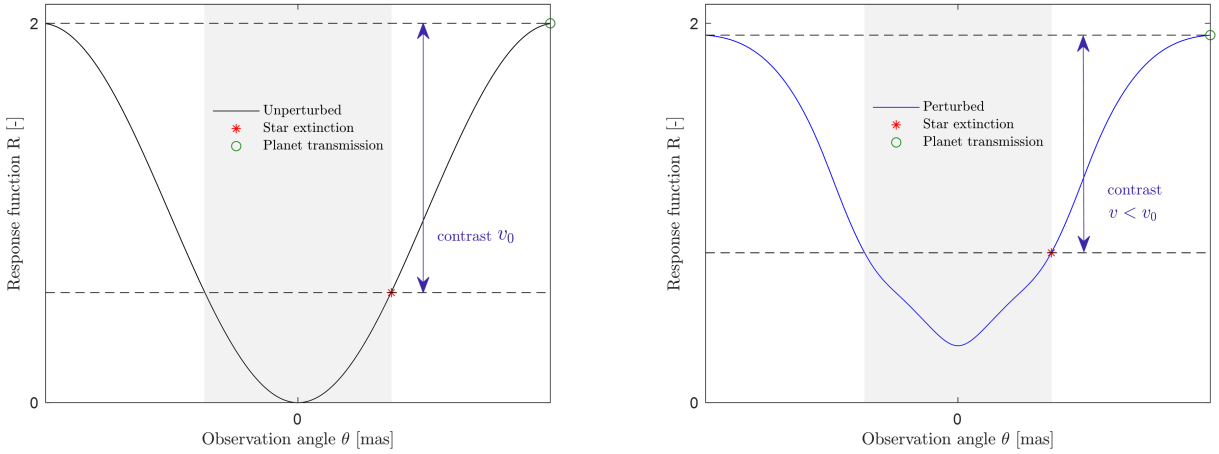

(a) Unperturbed case

(b) Perturbed case

Figure 4.13: Contrast between star extinction and planet transmission.

As can be seen for the unperturbed design, the planet transmission has a natural value of 2 and stellar leakage occurs, leading to a finite value of contrast. If the design is perturbed, the planet

transmission is lower and the stellar leakage is higher, or, equivalently, the stellar extinction is lower. This results in a degraded contrast. This contrast was particularized in the case of a single perturbed design, but, as discussed previously, statistics can be conducted on a high numbers of cases. However, as aforementioned, the worst case scenario for stellar leakage at 1 sigma must be associated to the worst case scenario for planet transmission at -1 sigma.

Sensitivity analysis

The other approach consists of evaluating the sensitivity of the system by conducting simulations over different values of the perturbations for a fixed parameter. For instance, degrading the curve radius of a mirror and assessing the value of the response function, all other things remaining unchanged. This allows targeting one specific constaints and prioritizing specific tolerances.

4.5 Conclusions

An **advanced analysis tool** has been developed to **assess interference quality**, leveraging the results from CodeV ray-tracing software and MATLAB postprocessing capabilities. Utilizing the **response function as a figure of merit**, it establishes a robust foundation for subsequent investigations into optical designs such as SCoHo and DiCoS. The tool offers two computation strategies based on the coherence of the phase or the direct use of the interferogram. Additionally, a rigorous convergence study is conducted in the appendices to ensure the validity of the results. The capabilities of this tool will be demonstrated in the following chapters through tolerancing analysis and the study of various perturbations such as tip/tilt and mirror imperfections. Monte Carlo simulations will be explored in chapter 5 to assess the influence of manufacturing tolerances and positioning errors, while sensitivity analysis will be performed in chapter 6.

Chapter 5

Tolerance modeling results

Contents

5.1 Tolerancing hypothesis 69
5.2 Nominal performance 70
5.3 Results 71
5.3.1 Case study 1 71
5.3.2 Case study 2 75
5.3.3 Case study 3 77
5.4 Conclusions 78

This chapter aims to utilize the modeling tool developed previously to conduct **Monte Carlo tolerancing analysis** on the **SCoHo configuration**. The objective is not to derive precise specifications for design tolerances at the conclusion of the process. Instead, the focus is on exploring typical tolerance values to demonstrate the robustness and utility of the tool. The parameters for the simulations are initially presented and justified before presenting the results for both nominal performance and perturbed cases.

5.1 Tolerancing hypothesis

This chapter is dedicated to the budget error approach. On the other hand, sensitivity analysis are conducted in the following chapter. For this matter, MonteCarlo simulations are conducted for mirror wavefront errors and optical surfaces positioning errors. A nominal configuration is thus taken as standard and departures from this configuration are simulated by random deviations. A standard deviation error e is chosen, so that by denoting x the nominal configuration, gaussian random departures occurs around x. The figure of merit considered to assess the nulling interferometer performance is the response function R, as explained previously.

The typical mirror wavefront error standard deviation considered are $\lambda/10$ for plane mirrors and $\lambda/20$ for powered ones, with the exception of the tip/tilt mirror, which is set at $\lambda/100$. This finer tolerance for the tip/tilt mirror is justified by its critical sensitivity in ensuring coherence maintenance. Alignment errors of 0 (no misalignment), 1, and 10 microns are discussed, corresponding to X, Y, and Z departures of the optical surfaces from their initial spatial positions. The extreme value of 10 microns, equivalent to the wavelength, represents a scenario of a completely ill-designed nulling interferometer. The cases are presented in order of magnitude of the perturbations.

5.2 Nominal performance

The tool is validated by demonstrating the behavior of the response function under nominal performance conditions. By retrieving data from CodeV with the perfect optical design of SCoHo, Figure 5.1 shows the adequacy between the measured optical path and the theoretical perfect response function, confirming the physical interpretations of this methodology. The associated main fringes interferogram is also depicted.

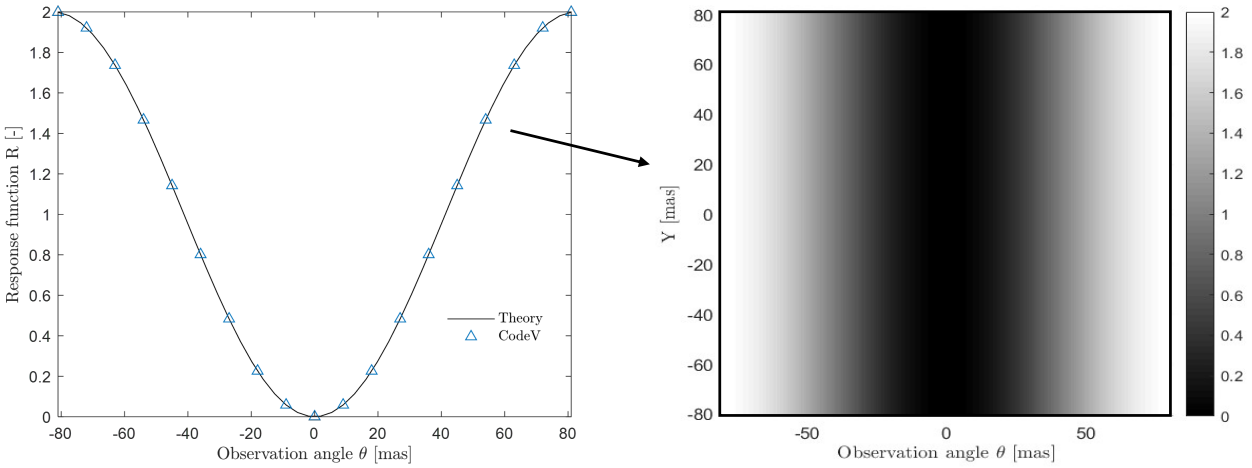

Figure 5.1: Response function of a perfect nulling interferometer of baseline 12.5 m and associated main fringes interferogram.

5.3 Results

5.3.1 Case study 1

The proposed tolerancing method is now examined by considering the wavefront errors discussed previously (in particular $\lambda/100$ for the tip/tilt mirror), while maintaining perfect alignment of all optical surfaces. This case allows to explore an example of manufacturing tolerances of mirrors and will serve as a baseline for discussing alignment errors.

Figure 5.2 illustrates the deviations of the perturbed simulations from the unperturbed perfect response function curve. The curve representing one positive standard deviation from the mean is also presented. The simulations are performed for a specific set of angles, covering the central region of the interferogram, which explains the vertical alignment of the simulated points.

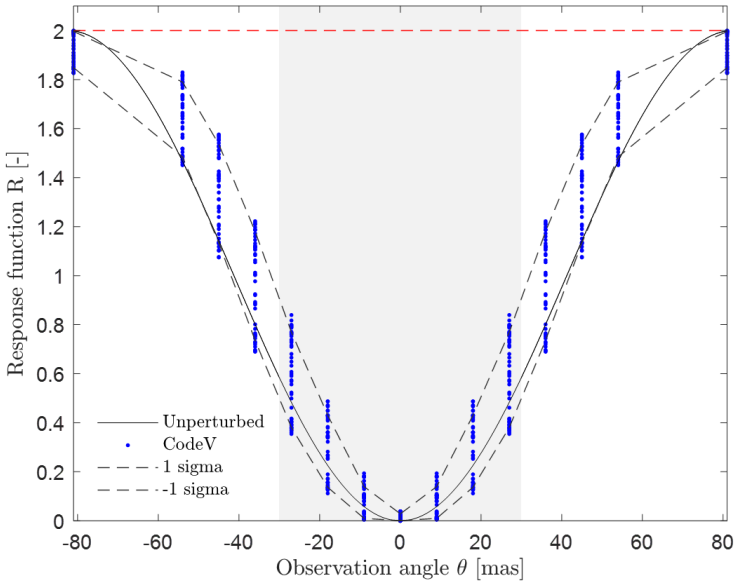

Figure 5.2: Perturbed response function curve from MonteCarlo simulations with respect to the unperturbed theory (wavefront error $\lambda/100$, no misalignment).

The primary effect of the perturbed configuration is the emergence of non-null floor perturbations. Even for on-axis observations, starlight cancellation is no longer total, resulting in a non-zero value for $R(0) = 0.029$. Additionally, an increase in stellar leakage, indicated by the shaded area, is evident in Figure 5.2. Previously, the starlight dropped on the detector, causing the response function to reach as high as $R = 0.584$ at the beginning of the star's corona. This value further increases for the perturbed 1 sigma curve, reaching $R = 0.906$. The hypothetical star considered remains Proxima Centauri, as discussed in chapter 1. The contrast ν can be computed as $\nu = 0.342$, which can be compared to the unperturbed case contrast $\nu_0 = 0.548$. By definition, as discussed previously, it is computed between the star response function at the extent angle of stellar leakage and the planet maximum response function angle. This further demonstrates the degradation of the interference quality.

Another perspective on the effect of the perturbed simulations is shown in Figure 5.3, which depicts the normalized perturbed response function.

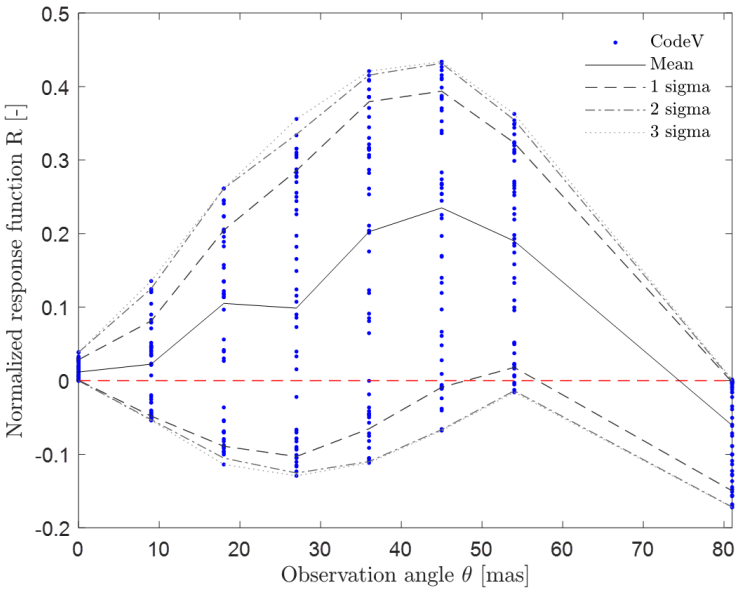

Figure 5.3: Normalized perturbed response function from MonteCarlo simulations and associated deviation envelope (wavefront error $\lambda/100$, no misalignment).

The perfect response function has been substracted from the perturbations to assess their direct effect relative to the nominal value (the line $x = 0$). Negative values, therefore, illustrate points below the theoretical curve. At low angles, this would result in enhanced performance and a better extinction ratio than the classical θ^2 behavior. Conversely, at angles corresponding to the neighborhood of a maximum of the sine square theoretical curve, where constructive interference normally occurs, the interferences would no longer be fully constructive, resulting in a loss of contrast.

As observed in Figure 5.3, the upper envelope increases with the observation angle up to a certain point, after which the trend reverses. Moreover, the mean line starts to decrease at greater angles. The inflection point of the envelope can be understood by considering the bounds of the response function $[0;2]$. As the angle increases, the response function approaches the value of 2. Therefore, the perturbations begin to deteriorate the constructive interferences instead of the destructive ones, resulting in a decrease in the upper envelope. On the other hand, the bounds of 0 and 2 also explain the behavior of the mean line. For a zero angle of observation, or equivalently at the minimum of the sine square function, the response function can only be greater than 0, whereas at its maximum, it can only be lower than 2. These constraints force the distributions of the perturbations to be positive at a zero angle and negative at the maximum angle. Hence, the mean line starts positive and ends negative in this normalized graph.

This shift explains the distribution of points from positive to negative values for the angles corresponding to the minimum (0 mas) and the maximum (approximately 81 mas) of the theoretical curve, as illustrated in Figure 5.4.

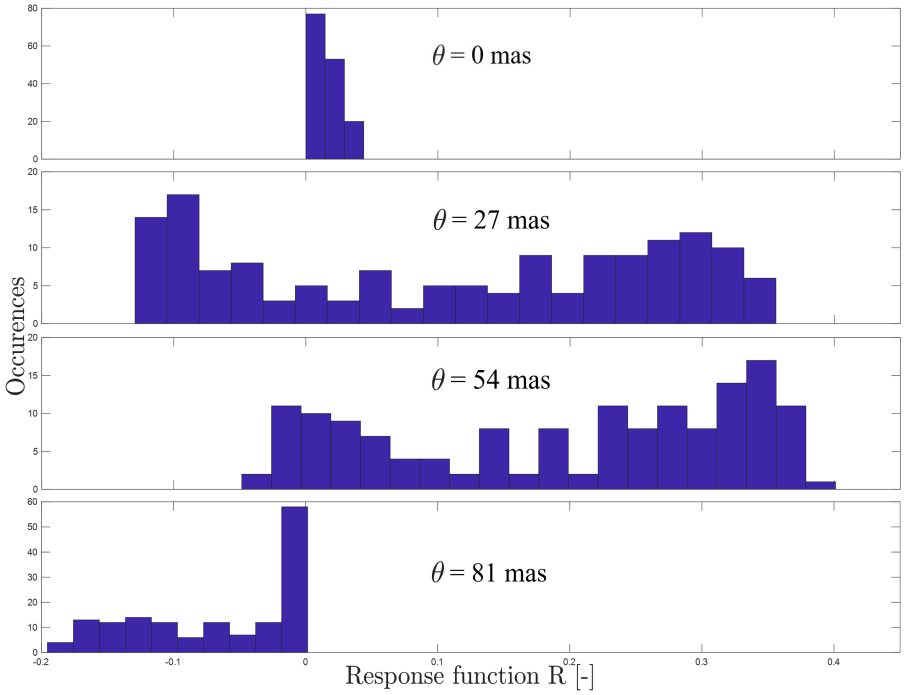

Figure 5.4: Distributions of the response function for angles of respectively 0, 27, 54 and 81 mas (wavefront error $\lambda/100$, no misalignment).

The histogram graphs represent the normalized distributions where the unperturbed value has been subtracted. It shows that the distribution is less spread at the minimum than at the maximum. However, at the maximum, there are more occurrences of nearly unperturbed values. Histograms at intermediate angles are also presented in Figure 5.4 to illustrate the evolution of these distributions.

Two bulges of point concentration can be observed. With increasing angles, the left bulge, initially higher than the right, starts to decrease in amplitude in favor of the right. The extreme cases are thus illustrated for angles of 0 and 81 mas.

Independently of the observation angle, the distribution appears to be a combination of two bulges. At low angles, only one predominant bulge can be observed, with the distribution contained positively near the 0 value of the response function. The symmetric case occurs at high angles corresponding to the maximum of the unperturbed response function, with a negative containment near the 0 value. Between these angles, the distribution is seen to be a combination of both bulges, with the concentration of points shifting slightly from left to right as θ increases. This shift was already reflected in the behavior of the mean value line in Figure 5.3.

Finally, the difference between the various expressions of the response function derived are investigated in Figure 5.5. The unperturbed curve, describing a sine square, represents the ideal case. When considering non-null floor perturbations, starlight is not completely cancelled out at a zero angle of observation. For this configuration, the effect appears relatively small, with $R(0) = 0.029$ as discussed previously. However, the extremely high precision required for nulling interferometry, especially for ensuring coherence, must not be disregarded. Morever, it can be seen that the non-null floor curve greatly underestimates the actual response function. The general solution illustrates this actual and global effect of the perturbations for any angle of observation. This solution is physically compliant since it is bounded between 0 and 2, similar to the unperturbed solution. Finally, the approximation of the general solution, which is mathematically simpler, offers a good alternative for small angles as long as the phase perturbation remains small. This approximation, nevertheless, is not necessarily bounded between 0 and 2 and requires careful interpretation.

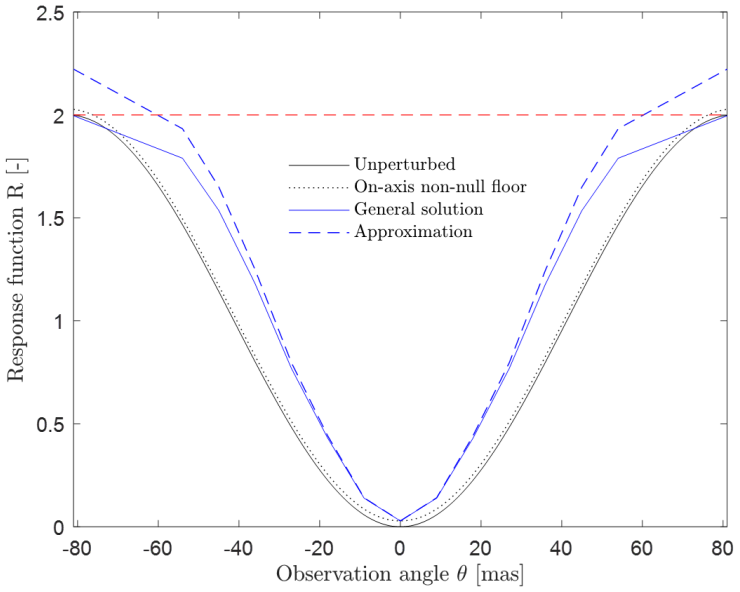

Figure 5.5: Evolution of the different response function definitions (wavefront error $\lambda/100$, no misalignment).

5.3.2 Case study 2

In this case, misalignment of up to 1 micron is introduced for all optical surfaces.

Figure 5.6 illustrates the resulting deviations of the perturbed simulations from the unperturbed perfect response function curve. In addition, the curve corresponding to one positive standard deviation from the mean is presented.

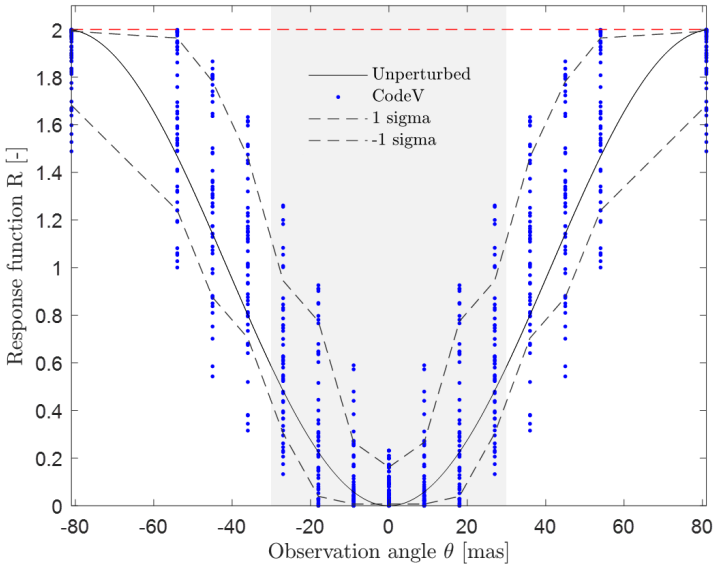

Figure 5.6: Perturbed response function curve from MonteCarlo simulations with respect to the unperturbed theory (wavefront error $\lambda/100$, misalignment 1 micron).

As observed in Figure 5.6, misalignments significantly degrade the capabilities of the nulling interferometer, with $R(0) = 0.162$ and a stellar leakage $R = 1.118$ at the extent of the star. While no perturbed simulation achieves a perfect null for on-axis observation, some simulations do improve the response function at certain angles. However, such perturbed configurations may worsen the interferometer's capability at other angles, indicating that the configuration is not necessarily optimized. This underscores the importance of tolerancing. Moreover, the large extent of the distribution is expected due to a value of 1 micron, or equivalently $\lambda/10$, which is more than twice the coherence length. The contrast V can be computed as $v = 0.201$, an even lower value than the previous case.

The instability of these simulations is further evident in Figure 5.7.

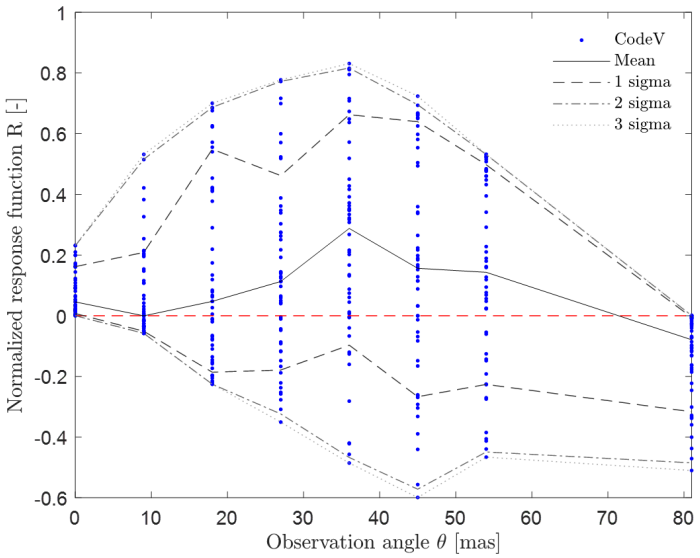

Figure 5.7: Normalized perturbed response function curve from MonteCarlo simulations and associated deviation envelope (wavefront error $\lambda/100$, misalignment 1 micron).

Negative values indeed occur at times, indicating enhanced precision, but values as high as 0.8 above the unperturbed curve can also be observed. Nevertheless, the classical behavior of the upper envelope and mean value line remains consistent. Finally, the evolution of the response function expressions is depicted in Figure 5.8.

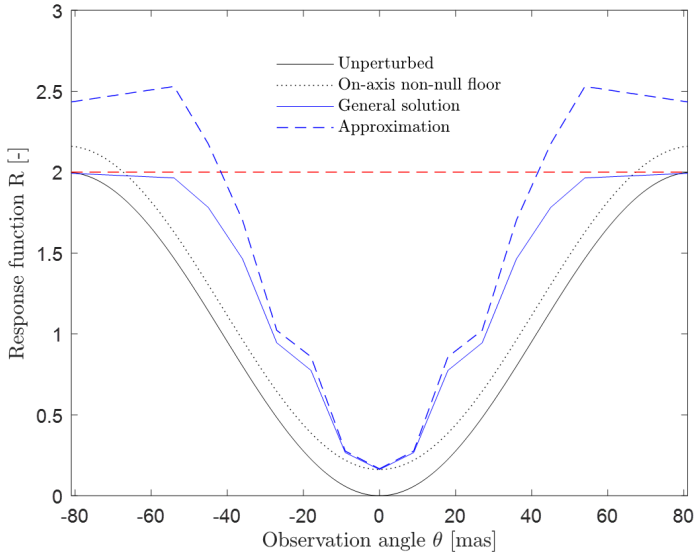

Figure 5.8: Evolution of the different response function definitions (wavefront error $\lambda/100$, misalignment 1 micron).

The non-null floor perturbation is quite significant, with $R(0) = 0.162$, as mentioned. The general solution demonstrates a clear degradation in performance but remains physically compliant, never exceeding a value of 2. On the other hand, the approximation function proves to be less accurate,

especially away from the on-axis observation, and tends to deviate from the general solution. In addition, it reaches values higher than 2, which is not physically plausible. The rough, broken appearance of the curves is due to the high amplitude of the perturbations. This highlights the importance of the tolerancing modeling tool in establishing acceptable limits for deviations in optical surface alignments, ensuring that the overall system meets its performance requirements.

5.3.3 Case study 3

This final brief case study involves extreme perturbations with misalignments of up to 10 microns. This worst case in terms of perturbations, with respect to cases 1 and 2, is examined to explore the chaotic performance of such a nulling interferometer. The deviations of the perturbed simulations from the unperturbed perfect response function curve are depicted in Figure 5.9, with the 1 sigma curve also included for reference.

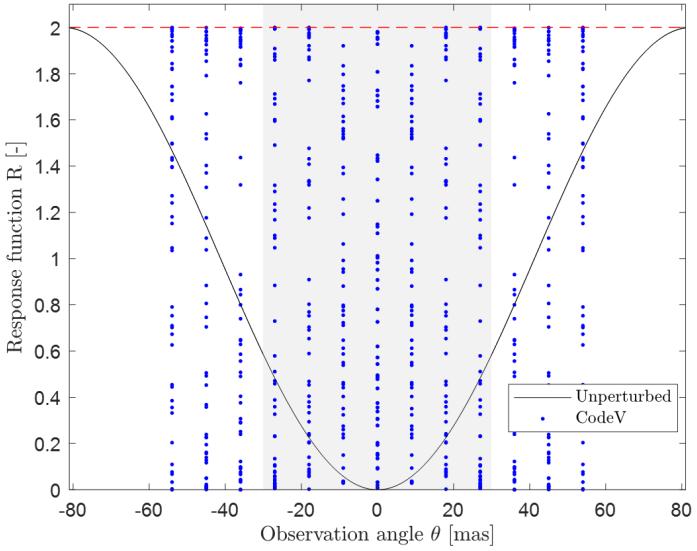

Figure 5.9: Perturbed response function curve from MonteCarlo simulations with respect to the unperturbed theory (wavefront error $\lambda/100$, misalignment 10 microns).

As anticipated, misalignments of up to the working wavelength value lead to complete chaos. A misalignment of this magnitude could indeed convert destructive interference to constructive. While not realistic, this demonstrates the tool's robustness. Even with such an ill-defined problem, the computed response function does not exceed a value of 2, and the tool continues to operate effectively. This case clearly illustrates a suboptimally designed interferometer that requires redesign. The concept of contrast is irrelevant in this case with the absence of real interpretations of eventual conducted statistics. The contrast could be seen as $v = 0$. Table 5.1 summarizes the steady degradation of the contrast from the unperturbed case to the final case 3.

Table 5.1: Summary of the contrast of the various cases.

	Unperturbed	**Case 1**	**Case 2**	**Case 3**
v	0.548	0.342	0.201	0

5.4 Conclusions

The general **interference modeling tool** developed has proven to be invaluable for **tolerancing analysis**. Its capabilities were demonstrated in a specific case of $\lambda/100$ wavefront error, highlighting its importance for **manufacturing tolerancing**. Subsequently, it was employed for different optical surface **alignment tolerancing**.

This tool can be utilized for comprehensive tolerancing analysis to optimize configurations such as SCoHo or DiCoS, providing error budgets and tolerance sets.

In the next chapter, specific parameter variations and subsequent sensitivity analysis will be conducted, serving as a second method to demonstrate the capabilities of this tool.

Chapter 6

Parameters sensitivity analysis

Contents

6.1 Tip/tilt angles 79
6.1.1 Applied case 79
6.1.2 Sensitivity analysis 81
6.1.3 Tip/tilt correlation 82
6.2 Mirror curve imperfections 87
6.2.1 Applied case 87
6.2.2 Sensitivity analysis 88
6.3 Conclusions 90

In this chapter, the previously developed **analysing tool** is used to investigate two basic type of perturbations: tip/tilt and mirror curve imperfection. This second application will further demonstrate its capabilities. The methodology is exemplified in a single applied case and a global **sensitivity analysis** is subsequently conducted. Conclusions are eventually drawn on the necessity of implementing correction mechanisms.

6.1 Tip/tilt angles

6.1.1 Applied case

Tip/tilt perturbations are considered for the **SCoHo design**. The methodology is detailed for a 0.1 degree tilt of the lightbeam at the plane of reference.

The optical path distribution and corresponding phase distribution are illustrated in Figure 6.1.

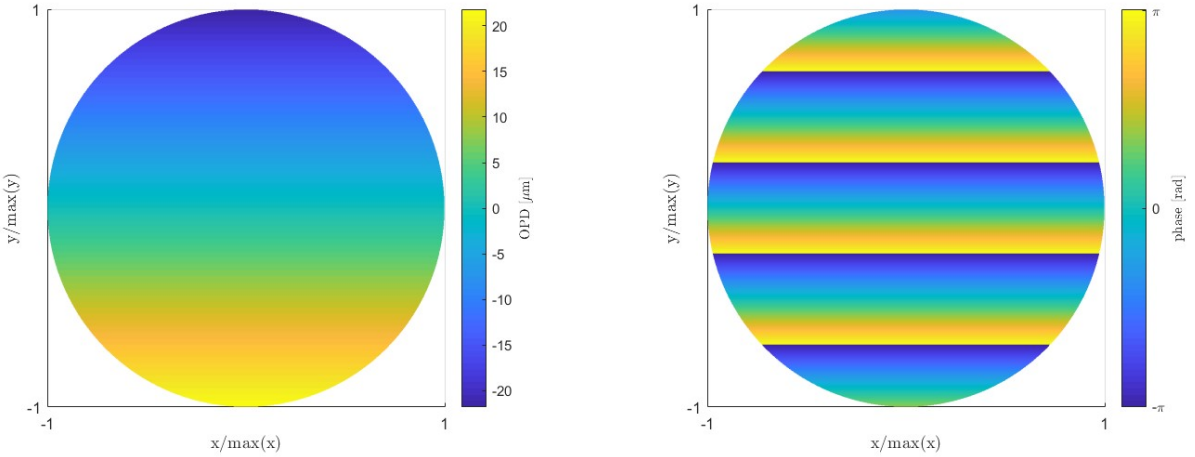

(a) Optical path distribution

(b) Relative phase distribution

Figure 6.1: Optical path and corresponding phase distributions of SCoHo configuration with a 0.1 degree tilt.

As observed in Figure 6.1a, a gradient of optical path occurs due to the tilt, as expected. Moreover, even a subtle tilt as low as 0.1 degree can lead to differences in optical path up to twice the wavelength in absolute value. This discrepancy would result in a loss of coherence, underscoring the critical importance of tip/tilt monitoring.

The subsequent phase distribution is presented in Figure 6.1b. The purely longitudinal aspect of the imperfection is evident from the periodic pattern of the phase. As discussed previously, phase changes up to a full period occur at certain bands of the detector, significantly degrading interference quality.

The interference intensity of this signal interfered with a perfect non-perturbed one is displayed in Figure 6.2.

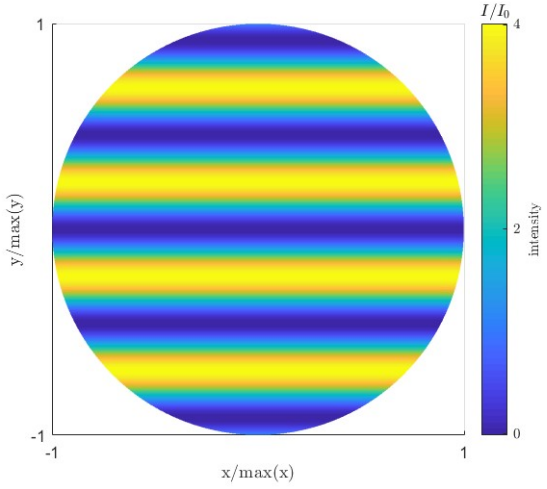

Figure 6.2: Interference intensity of SCoHo configuration with a 0.1 degree tilt.

The longitudinal aspect persists, and constructive interference occurs at locations where the phase change is π in Figure 6.2. The nulling capability of this optical design is disastrous, highlighting

the necessity of tilt corrections to address these types of imperfections. Such tilt errors may arise from instrument tolerances, calibration issues, vibrations, or inadequacies in the Attitude Determination and Control System (ADCS) for tracking the star accurately.

6.1.2 Sensitivity analysis

Interference quality proxies for a single value of tilt do not bring enough information on the behavior of the design due to tipping or tilting. Hence, more simulations are performed for various angles of tilt only. Since only tip would result in similar results by an argument of symmetry, the following discussion is also valid for tip only.

Figure 6.3 illustrates the evolution of the maximum optical path difference when varying the tilt angle of the detector.

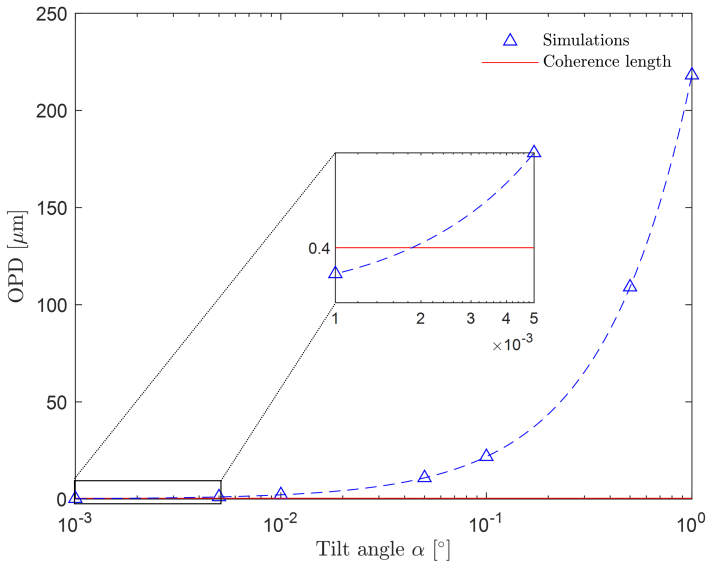

Figure 6.3: Sensitivity analysis of the maximum optical path difference with respect to tilt angles. Discrete data from simulations (blue triangle) and coherence length (red) are represented.

A cubic fit of the data retrieved is also presented as well as the value of the coherence length L_c for further discussion.

From Figure 6.3, it is inferred that the critical angle value for tilt, above which interference quality is jeopardized, is given by $0.002°$. This highlights once again the need for tip/tilt corrections. A tip/tilt mirror appears as mandatory to enforce and ensure coherence maintenance.

Additionally, the sensitivity analysis based on the figure of merit, the response function, is provided in Figure 6.4.

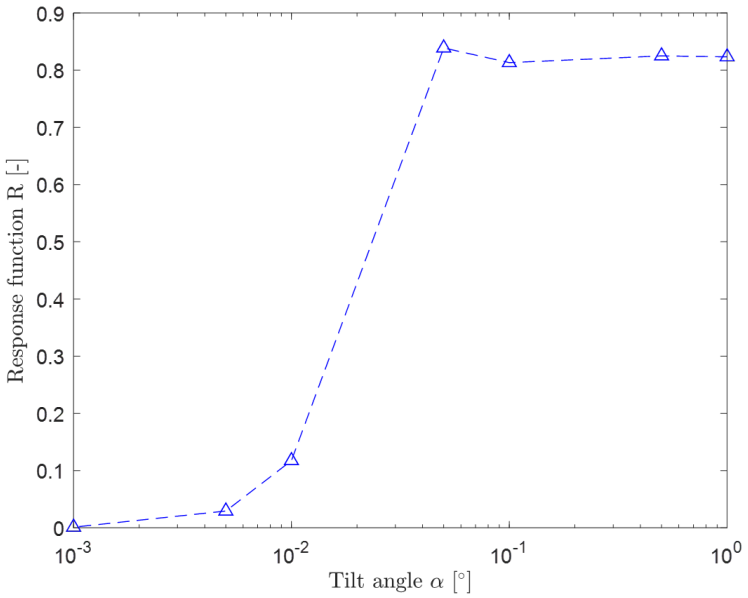

Figure 6.4: Sensitivity analysis of the response function with respect to tilt angles.

The response function quickly rises from its nominal value of 0 when the lightbeam is slightly tilted, underscoring once more the need for correction mechanisms.

6.1.3 Tip/tilt correlation

A particular application of the tool is to investigate the potential correlation between tip and tilt perturbations with the SCoHo design. To this end, all possible combinations of tilt angle α and tip angle β described by the following vectors and expressed in degrees are studied:

$$\alpha = \pm[1 \ ; \ 0.5 \ ; \ 0.1 \ ; \ 0.05 \ ; \ 0.01 \ ; \ 0.005 \ ; \ 0.001 \ ; \ 0] \tag{6.1}$$

and

$$\beta = \pm[1 \ ; \ 0.5 \ ; \ 0.1 \ ; \ 0.05 \ ; \ 0.01 \ ; \ 0.005 \ ; \ 0.001 \ ; \ 0] \ . \tag{6.2}$$

All these different couples of tilt and tip angles are implemented into CodeV and data are retrieved in the sense of optical path difference following the modeling tool developed. Then, those perturbed signals are interfered with a perfect signal and the averaged normalized intensity is computed.

The coupling matrix of said intensities, now denoted $\boldsymbol{I}$ in this development for simplicity sake, is illustrated in Figure 6.5.

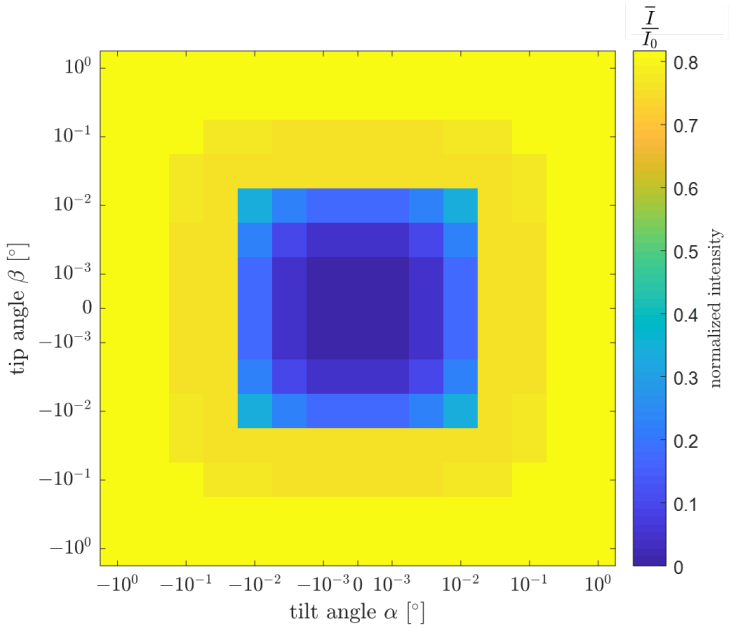

Figure 6.5: Coupling matrix of tip/tilt angles and resulting averaged normalized intensity.

As observed in Figure 6.5, symmetries do exist for tip and tilt perturbations. It can already be inferred that $\mathrm{I}(\boldsymbol{\alpha} = a) = \mathrm{I}(\boldsymbol{\alpha} = -a)$ and equivalently for $\boldsymbol{\beta}$, which was physically expected. Moreover, the relation $\mathrm{I}(\boldsymbol{\alpha} = a) = \mathrm{I}(\boldsymbol{\beta} = a)$ for tip or tilt only is retrieved from the previous section.

By taking advantage of those symmetries, the first quadrant of the matrix can solely be discussed. Results are refined by interpolating the dataset of this first quadrant with a 1000×1000 grid, depicted in Figure 6.6.

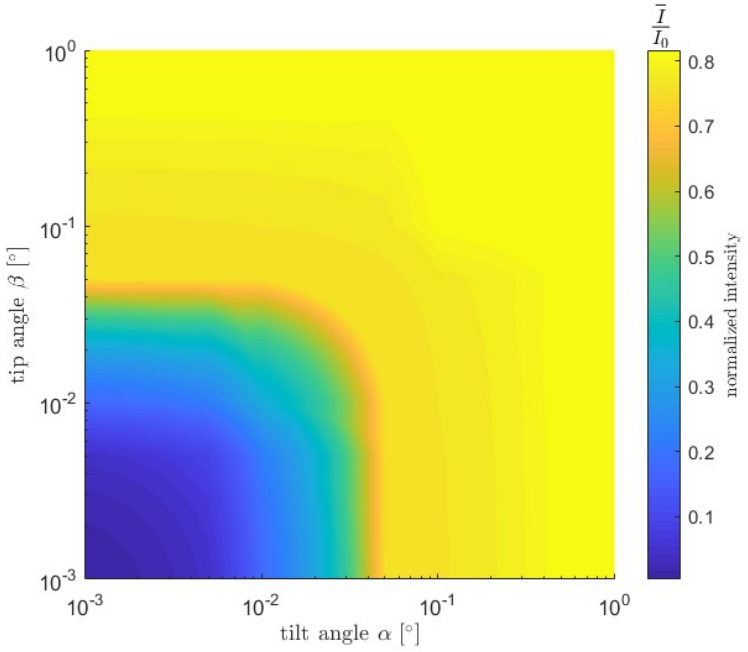

Figure 6.6: Interpolated averaged normalized intensity distribution with respect to tip/tilt angles.

Even though the number of initial discrete data was low, Figure 6.6 exhibits a certain correlation between tip and tilt angles which form quarters of circle.

In all generality, the correlation between the tip β and tilt α angles is illustrated in Figure 6.7.

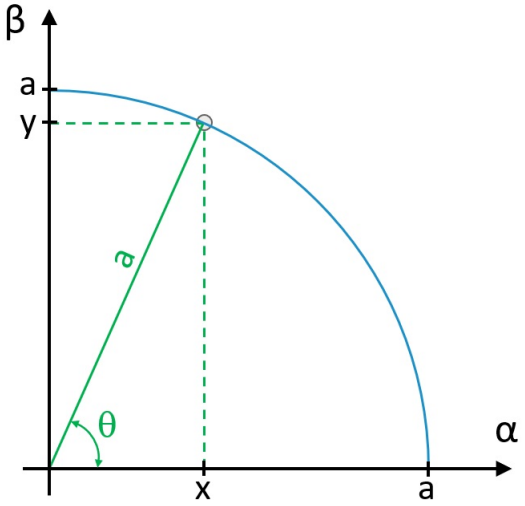

Figure 6.7: Schematic of the tip/tilt angles correlation with respect to the averaged intensity isoline.

Based on this schematic, where the blue line represents the line of equal averaged intensity, it yields that

$$I(\alpha = a, \beta = 0) = I(\alpha = 0, \beta = a) \ , \tag{6.3}$$

where I denotes this averaged intensity for the sake of simplicity as expressed previously.

The previous equation actually proves that tip or tilt only yields the exact same results for a common angle of deviation.

Following the isoline, another relationship is for instance given by

$$I(\alpha = a \cdot \frac{\sqrt{2}}{2}, \beta = 0) = I(\alpha = 0, \beta = a \cdot \frac{\sqrt{2}}{2}) \ , \tag{6.4}$$

by choosing a specific angle $\theta = 45°$.

Generalising this correlation for all angles θ finally gives

$$I(\alpha = x, \beta = y) = \text{constant}, \tag{6.5}$$

if $x = a \cdot \cos(\theta)$ and $y = a \cdot \sin(\theta)$.

Another perspective to this condition writes itself as

$$y = \sqrt{a^2 - x^2} \ . \tag{6.6}$$

Hence, the sine and cosine of θ can be employed as scaling factors to retrieve the expected intensity of tip or tilt only or any given combination since

$$\frac{x}{a} = \cos(\theta) \tag{6.7}$$

and

$$\frac{y}{a} = \sin(\theta) \ . \tag{6.8}$$

However, this relationship has yet to be validated. Figure 6.8 provides the evolution of I with respect to the tilt angle for distinct cases.

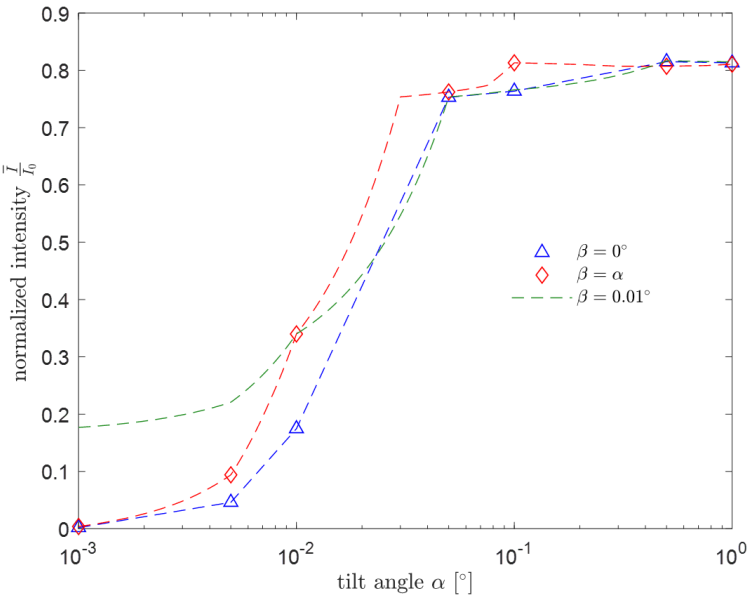

Figure 6.8: Evolution of the averaged normalized intensity with respect to the tilt angle. Three cases are illustrated: tilt only (blue triangle), equal tip/tilt angles (red diamond) and 0.01 degree tip (green dash).

The curve $\beta = 0.01°$ is an example of interpolated data from the matrix, explaining thus the absence of direct simulation points in the graph.

By artificially correcting the different curves using the corresponding scaling factors, the curves align in Figure 6.9, hence demonstrating the validity of the correlation.

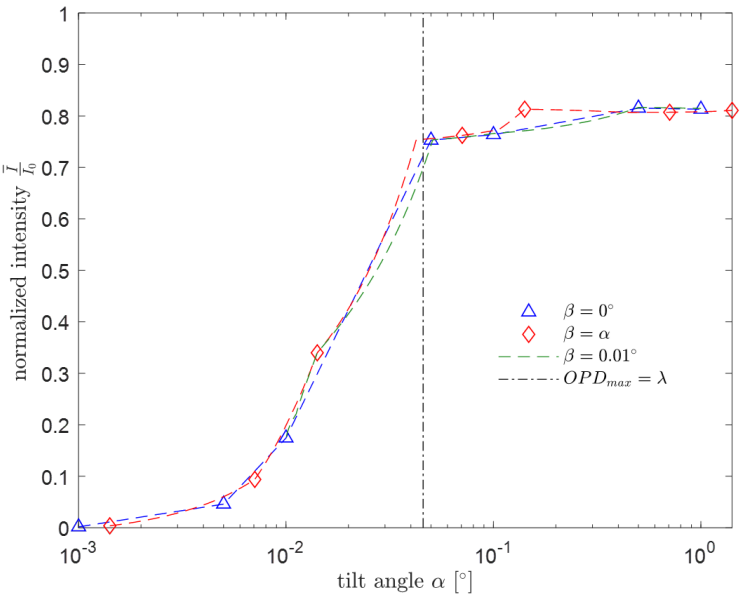

Figure 6.9: Corrected evolution of the averaged normalized intensity with respect to the tilt angle. Three cases are illustrated: tilt only (blue triangle), equal tip/tilt angles (red diamond) and 0.01 degree tip (green dash). The line corresponding to a maximum optical path equal to the working wavelength is also provided.

Furthermore, Figure 6.9 can be divided into two different regimes: a quick rise of I followed by a kind of plateau. This frontier is due to the maximum optical path difference exceeding the working wavelength $\lambda = 10\,\mu m$. This leads to a complete loss of coherence resulting in those two distinct regimes. The associated tilt angle value is $\alpha = 0.0458°$ clearly marks this separation.

This value is easily computed following the geometric relationships of an inclined plane as

$$\alpha = \tan^{-1} \frac{10}{1.25} \cdot \frac{10^{-6}}{10^{-2}} = 0.0458° \ . \tag{6.9}$$

To further demonstrate this correlation, two specific cases are implemented in CodeV, corresponding to angles θ of 45 and 60 degrees and a of 1 and 0.01 degrees. The retrieved intensity from the modeling tool is then compared to the equivalent tilt only perturbation. Table 6.1 summarizes those results.

Table 6.1: Tip/tilt correlation demonstration.

	Tilt only	**Tip/tilt**	**Relative error** [%]
Case 1	0.8131	0.8133	0.025
Case 2	0.1745	0.1803	3.3324

Despite the exact cosine and sine values of the angles can not be implemented in CodeV, the relative errors remains small and the correlation offers good precision.

6.2 Mirror curve imperfections

6.2.1 Applied case

Imperfections may arise from various reasons, one of which being the mirror quality. Typical mirror curvature tolerances from manufacturers vary from ±0.5% to ±0.1% or even ±0.01% for extremely high-quality products [52]. The first mirror curvature is changed by 0.1% in the DiCoS configuration to detail the methodology.

The optical path distribution and corresponding phase distribution are illustrated in Figure 6.10.

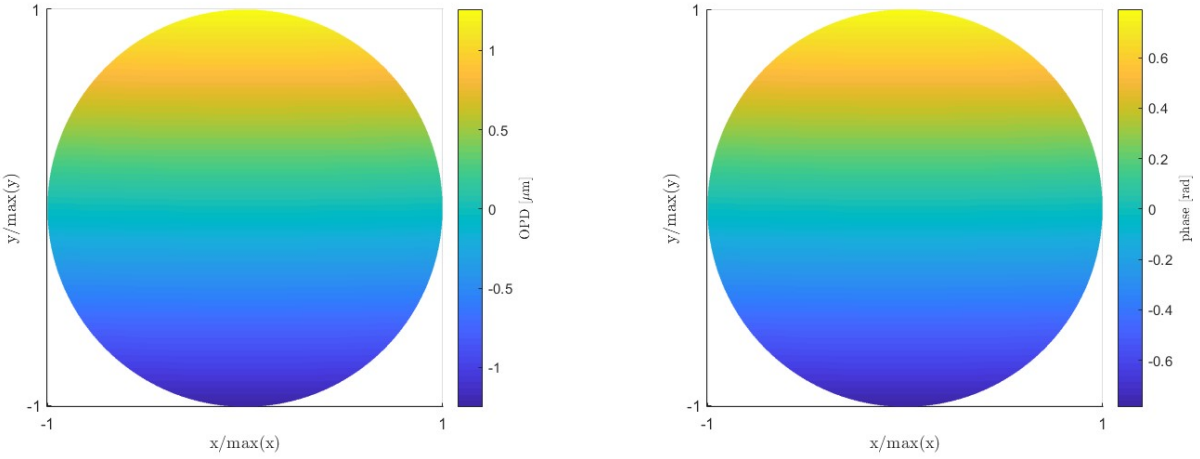

(a) Optical path distribution

(b) Relative phase distribution

Figure 6.10: Optical path and corresponding phase distributions of DiCoS configuration with a 0.01 % curve imperfection.

As observed in Figure 6.10a, the rays suffer from a slight bending. This is poorly visual due to the high initial value of the radius of curvature, *i.e.* the first mirror is quite flat. The phase distribution is also slightly bended, as depicted in Figure 6.10b. The interference intensity of this signal interfered with a perfect non-perturbed one is displayed in Figure 6.11.

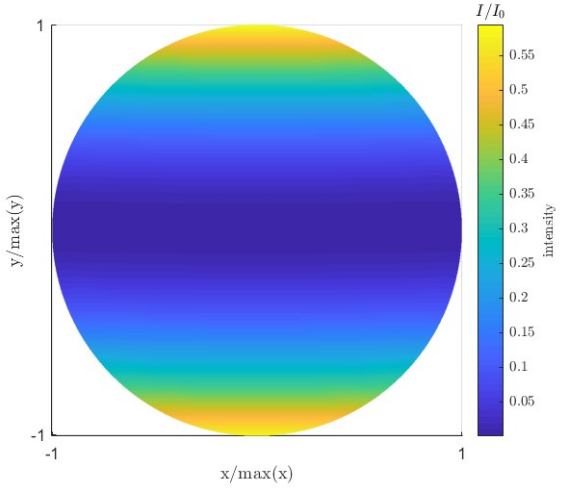

Figure 6.11: Interference intensity of DiCoS configuration with a 0.01 % curve imperfection.

Destructive interference occurs in the whole detector, as illustrated in Figure 6.11, but there are increasing discrepancies towards the extremities. Correction mechanisms such as deformable mirrors, *i.e.* active optics, are essential to monitor and mitigate these kinds of errors.

6.2.2 Sensitivity analysis

The influence of mirror curve imperfections is now generalized by varying the perturbations to investigate the effects on the interference quality of the system. This is represented in Figure 6.12 with the evolution of the maximum optical path difference with respect to several curve imperfections. A cubic fit of the data retrieved is also presented as well as the value of the coherence length L_c for further discussion.

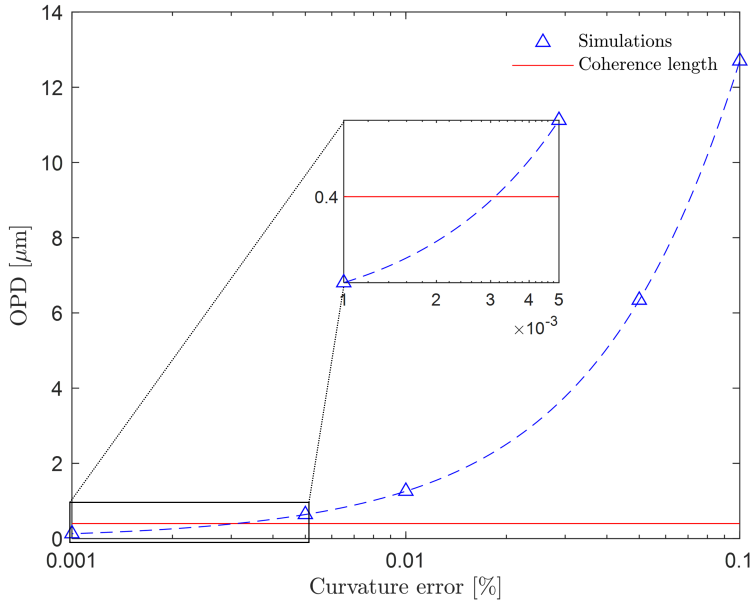

Figure 6.12: Sensitivity analysis of the maximum optical path difference with respect to first mirror curve imperfections of DiCoS. Discrete data from simulations (blue triangle) and coherence length (red) are represented.

From Figure 6.12, it is inferred that the critical curve imperfection value is around 0.003 % for the DiCoS configuration. Since the most precise mirrors have a precision around 0.01 %, as discussed previously, this reinforces the need for active optics to mitigate those perturbations.

The sensitivity analysis is also performed for the response function in Figure 6.13.

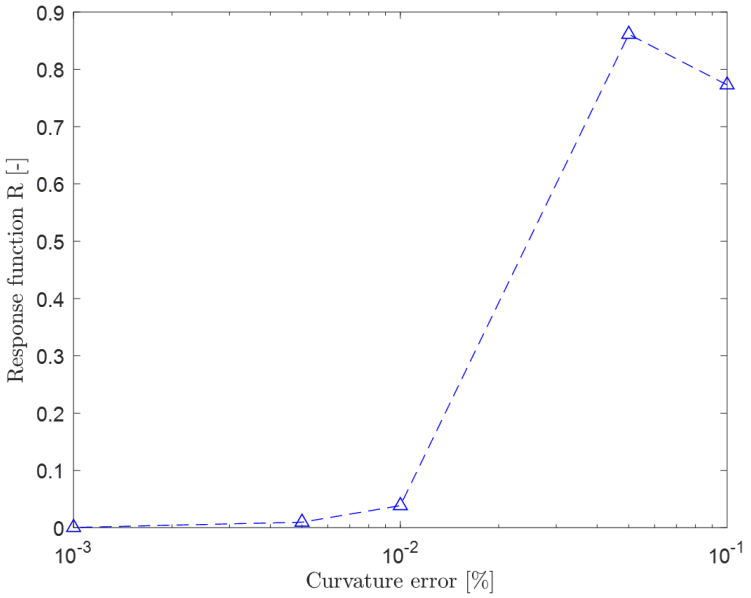

Figure 6.13: Sensitivity analysis of the response function relative to first mirror curve imperfections of DiCoS.

The quick rise of the response function from its 0 nominal value underlines again the need for correction mechanisms.

6.3 Conclusions

In this chapter, a second application of the developed **tool** is proposed to demonstrate its capabilities. **Sensitivity analysis** of fixed parameters for both configurations was conducted, yielding several important observations through numerical simulations and data analysis.

By first artificially introducing **tilt** (and equivalently tip) errors, the significant impact of even minor deviations on interference quality was demonstrated. Tilt corrections were identified as essential for maintaining high-quality interference. Sensitivity analysis revealed a critical angle value of $0.002°$.

Furthermore, the investigation of **mirror curvature imperfections** revealed detrimental effects on interference quality, particularly at the extremities of the detector. Correction mechanisms such as deformable mirrors were identified as crucial for mitigating these errors. Sensitivity analysis found the critical curvature imperfection value to be 0.003

Overall, thorough optical design and calibration were underscored as mandatory for ensuring high-quality interference in nulling interferometry. These findings further confirm the need for and overall utility of the developed tool.

Conclusions and perspectives

The purpose of this master's thesis was to develop and **propose a physically compliant analysing tool to assess the performance and interference quality of a space nulling interferometer**. Conducted with similar objectives than the ESA project, in collaboration with TU Delft, KU Leuven, AMOS, and CSL for the development of a L-space mission, this report aims to contribute to the field of nulling interferometry.

After a brief introduction setting the context of space nulling interferometry in the search for exoplanets, the first chapter laid out the **theoretical background of interferometry**, particularly nulling interferometry. It discussed the wave properties of light, crucial for the cancellation of starlight to observe neighboring exoplanets, and explored initial optical concepts, limitations, and key quantities of this optical application.

The following chapter traced the **evolution of nulling interferometers** over the years, whether currently existing on-ground or conceived as space-based concepts, from Bracewell's first concept in 1972 to contemporary ideas.

In chapter three, two optical configurations were proposed and built upon previous ideas and concepts from the state-of-the-art. The first configuration, **SCoHo**, utilizes a siderostat as the initial optical surface, whereas **DiCoS** employs a confocal system. These configurations were subsequently used as benchmarks for developing the analyzing tool.

The heart of this thesis lies in chapter four introducing the **analyzing modeling tool to assess space nulling interferometer performance**. This tool combines results from the ray-tracing software CodeV with MATLAB's post-processing capabilities to provide a robust method for thoroughly analyzing optical designs. By computing the phase difference distribution for each signal from the optical path length of each light ray, the tool can generate various results, such as intensity distribution, interferograms, and response functions, key metrics in space nulling interferometry. It also enables an alternative approach directly using intensities of the signals. **This thesis brings a rigorous approach, supported by mathematical proofs, compared to the existing limited models.**

Subsequent chapters involved case study for testing the performance modeling tool in **tolerancing**. Chapter five explored **Monte Carlo simulations** for global tolerancing, while chapter six conducted **sensitivity analyses** by fixing specific parameters. Notably, a correlation between tip and tilt angles was identified, and critical values for tip/tilt angles and mirror curvature precision were derived. These precise values underscored the importance of controlling optics, such as tip/tilt mirrors and deformable mirrors, to ensure coherence and high interference precision.

In conclusion, the developed analyzing tool will significantly aid in assessing the quality as well as predicting the performance of space nulling interferometers and in tolerancing optical designs. This master's thesis paves the way for future work to apply this tool to specific optical designs and conduct a precise and thorough analysis, further demonstrating the tool's full potential.

Illuminating the darkness of the far cosmos, nulling interferometry opens a path to a deeper understanding of the universe and brings humanity a little step closer to discovering the hidden mysteries lying in the distant stars. **What will nulling interferometry teach us tomorrow ?**

Appendices

A: Proxima Centauri angular diameter

Considering the mean distance $d = 4.2456$ ly between the Earth and Proxima Centauri described by a radius $R = 107280$ km, the angular diameter of the star θ_* is given by

$$\theta_* = 2 \cdot \tan^{-1}\left(\frac{107280}{4.246 \cdot 9.461 \cdot 10^{12}}\right) \cdot \frac{180}{\pi} \cdot 3600000 \approx 63 \text{ mas}, \tag{6.10}$$

considering the conversion from ly to km and from rad to mas. For the sake of simplicity, a rounded value of 60 mas is used in the work.

B: Numerical convergence

For a rigorous and reliable investigation, it is mandatory to consider the influence of discretization elements, as numerical errors could potentially distort results. There are two levels of discretization in the methodology. The former occurs in CodeV with the number of selected rays investigated in terms of optical path whereas the latter lies in the choice of the interpolated grid.

Figure 6.14 illustrates the different beam discretizations studied in CodeV.

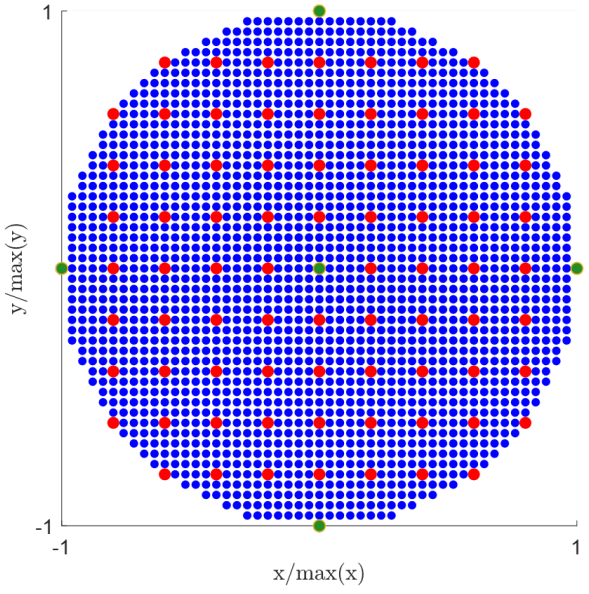

Figure 6.14: Different levels of beam discretization onto the detector.

Each color represents the rays added in the discretization from one level to another. It finally comes down to three cases: 5 (green), 81 (red) and 317 (blue) discrete rays.

Moreover, various squared grid sizes are investigated: 500, 1000, 2000 and 5000. The number of associated interpolated rays is preferred for the figures hereunder.

Figure 6.15 illustrates the influence of both discretizations on the response function value and the CPU time of the algorithm.

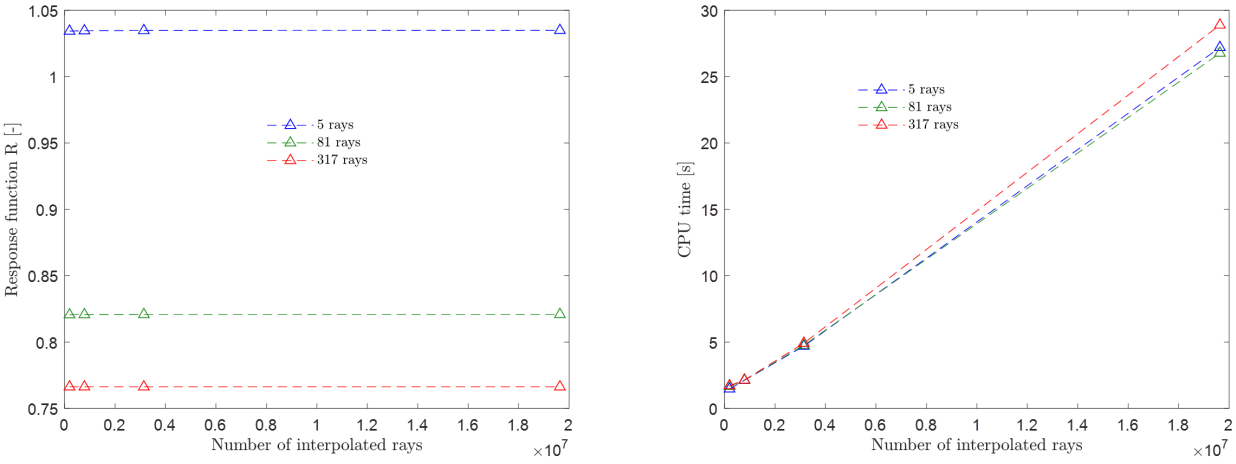

(a) Response function

(b) CPU time

Figure 6.15: Influence of the number of selected rays and interpolated rays on the algorithm.

As observed in Figure 6.15a, the grid size has practically no effect on the convergence of $\boldsymbol{R}$. However, as expected, the higher the grid size, or equivalently the number of interpolated rays, the longer the CPU time, as represented in Figure 6.15b. The grid size is thus set to 1000×1000 to allow for a certain margin without drastically increasing the algorithm duration. This corresponds approximately to 800000 interpolated rays, taking into account the circular aperture.

Figure 6.16 offers a better visualization of the convergence with respect to the discretization of the beam in CodeV.

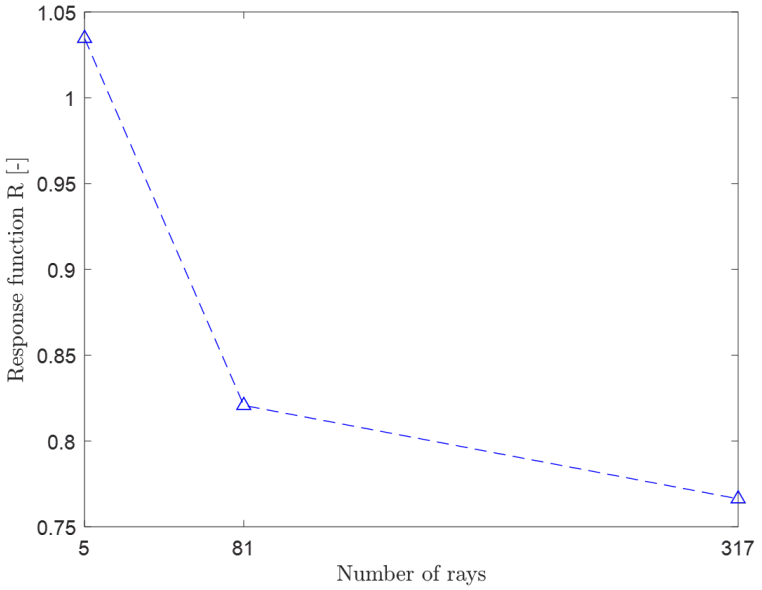

Figure 6.16: Convergence analysis of the response function with respect to the number of selected rays.

As observed in Figure 6.16, the figure of merit is converging and for 317 rays the fit curve slope is approaching a zero value. The number of selected rays is then set to 317. Furthermore, the time required for the extraction of the data in CodeV increases with the number of rays, making it complex to further increase this value. It comforts the final choice 317 rays with an interpolated 1000×1000 grid.

The convergence of the intensity distribution provided in Figure 6.17 is another proof of the final choice of 317 rays.

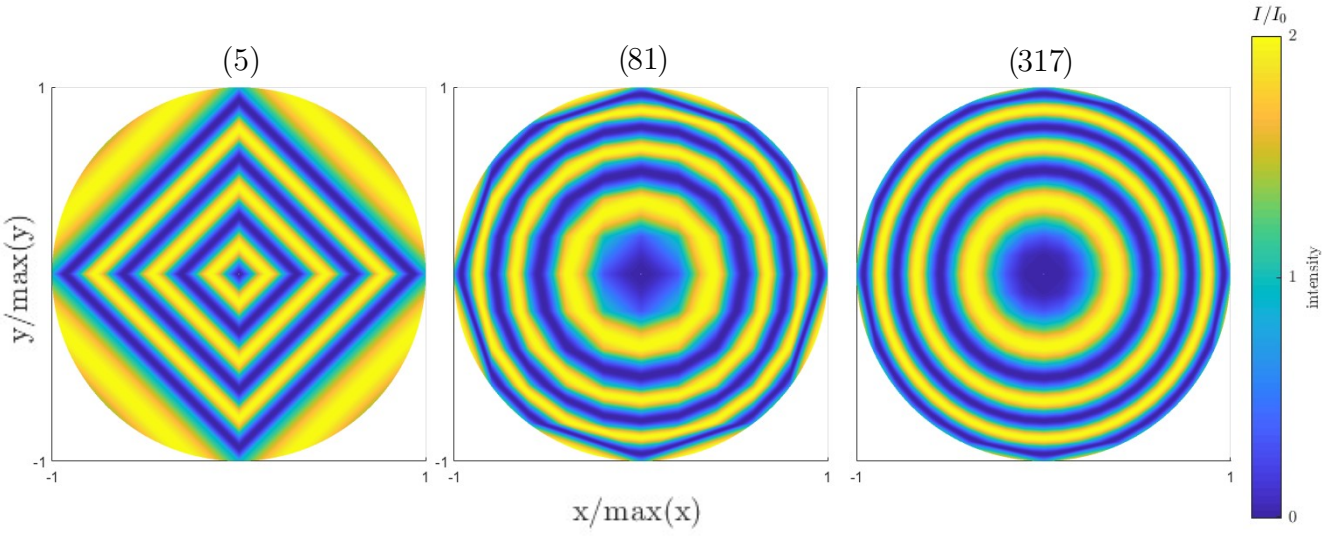

Figure 6.17: Intensity distribution convergence.

C: Unperturbed response function

As demonstrated in [10] starting from S,

$$S = \frac{1}{\sqrt{2}}\left(e^{iC} + e^{-iC} \cdot e^{i\pi}\right) \ , \tag{6.11}$$

the unperturbed response function can be derived.
Euler's formula simply gives

$$e^{i\pi} = \cos(\pi) + i \cdot \sin(\pi) = -1 \ . \tag{6.12}$$

Replacing in S,

$$S = \frac{1}{\sqrt{2}}\left(e^{iC} - e^{-iC}\right) \tag{6.13}$$

subsequently gives

$$S = \frac{2i}{\sqrt{2}}(\sin(C)) \tag{6.14}$$

by taking advantage of the complex definition of the sine.
Taking the modulus square finally yields the wanted unperturbed response function

$$R = \frac{1}{2}\left(4\sin^2(C)\right) = 2\sin^2(C) \ , \tag{6.15}$$

where it is recalled that $C = \dfrac{\pi b \theta}{\lambda}$.

Bibliography

[1] A. Wolszczan and D. A. Frail, "A planetary system around the millisecond pulsar PSR1257 + 12," *Nature*, vol. 355, no. 6356, pp. 145–147, 1992.

[2] M. Mayor and D. Queloz, "A Jupiter-mass companion to a solar-type star," *Nature*, vol. 378, pp. 355–359, Nov. 1995. Number: 6555 Publisher: Nature Publishing Group.

[3] "5 Ways to Find a Planet | Explore." URL: https://exoplanets.nasa.gov/alien-worlds/ways-to-find-a-planet. Last accessed 7 February 2024.

[4] Yaël Nazé, *Les couleurs de l'Univers*. BELIN - Pour la Science.

[5] L. Université, "Trappist." URL: https://www.trappist.uliege.be/cms/c_5006023/fr/trappist?id=c_5006023.

[6] D. A. Fischer, A. W. Howard, G. P. Laughlin, B. Macintosh, S. Mahadevan, J. Sahlmann, and J. C. Yee, "Exoplanet detection techniques," *arXiv preprint arXiv:1505.06869*, 2015.

[7] "Esa | exoplanets detection." URL: https://www.esa.int/Science_Exploration/Space_Science/Exoplanets/How_to_find_an_exoplanet. Last accessed 20 February 2024.

[8] D. Defrère, J. Loicq, *Lecture notes : Space Interferometry Basics, history, configuration, design issues, prospects (SPAT0073-1)*. Université de Liège, 2023.

[9] D. Defrère, J. Loicq, *Lecture notes : Telescopes and Telescope Optics, history, optics, configuration, design issues, future (SPAT0073-1)*. Université de Liège, 2023.

[10] O. Absil, "Astrophysical studies of extrasolar planetary systems using infrared interferometric techniques," Mar. 2006. Publisher: ULiège - Université de Liège.

[11] A. R. Thompson, J. M. Moran, and G. W. Swenson, "Van Cittert–Zernike Theorem, Spatial Coherence, and Scattering," in *Interferometry and Synthesis in Radio Astronomy* (A. R. Thompson, J. M. Moran, and G. W. Swenson Jr., eds.), Astronomy and Astrophysics Library, pp. 767–786, Cham: Springer International Publishing, 2017.

[12] "Atmospheric absorption." URL: https://www.noaa.gov/jetstream/satellites/absorb. Last accessed 8 February 2024.

[13] D. L. Fried, "Statistics of a Geometric Representation of Wavefront Distortion," *JOSA*, vol. 55, pp. 1427–1435, Nov. 1965. Publisher: Optica Publishing Group.

[14] R. J. Noll, "Zernike polynomials and atmospheric turbulence*," *JOSA*, vol. 66, pp. 207–211, Mar. 1976. Publisher: Optica Publishing Group.

[15] W. S. Telescope, "Transmission spectrum of an earth-like atmosphere." URL: https://webbtelescope.org/contents/media/images/01F8GF9XGA29AD3QWNPNKMPD1W.

[16] R. N. Bracewell, "Detecting nonsolar planets by spinning infrared interferometer," *Nature*, vol. 274, pp. 780–781, Aug. 1978. Number: 5673 Publisher: Nature Publishing Group.

[17] C. Dandumont, D. Defrère, J. Kammerer, O. Absil, S. P. Quanz, and J. Loicq, "Exoplanet detection yield of a space-based Bracewell interferometer from small to medium satellites," *Journal of Astronomical Telescopes, Instruments, and Systems*, vol. 6, p. 035004, Sept. 2020. Publisher: SPIE.

[18] R. Laugier, N. Cvetojevic, and F. Martinache, "Kernel nullers for an arbitrary number of apertures," *Astronomy & Astrophysics*, vol. 642, p. A202, Oct. 2020. arXiv:2008.07920 [astro-ph].

[19] F. Martinache and M. Ireland, "Kernel-nulling for a robust direct interferometric detection of extrasolar planets," *Astronomy & Astrophysics*, vol. 619, Feb. 2018.

[20] J. R. P. Angel and N. J. Woolf, "An Imaging Nulling Interferometer to Study Extrasolar Planets," *The Astrophysical Journal*, vol. 475, p. 373, Jan. 1997.

[21] B. Mennesson and J. M. Mariotti, "Array configurations for a space infrared nulling interferometer dedicated to the search for earthlike extrasolar planets," *Icarus*, vol. 128, no. 1, pp. 202–212, 1997.

[22] B. Mennesson, A. Léger, and M. Ollivier, "Direct detection and characterization of extrasolar planets: The mariotti space interferometer," *Icarus*, vol. 178, no. 2, pp. 570–588, 2005.

[23] D. Defrere, "Characterizing extrasolar planetary systems using infrared interferometry," Nov. 2009. Publisher: ULiège - Université de Liège.

[24] "Life space mission." URL: https://life-space-mission.com/. Last accessed 7 February 2024.

[25] F. Roddier, ed., *Adaptive Optics in Astronomy*. Cambridge: Cambridge University Press, 1999.

[26] L. Escarrat, *Contribution au mode coronographique de la mission Darwin*. phdthesis, Université Nice Sophia Antipolis, Nov. 2003.

[27] E. Serabyn, "Nulling interferometry: symmetry requirements and experimental results," in *Interferometry in Optical Astronomy*, vol. 4006, pp. 328–339, SPIE, July 2000.

[28] R. Davies and M. Kasper, "Adaptive Optics for Astronomy," *Annual Review of Astronomy and Astrophysics*, vol. 50, no. 1, pp. 305–351, 2012. _eprint: https://doi.org/10.1146/annurev-astro-081811-125447.

[29] I. Klein, M. Guelman, and S. G. Lipson, "Space-based intensity interferometer," *Applied Optics*, vol. 46, pp. 4237–4247, July 2007. Publisher: Optica Publishing Group.

[30] J. Berger, K. Rousselet-Perraut, P. Kern, F. Malbet, I. Schanen-Duport, F. Reynaud, P. Haguenauer, and P. Benech, "Integrated optics for astronomical interferometry-ii. first laboratory white-light interferograms," *Astronomy and Astrophysics Supplement Series*, vol. 139, no. 1, pp. 173–177, 1999.

[31] M. Schöller, R. Wilhelm, and B. Koehler, "Modeling the imaging process in optical stellar interferometers," *Astronomy and Astrophysics Supplement Series*, vol. 144, no. 3, pp. 541–552, 2000.

[32] B. Mennesson, M. Ollivier, and C. Ruilier, "Use of single-mode waveguides to correct the optical defects of a nulling interferometer," *JOSA A*, vol. 19, pp. 596–602, Mar. 2002. Publisher: Optica Publishing Group.

[33] M. Ollivier, A. Léger, C. A. P. Sekulic, J. Brunaud, G. Artzner, J. M. Mariotti, G. Michel, V. Coudé du Foresto, B. Mennesson, P. Bouchareine, T. Lépine, and F. Malbet, "Nulling Interferometry for the DARWIN Mission - Laboratory Demonstration Experiment," vol. 194, p. 443, Jan. 1999. Conference Name: Working on the Fringe: Optical and IR Interferometry from Ground and Space ADS Bibcode: 1999ASPC..194..443O.

[34] O. P. Lay, "Systematic errors in nulling interferometers," *Applied Optics*, vol. 43, pp. 6100–6123, Nov. 2004. Publisher: Optica Publishing Group.

[35] "Large binocular telescope observatory." URL: https://www.lbto.org/. Last accessed 13 February 2024.

[36] S. Ertel, "The LBT Interferometer Instrument overview, future developments, and synergies with JWST, future space missions and ELTs," in *IR2022: An Infrared Bright Future for Ground-based IR Observatories in the Era of JWST*, p. 22, Mar. 2022.

[37] J. M. Leisenring, P. M. Hinz, M. Skrutskie, A. Skemer, C. E. Woodward, C. Veillet, C. Arcidiacono, V. Bailey, M. Bertero, P. Boccacci, A. Conrad, K. d. Kleer, I. d. Pater, D. Defrère, J. Hill, K.-H. Hofmann, L. Kaltenegger, A. L. Camera, M. J. Nelson, D. Schertl, J. Spencer, G. Weigelt, and J. C. Wilson, "Fizeau interferometric imaging of Io volcanism with LBTI/LMIRcam," in *Optical and Infrared Interferometry IV*, vol. 9146, pp. 846–854, SPIE, July 2014.

[38] D. Defrère, A. Bigioli, C. Dandumont, G. Garreau, R. Laugier, M.-A. Martinod, O. Absil, J.-P. Berger, E. Bouzerand, B. Courtney-Barrer, A. Emsenhuber, S. Ertel, J. Gagne, A. Glauser, S. Gross, M. J. Ireland, H.-D. Kenchington, J. Kluska, S. Kraus, L. Labadie, V. Laborde, A. Léger, J. Leisenring, J. Loicq, G. Martin, J. Morren, A. Matter, A. Mazzoli, K. Missiaen, S. Muhammad, M. Ollivier, G. Raskin, H. Rousseau, A. Sanny, S. Verlinden, B. Vandenbussche, and J. Woillez, "L-band nulling interferometry at the VLTI with Asgard/Hi-5: status and plans," in *Optical and Infrared Interferometry and Imaging VIII*, vol. 12183, pp. 184–199, SPIE, Aug. 2022.

[39] "Nott: The first nulling interferometer for the vlti." URL: http://denis-defrere.com/asgard.php. Last accessed 30 April 2024.

[40] C. A. Beichman, N. J. Woolf, and C. A. Lindensmith, *The Terrestrial Planet Finder (TPF): A NASA Origins Program to Search for Habitable Planets*. National Aeronautics and Space Administration, 1999.

[41] C. Cockell, T. Herbst, A. Leger, O. Absil, C. Beichman, W. Benz, A. Brack, B. Chazelas, A. Chelli, H. Cottin, V. Foresto, W. Danchi, J.-W. Herder, C. Eiroa, M. Fridlund, T. Henning, K. Johnston, L. Kaltenegger, and P. Bordé, "Darwin—an experimental astronomy mission to search for extrasolar planets," *Experimental Astronomy, v.23, 435-461 (2009)*, vol. 23, Mar. 2009.

[42] S. Martin, D. Scharf, R. Wirz, O. Lay, D. McKinstry, B. Mennesson, G. Purcell, J. Rodriguez, L. Scherr, J. Smith, and L. Wayne, "TPF-Emma: concept study of a planet finding space interferometer," *Proc SPIE*, p. 9, Sept. 2007.

[43] P. Lawson, O. Lay, K. Johnston, C. Beichman, S. Unwin, S. Martin, S. Hunyadi, O. Absil, R. Akeson, and J. Bally, "Terrestrial Planet Finder Interferometer (TPF-1) Whitepaper for the AAAC Exoplanet Task Force," p. 9, Apr. 2007.

[44] W. Danchi, R. Allen, D. Benford, D. Deming, D. Gezari, M. Kuchner, D. Leisawitz, R. Linfield, R. Millan-Gabet, J. Monnier, L. Mundy, C. Noecker, J. Rajagopal, L. Richardson, S. Rinehart, S. Seager, W. Traub, and D. Wallace, *The Fourier-Kelvin Stellar Interferometer: a practical interferometer for the detection and characterization of extrasolar giant planets*. Oct. 2004.

[45] M. Ollivier, O. Absil, F. Allard, J.-P. Berger, P. Bordé, F. Cassaing, B. Chazelas, A. Chelli, O. Chesneau, V. Coudé du Foresto, D. Defrère, P. Duchon, P. Gabor, J. Gay, E. Herwats, S. Jacquinod, P. Kern, P. Kervella, J.-M. Le Duigou, A. Léger, B. Lopez, F. Malbet, D. Mourard, D. Pelat, G. Perrin, Y. Rabbia, D. Rouan, J.-M. Reiss, G. Rousset, F. Selsis, P. Stee, and J. Surdej, "PEGASE, an infrared interferometer to study stellar environments and low mass companions around nearby stars," *Experimental Astronomy*, vol. 23, pp. 403–434, Mar. 2009.

[46] M. C. Noecker, R. Linfield, D. Miller, D. Osterman, S. Kilston, M. Lieber, B. Babb, A. Cavender, and J. Jacobs, "Cold interferometric nulling demonstration in space (CINDIS)," in *Techniques and Instrumentation for Detection of Exoplanets*, vol. 5170, pp. 113–128, SPIE, Nov. 2003.

[47] S. P. Quanz, M. Ottiger, E. Fontanet, J. Kammerer, F. Menti, F. Dannert, A. Gheorghe, O. Absil, V. S. Airapetian, E. Alei, R. Allart, D. Angerhausen, S. Blumenthal, L. A. Buchhave, J. Cabrera, Carrión-González, G. Chauvin, W. C. Danchi, C. Dandumont, D. Defrére, C. Dorn, D. Ehrenreich, S. Ertel, M. Fridlund, A. García Muñoz, C. Gascón, J. H. Girard, A. Glauser, J. L. Grenfell, G. Guidi, J. Hagelberg, R. Helled, M. J. Ireland, M. Janson, R. K. Kopparapu, J. Korth, T. Kozakis, S. Kraus, A. Léger, L. Leedjärv, T. Lichtenberg, J. Lillo-Box, H. Linz, R. Liseau, J. Loicq, V. Mahendra, F. Malbet, J. Mathew, B. Mennesson, M. R. Meyer, L. Mishra, K. Molaverdikhani, L. Noack, A. V. Oza, E. Pallé, H. Parviainen, A. Quirrenbach, H. Rauer, I. Ribas, M. Rice, A. Romagnolo, S. Rugheimer, E. W. Schwieterman, E. Serabyn, S. Sharma, K. G. Stassun, J. Szulágyi, H. S. Wang, F. Wunderlich, M. C. Wyatt, and LIFE Collaboration, "Large Interferometer For Exoplanets (LIFE). I. Improved exoplanet detection yield estimates for a large mid-infrared space-interferometer mission," *Astronomy and Astrophysics*, vol. 664, p. A21, Aug. 2022. ADS Bibcode: 2022A&A...664A..21Q.

[48] V. Moreau, C. Flebus, J. Loicq, *Lecture notes : Optics manufacturing (SPAT0073-1)*. Université de Liège, 2023.

[49] James R. Wert, David F. Everett, Jeffery J. Puschell , *Space Mission Engineering: The New SMAD*. Space Technology Library.

[50] R. Williamson, "Field guide to optical fabrication," Spie, 2011.

[51] U. of Arizona, "Tolerancing optical systems." URL: https://wp.optics.arizona.edu.

[52] "Understanding optical specifications." URL: https://www.edmundoptics.com/knowledge-center/application-notes/optics/understanding-optical-specifications/. Last accessed 2 April 2024.